

THESIS

CATIONIC-DOPING OF MAYENITE ELECTRIDE: SYNTHESIS, PROCESSING, AND  
EFFECT ON THERMAL STABILITY

Submitted by

Brodderic DeBoer

School of Advanced Materials Discovery

In partial fulfillment of requirements

For the Degree of Master of Science

Colorado State University

Fort Collins, Colorado

Summer 2021

Master's Committee:

Advisor: Kaka Ma

Chris Weinberger  
Travis Bailey  
Todd Bandhauer

Copyright by Brodderic Alan DeBoer 2021

All Rights Reserved

## ABSTRACT

### CATIONIC-DOPING OF MAYENITE ELECTRIDE: SYNTHESIS, PROCESSING, AND EFFECT ON THERMAL STABILITY

Mayenite electride is an electrically conductive ceramic developed from its parent phase, oxy-mayenite ( $12\text{CaO}\cdot7\text{Al}_2\text{O}_3$ , commonly referred to as C12A7). C12A7 has a unique unit cell that consists of a positively charged  $[\text{Ca}_{24}\text{Al}_{28}\text{O}_{64}]^{4+}$  framework containing twelve cages and two extra-framework  $\text{O}^{2-}$  ions located inside two cages. The extra-framework  $\text{O}^{2-}$  ions can be replaced with electrons when C12A7 is heated in a reducing environment, and those extra-framework electrons act like anions, forming the mayenite electride phase, denoted as C12A7: $e^-$  hereafter. The anionic electrons enable peculiar properties of C12A7: $e^-$  such as high electrical conductivity and low work function, making it a promising material for field emission devices, thermionic-cooling, and as a hallow cathode for electrical propulsion. Compared to other electride materials such as Ca<sub>2</sub>N, which barely sustain their electride properties even at ambient conditions, C12A7: $e^-$  has been reported to be stable up to 400 °C. This temperature is yet not high enough to enable its applications in the technologies mentioned above. Doped derivatives of C12A7: $e^-$  emerged in recent years to improve its electronic properties, mainly electron density and electrical conductivity. However, the effects of doping on the oxidation resistance and thermal stability of C12A7: $e^-$  remained unclear. Experimental effort on cationic doping of C12A7: $e^-$  was particularly lacking in the literature. Therefore, the goal of this study is two-fold: (1) to develop processing routes for successful cationic doping of C12A7: $e^-$ , and (2) to test if cationic doping can improve the thermal stability of C12A7: $e^-$ .

Copper (Cu) and niobium (Nb) were selected as cationic dopants in this study to elucidate how cationic doping affects the thermal stability of the mayenite electride. First, effort was focused on developing synthesis and processing methods to effectively dope Cu and Nb into C12A7:e<sup>-</sup>. Three different methods were investigated, including diffusion doping; in conventional furnace or via spark plasma sintering (SPS), single-step *in-situ* formation via SPS, and a solid-state reaction (SSR) synthesis followed by reduction. The phase constitutions, lattice parameters, and microstructure of the various C12A7:e<sup>-</sup> samples fabricated via the aforementioned methods were characterized to verify if cationic doping was successfully achieved. Electrical conductivity was measured to verify the electride phase is sustained after the doping. Thermal analysis was performed to determine the thermal stability of the cation-doped C12A7:e<sup>-</sup> compared to undoped counterparts, including onset temperature and peak temperature of oxidation, oxidation rate, mass gain percentage resulted from oxidation, and any decomposition reaction.

The key findings of this study include: (1) both Cu-doping and Nb-doping improved the thermal stability of the C12A7:e<sup>-</sup> by increasing the onset temperatures of oxidation; (2) Cu-doping was effectively and efficiently achieved via the novel SPS diffusion doping method. SPS diffusion doping of Cu at 800 °C gave rise to a minimum lattice parameter ( $a = 11.942 \text{ \AA}$ ) of C12A7:e<sup>-</sup>, the lowest oxidation rate, and the smallest mass gain percent at 1050 °C; (3) Using oxy-mayenite and Nb<sub>2</sub>O<sub>5</sub> as precursor for reaction sintering and *in-situ* reduction in SPS led to successful Nb-doping into the C12A7:e<sup>-</sup>. Despite the increased onset oxidation temperature resulted from Nb addition, pest oxidation occurred in Nb-doped C12A7:e<sup>-</sup> samples, leading to high oxidation rate, high total mass gain percentage, and fracture of the solid samples at temperature above 700 °C. In conclusion, Cu-doping was experimentally proved to be an

effective approach to improve the thermal stability of C12A7:e- and meanwhile increase the electrical conductivity.

## ACKNOWLEDGEMENTS

First and foremost, I would like to thank my advisor, Dr Kaka Ma for her guidance and giving me this opportunity. It cannot be easy doing all that she does for her students, the university, and in all her other endeavors. I have not been the easiest student to deal with and she has responded with encouragement and a nudge in the right direction. I am truly thankful for the experience of being her student. I would like to thank Dr Chris Weinberger for taking me through an intense academic journey with many technical discussions in class and at the Factory. Dr Travis Bailey has been involved in my academic career since being an undergraduate. Without him I would not have had this opportunity or even dreamt that it was possible. I would also like to thank Dr Todd Bandhauer for his time and effort serving on my committee, as well as his valuable feedback on my work.

This project would not be possible without the financial support and sponsorship of Lockheed Martin. I sincerely appreciate Dr. Luke Uribarri and Dr. Thomas McGuire at Lockheed Martin for their valuable feedback throughout the course of my research. I am grateful for the staff in the CSU ARC, namely Dr Brian Newell, Dr Pat McCurdy, and Dr Rebecca Miller. The value of training and the assistance provided cannot be overstated.

I would like to thank the students in the School of Advanced Materials Discovery and everyone in the Factory, especially my lab members Alex Preston, Alex Sutherland, Yuchen Lin, and Liam Fisher. Their conversations and ideas that lead to scientific discussions were my favorite part of each workday. Particular thanks go to my predecessor Adam Kuehster for introducing me into the lab and mentoring me in the beginning.

Without the support of my mom and dad I would not be the person I am today. I could never thank them enough for my life up to this point. Finally, I want to thank my late grandfather John Robinette. He took a genuine interest in all my scientific pursuits when he always asked about my research, encouraged me, and believed I could do anything.

## TABLE OF CONTENTS

ABSTRACT .....	ii
ACKNOWLEDGEMENTS.....	v
LIST OF TABLES.....	ix
LIST OF FIGURES .....	x
CHAPTER 1: Introduction.....	1
1.1 Mayenite and Mayenite Electride.....	1
1.2 Doped Derivatives of C <sub>12</sub> A <sub>7</sub> and C <sub>12</sub> A <sub>7</sub> :e <sup>-</sup> .....	5
1.3 Solid State Diffusion.....	8
1.4 Spark Plasma Sintering .....	10
1.5 Motivation and Objectives .....	15
CHAPTER 2: Material Synthesis and Doping Process.....	18
2.1 Synthesis of Materials.....	19
2.1.1 Mayenite .....	19
2.1.2 Mayenite Electride .....	20
2.2 Dopant Selection.....	20
2.2.1 Copper .....	20
2.2.2 Niobium .....	21
2.3 Cationic Doping Methods .....	22
2.3.1 Diffusion Doping in an Argon Furnace .....	22
2.3.2 Diffusion Doping in Spark Plasma Sintering .....	23
2.3.3 Cationic Doping in Preformed Mayenite and Mayenite Electride Powder .....	25
2.3.4 Synthesis of Cationic Doped Mayenite Electride from Precursors.....	25
CHAPTER 3: CHARACTERIZATION AND TESTING .....	28
3.1 Phase identification and Crystal Lattice Characterization .....	28
3.1.1 Powder X-ray Diffraction .....	28
3.1.2 Scanning Electron Microscopy .....	29
3.1.3 Electron Dispersive Spectroscopy.....	30
3.1.4 X-ray Photoelectron Spectroscopy .....	31
3.2 Electrical Conductivity Testing .....	32
3.2.1 Two-probe Resistance Measurement .....	32
3.3 Thermal Stability Characterization.....	33

3.3.1 Thermal Gravimetric Analysis .....	33
3.3.2 Differential Thermal Analysis .....	34
CHAPTER 4: EFFECT OF COPPER DOPING ON MAYENITE ELECTRIDE .....	35
4.1 Phase Constitution and Microstructure .....	35
4.2 Structural Analysis.....	41
4.3 Electrical Conductivity .....	43
4.4 Thermal Stability .....	45
4.5 Efficiency of doping by SPS Diffusion .....	55
4.6 Cu Doping Summary .....	57
CHAPTER 5: NIOBIUM DOPING OF MAYENITE ELECTRIDE .....	58
5.1 Nb-C <sub>12</sub> A <sub>7</sub> :e <sup>-</sup> Phase and Microstructural Analysis.....	58
5.1.1 <i>Analysis of Plan A samples</i> .....	58
5.1.2 <i>Analysis of Plan B samples</i> .....	60
5.1.3 <i>Analysis of Plan C samples</i> .....	61
5.1.4 <i>Analysis of Plan D samples</i> .....	65
5.1.5 <i>Analysis of Plan E samples</i> .....	68
5.1.6 Niobium-doping Process Summary .....	69
5.2 Niobium Speciation in Nb-C <sub>12</sub> A <sub>7</sub> :e <sup>-</sup> .....	70
5.3 Electrical Conductivity .....	72
5.4 Thermal Stability .....	73
5.5 Nb Doping Summary .....	81
CHAPTER 6: CONCLUSION .....	83
6.1 Thermal stability of mayenite electride .....	83
6.2 Copper Doping Experiments .....	84
6.3 Niobium Doping Experiments.....	84
6.4 Future Research Directions .....	86
References: .....	89

## LIST OF TABLES

Table 1.1: Maximum electrical conductivities of C<sub>12</sub>A<sub>7</sub>:e<sup>-</sup> reported in literature

Table 1.2: Electrical conductivities of cation-doped C<sub>12</sub>A<sub>7</sub>:e<sup>-</sup> at room temperature

Table 2.1: Characteristics of Ca, Al, Cu and Nb elements

Table 2.2: Summary of the processing parameters for various Cu-C<sub>12</sub>A<sub>7</sub>:e<sup>-</sup> samples and the corresponding IDs

Table 2.3: Summary of the processing routes for various Nb-C<sub>12</sub>A<sub>7</sub>:e<sup>-</sup> samples and the corresponding IDs

Table 4.1: Electrical conductivities of C<sub>12</sub>A<sub>7</sub>:e<sup>-</sup> and Cu-C<sub>12</sub>A<sub>7</sub>:e<sup>-</sup> at room-temperature

Table 5.1: Standard Ca/Al and Ca/Nb ratios for undoped and doped C<sub>12</sub>A<sub>7</sub>:e<sup>-</sup>

Table 5.2: Ca/Al and Ca/Nb atomic ratios of points in Fig 5.14

Table 5.3: Electrical conductivities of C<sub>12</sub>A<sub>7</sub>:e<sup>-</sup> and Nb-C<sub>12</sub>A<sub>7</sub>:e<sup>-</sup> at room-temperature

Table 6.1: Element properties of possible dopants

## LIST OF FIGURES

Figure 1.1: CaO-Al<sub>2</sub>O<sub>3</sub> phase diagram

Figure 1.2: C12A7 (a) cage structure and (b) unit cell

Figure 1.3: Model of Al site occupied by Nb in C12A7 framework

Figure 1.4: Three stages of solid-state sintering

Figure 1.5: Schematic of SPS apparatus

Figure 1.6: Schematic of the one-step synthesis process for C12A7:e-

Figure 2.1: Processing flow chart of material synthesis methods used in this study

Figure 2.2: Diagram of the set-up of samples in (a) conventional furnace and (b) SPS

Figure 4.1: X-ray diffraction (XRD) patterns of C12A7:e<sup>-</sup>, F3, F4, and S2

Figure 4.2: Optical images of the (a) F3 surface and (b) F4 surfaces, and SEM images showing (c) the Cu-C12A7:e<sup>-</sup> boundary on F3 and (d) the copper surface layer on F4

Figure 4.3: SEM images and EDS maps of the cross-section of F4

Figure 4.4: EDS line scans of Cu regions at the diffusion front

Figure 4.5: Post processing (a) SEM image and (b) EDS maps of copper foil surface

Figure 4.6: SEM image and EDS maps of S2 surface

Figure 4.7: (a) XRD pattern of C12A7:e<sup>-</sup> peaks for undoped C12A7:e<sup>-</sup>, F3, and S2 and (b) lattice parameters of the C12A7:e<sup>-</sup> in undoped and Cu-C12A7:e<sup>-</sup> samples

Figure 4.8: Electronic conductivity measurement diagram for the (a) two-probe and (b) four-probe testing

Figure 4.9: (a) Thermalgravimetric mass gain and (b) differential thermal peaks of S-type samples in comparison to an undoped counterpart

Figure 4.10: C12A7:e<sup>-</sup> specimens thermally analyzed to (a) 550°C, (b) 600°C, and (c) 650°C

Figure 4.11: Photos of the two surfaces of C12A7:e<sup>-</sup> at different temperatures showing the color evolution during heating in air in a furnace

Figure 4.12: XRD pattern of the (a) white and (b) tan surfaces of C12A7

Figure 4.13: Optical images of the specimen bottom surface after being held at (a) 1000°C and (b) 1350°C

Figure 4.14: Pictures of specimens cut from S3 after TG test in air (a) a representative specimen without evident Cu-region on surface; and (b) a representative specimen with evident Cu-region on surface

Figure 4.15: XRD pattern for S3 specimen post thermal analysis

Figure 4.16: Optical images of thermally analyzed S2 specimen via furnace heating

Figure 4.17: SPS measurement set-up and thermal gradient model

Figure 5.1: SEM and EDS images of the mixed C12A7:e<sup>-</sup> + Nb powder for Plan A

Figure 5.2: (a) SEM image of A1 surface, (b) XRD pattern of A1 surface, and (c) SEM image and EDS maps of Nb rich particle on the surface of Al

Figure 5.3: Powders of (a) precursor C12A7, (b) crystalline Nb-C12A7, (c) precursor C-type mixture, and (d) C12A7:e<sup>-</sup>

Figure 5.4: Sample B1 (a) optical image and (b) XRD pattern

Figure 5.5: Sample C1 (a) optical image and (b) XRD pattern

Figure 5.6: Microstructure of Sample C2. (a) SEM images of the sample surface and (b) SEM image showing a clear boundary between Nb-rich and Nb-deficient regions with (c) EDS maps

Figure 5.7: Sample C4 (a) optical image and (b) XRD pattern

Figure 5.8: Sample C5 (a) optical image, (b) XRD pattern, and (c) SEM image with EDS maps of a dark particle on the surface

Figure 5.9: XRD patterns of Nb-C12A7 powders produced by SSR at (a) 1300 °C, 10 h and (b) 1350 °C, 12 h

Figure 5.10: Sample D1 (a) optical image of the surface, (b) XRD pattern, and (c) SEM image with EDS maps of the surface

Figure 5.11: Sample D4 (a) optical image and (b) XRD scan

Figure 5.12: Resolidified C12A7:e<sup>-</sup> on Nb metal cap

Figure 5.13: XPS spectrum of (a) C, (b) O, (c) Ca, (d) Al, and (e) Nb in sample C2 including (f) standard BE for Nb 3d5/2 electrons. Note that the black dotted lines in (e) and (f) correspond to Nb 3d5/2 peak BE

Figure 5.14: SEM image of Nb-rich particle on the C5 surface with yellow dots representing EDS scan points

Figure 5.15: TG and DT curves of (a) A1 and (b) B2

Figure 5.16: TG and DT curves of (a) C2, (b) D1, (c) C5, and (d) D4

Figure 5.17: Thermogravimetric curves for Nb-C12A7: $e^-$  specimens and undoped C12A7: $e^-$  from 400°C to 650°C

Figure 5.18: Microscope images of (a) A-type specimens, (b) B-type specimens, and (c) D-type specimens before thermal analysis and when held at 600°C or 650°C

Figure 5.19: C5 specimen after being held at 700°C, 750°C, and 800°C in a furnace with an air atmosphere

Figure 5.20: D4 specimen after being held at 700°C, 750°C, and 850°C in a furnace with an air atmosphere

Figure 5.21: XRD patterns of C5 and D4 powders after TG/DTA

Figure 5.22: Phase evolution during the process flow for the C5 and D4

## CHAPTER 1: Introduction

This chapter provides a literature review regarding material structure, electrical conductivity, stability and oxidation behavior, and processing methods of mayenite ( $\text{C}12\text{A}7$ ), mayenite electride ( $\text{C}12\text{A}7:\text{e}^-$ ), and doped variants of both. It is important to note that doping of mayenite is commonly denoted as  $\text{Ca}_{12}\text{Al}_{14-x}\text{M}_x\text{O}_{33}$  or  $\text{Ca}_{12-x}\text{M}_x\text{Al}_{14}\text{O}_{33}$  in the literature, where M represents a cationic dopant and x represents the dopant concentration. However, in this thesis, it was intentional to use Cu-C<sub>12</sub>A<sub>7</sub>:e<sup>-</sup> and Nb-C<sub>12</sub>A<sub>7</sub>:e<sup>-</sup> to denote the attempts of Cu-doped C<sub>12</sub>A<sub>7</sub>:e<sup>-</sup> and Nb-doped C<sub>12</sub>A<sub>7</sub>:e<sup>-</sup>, respectively, due to that (1) it was not clear whether doping was successfully achieved until the samples were made and characterized; (2) addition of M (Cu or Nb in this study) may lead to compositing, i.e., M may be present as a second phase, rather than solely doping (i.e., M atoms go into the mayenite lattice substituting Ca or Al cations). Then, relevant fundamental principles will be introduced. Finally, the motivation and the aims of this study will be outlined.

### 1.1 Mayenite and Mayenite Electride

Mayenite is a calcium aluminate stoichiometric compound that occurs at the specific calcium oxide ( $\text{CaO}$ ) to alumina ( $\text{Al}_2\text{O}_3$ ) atomic ratio of 12:7 ( $12\text{CaO} \bullet 7\text{Al}_2\text{O}_3$ ). This is also defined as a cationic ratio of  $\text{Ca}/\text{Al} = 0.857$ . Additional calcium increases the  $\text{Ca}/\text{Al}$  ratio causing formation of the Ca-rich  $\text{Ca}_3\text{Al}_2\text{O}_6$  (C<sub>3</sub>A) phase. Conversely, additional aluminum decreases the  $\text{Ca}/\text{Al}$  ratio causing formation of the Al-rich  $\text{CaAl}_2\text{O}_3$  (CA) phase, as shown in the  $\text{CaO}-\text{Al}_2\text{O}_3$  phase diagram (Fig. 1.1).

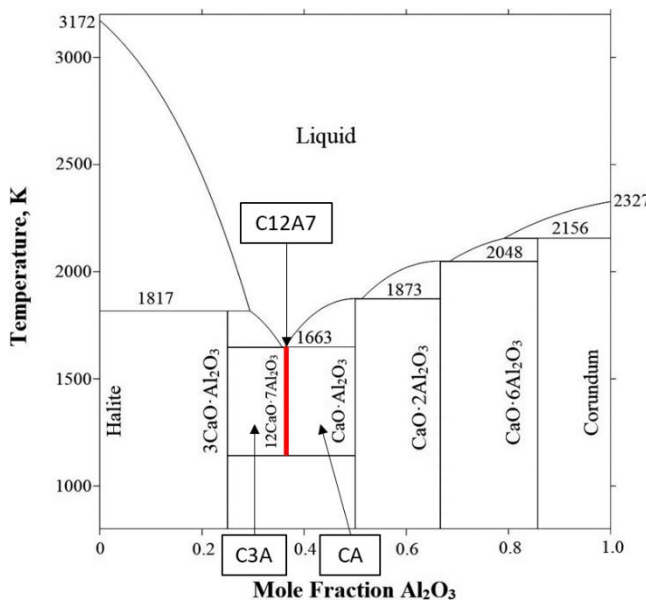


Figure 1.1: CaO-Al<sub>2</sub>O<sub>3</sub> phase diagram<sup>1</sup>

In 1962, C12A7 was discovered as a secondary phase in Portland cements. The C12A7 structure is nano-porous and cubic with space group *I*43d. Each unit cell consists of [Ca<sub>24</sub>Al<sub>28</sub>O<sub>64</sub>]<sup>4+</sup> fixed in a Ca-Al-O framework that arrange into 12 cage structures. Fig 1.2 displays a diagram of individual cage structure and a unit cell. Each cage contains two Ca centered poles that bond to extra-framework anions, have a 5-6 Å diameter, and is connected to adjacent cages by large ‘windows’ approximately 3.7 Å in diameter identified to allow high anion mobility<sup>2</sup>. When cages are occupied by oxide anions (O<sup>2-</sup>), the lattice parameter of a unit cell is C12A7  $a \cong 11.98 \text{ \AA}$ .

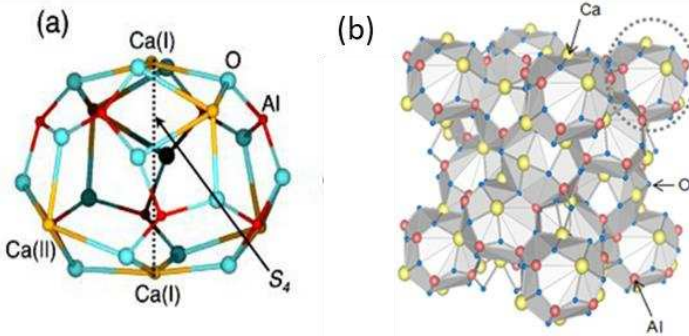
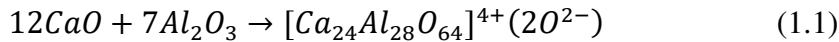


Figure 1.2: C12A7 (a) cage structure<sup>3</sup> and (b) unit cell<sup>4</sup>

The framework exhibits a  $4^+$  charge per unit cell evenly distributed throughout the structure. Extra-framework anions ( $O^{2-}$ ,  $OH^-$ ,  $Cl^-$ ,  $F^-$ , etc.) statistically occupy cages to maintain charge neutrality. When synthesized from precursor material, two oxygen atoms naturally become oxide anions ( $O^{2-}$ ) forming oxy-C12A7 given by Reaction 1.1.



The initially suggested mechanism of oxygen movement within oxy-C12A7 was brought into question by molecular dynamics and *ab initio* calculations<sup>3</sup>. It was later supported that oxygen diffusion in C12A7 proceeds via site-exchange between framework and extra-framework oxygen<sup>5</sup>. Oxy-C12A7 can be utilized as an oxide ion conductor with potential applications in sensors, fuel cells, oxygen pumps, and gauges<sup>6-8</sup>.

In 2003 Matsuishi et al. used Ca vapor treatment to remove extra framework oxygen, replacing oxide anions with an equivalent charge of electrons<sup>9</sup>. C12A7 with electron anions became a new class of material, mayenite electride (C12A7:e-), the first room-temperature stable electride chemically inert in ambient atmosphere. An electride is defined as a material that has some electrons not localized to one atom and act as anions. Discovery of C12A7:e- overcame the largest hurdle in electride research from the 20<sup>th</sup> century. The reduction of oxy-C12A7 into

C<sub>12</sub>A<sub>7</sub>:e<sup>-</sup> results in significant physical property changes. Optically the color of the material changes from white to black after being fully reduced, which is attributed to the formation of a cage conduction band (CCB) allowing for the absorption of visible light<sup>10</sup>. Formation of a CCB is unique to C<sub>12</sub>A<sub>7</sub>:e<sup>-</sup> giving rise to desirable electronic properties including anion mobility (0.1 cm<sup>2</sup> V<sup>-1</sup> s<sup>-1</sup>)<sup>9, 11</sup>, electron density ( $2.3 \times 10^{21}$  cm<sup>-3</sup>), electrical conductivity given in Table 1.1, and low work function (2.4 eV)<sup>10, 12</sup>.

**Table 1.1: Maximum electrical conductivities of C<sub>12</sub>A<sub>7</sub>:e<sup>-</sup> reported in literature**

<b>Material</b>	<b>Structure</b>	<b>Fabrication</b>	<b>Maximum Conductivity [S/cm]</b>
C <sub>12</sub> A <sub>7</sub> :e <sup>-</sup> <sup>13</sup>	Single crystal	Metal Vapor Reduction	1500
C <sub>12</sub> A <sub>7</sub> :e <sup>-</sup> <sup>14</sup>	Thin film	Sputtering	28
C <sub>12</sub> A <sub>7</sub> :e <sup>-</sup> <sup>11</sup>	Polycrystalline	Melt Solidification	5
C <sub>12</sub> A <sub>7</sub> :e <sup>-</sup> <sup>15</sup>	Polycrystalline	Mg Heat Treatment	0.48
C <sub>12</sub> A <sub>7</sub> :e <sup>-</sup> <sup>16</sup>	Polycrystalline	SPS Ti Reduction	138

The unique electronic properties and catalytic activity of C<sub>12</sub>A<sub>7</sub>:e<sup>-</sup> make it a promising material for electron emitters, cathode in cold cathode fluorescent lights (CCFLs), short channel nanowire transistor, ammonia synthesis/decomposition, activation and splitting of carbon dioxide, catalyst for reforming of bio oil, and a chemical reductant<sup>17-25</sup>.

While it is possible to synthesize C<sub>12</sub>A<sub>7</sub>:e<sup>-</sup> samples with high conductivity and near theoretical maximum electron density, there are surface effects that inhibit the conductive and emissive properties. The electro, chemical, or mechanical polishing of C<sub>12</sub>A<sub>7</sub>:e<sup>-</sup> can cause damaged cage structures on environment contacting surfaces. Damaged surface cages lack a cage conduction band (CCB) at the fermi-level resulting in a large band gap. Oxygen or other atmospheric molecules can adhere to C<sub>12</sub>A<sub>7</sub>:e<sup>-</sup> surface forming a boundary. Adsorbed molecule layers and damaged cage structures result in loss of ohmic contact and make C<sub>12</sub>A<sub>7</sub>:e<sup>-</sup> act as an

insulator. It has been shown that argon sputtering and subsequent annealing under particular parameters can create a clean, relatively flat, and conductive surface<sup>25</sup>.

The low work function of C12A7: $e^-$  enables high electron emission current upon an external applied field or thermal stimulus, which makes C12A7: $e^-$  attractive for applications in thermionic cathodes, hallow cathodes for electronic propulsion<sup>26</sup>, and novel hypersonic vehicle cooling technology<sup>27, 28</sup>. The thermionic-emission cooling power ( $P_{emit}$ ) is not significant compared with thermal radiation of the sample ( $P_{rad}$ ) in the temperature range of 600 – 1000 °C. The  $P_{emit}/P_{rad}$  ratio increases with increasing temperature<sup>29</sup>. However, the stability of C12A7: $e^-$  up to 400 °C is not high enough to enable its application in thermionic-emission cooling. Above 400 °C, oxidation occurs to C12A7: $e^-$  in an oxygen-containing environment and C12A7: $e^-$  transits to oxy-C12A7, losing all its unique electronic properties. If C12A7: $e^-$  can be stabilized to higher temperatures, its application in thermionic-emission cooling and/or thermionic energy conversion can be realized. Therefore, it is imperative to improve the thermal stability of C12A7: $e^-$ , which is the primary goal of this study. It is hypothesized that cationic doping can change the lattice parameter of C12A7: $e^-$  and alter its cage opening, and as a result, the adsorption of oxygen on the surface and the subsequent diffusion of oxygen into the bulk would be retarded, leading to improved oxidation resistance.

## 1.2 Doped Derivatives of C12A7 and C12A7: $e^-$

Significant research efforts have been put into the doping of C12A7 in the literature. Cationic dopants can occupy Ca sites or Al sites in the C12A7 framework. The doped derivatives are commonly presented as  $[Ca_{24-x}M_xAl_{28}O_{64}]$  or  $[Ca_{24}Al_{28-x}M_xO_{64}]$  depending on which cationic site is occupied by the dopants. C12A7 has been doped with various cations like rare earth (RE) metals ( $Gd^{3+}$ ,  $Er^{3+}$ ,  $Ce^{3+}$ ,  $Tb^{3+}$ ,  $Eu^{3+}$ ,  $Eu^{2+}$ ) to form RE-C12A7 phosphors<sup>30</sup>.  $Cu^{31, 32}$ ,  $Ni^{33, 34}$ ,  $V^{35}$ ,

Zn, P<sup>36</sup>, Fe, Ir<sup>37</sup>, and Ga<sup>38, 39</sup> were also investigated in previous studies to form cationic doped C12A7 variants. Here the cationic doped mayenite is denoted as M-C12A7 (where M represents any cationic atom). Some RE-C12A7 phosphors had intense field emissions so they can be used for field emission displays with dual functionality. Cu and P doping caused structural changes resulting in a decrease in lattice parameter while Zn doping caused an increase in lattice parameter. Cu doping also resulted in an increased specific surface area of mayenite powders, which was attributed to a contraction of the lattice structure. Cu-C12A7 and Ni-C12A7 showed an increased catalytic activity in chemical conversion processes compared to undoped C12A7. Some studies also reported that the electrical conductivities of C12A7 were slightly decreased for Ni doping and Fe doping<sup>34</sup>, while the oxygen anion mobility was not affected. Ga-C12A7 samples were identified as a single phase for dopant concentrations of  $x = 1$ . Attempts to synthesize material with higher dopant concentration resulted in formation of secondary phases.

Huang et al predicted the effects of cationic dopants ( $Mg^{2+}$ ,  $Cu^{2+}$ ,  $Sr^{2+}$ ,  $Fe^{3+}$ ,  $Ir^{4+}$ ,  $P^{5+}$ , and  $V^{5+}$ ) on the structural and electronic properties of the doped C12A7: $e^-$  materials via density functional theory (DFT) calculations<sup>40</sup>. Limited experimental work has been done on the synthesis and analysis of cation-doped C12A7: $e^-$ . To my knowledge, only four types of cation (V, Sn, Si, and Ga) doped C12A7: $e^-$  derivatives have been successfully synthesized<sup>15, 41-43</sup>. Palacios et al attempted to synthesize Ga-doped C12A7: $e^-$  by reduction of Ga-doped C12A7, which resulted in separation of Ga atoms from C12A7 framework and formation of Ga metal phase and C3A after processing<sup>38</sup>. A modified sol-gel synthesis method developed by Khan<sup>41-43</sup> emerged as an effective process to produce cation doped C12A7: $e^-$ . Solid-state reaction (SSR) of precursor material and subsequent Mg vapor reduction was used to produce Sn-doped C12A7: $e^-$ <sup>15</sup>. Nominal concentrations were tested in the range of  $x = 0.2 \sim 1$ . It is widely accepted

that  $x = 1$  is the highest dopant concentration due to secondary phase formation being detected at  $x \geq 1.5$  for Co and Ga doped C12A7 resulted from low solubility limits<sup>34, 38, 44</sup>. In addition, the electrical conductivity at room temperature (RT) was increased as dopant concentration increased with maximum values reached at  $x = 1$ , as shown in Table 1.2.

Table 1.2: Electrical conductivities of cation-doped C12A7: $e^-$  at room temperature.

<b>Material</b>	<b>Method</b>	<b>Maximum RT Electrical Conductivity [S/cm]</b>
Ga-C12A7: $e^-$ <sup>42</sup>	Modified sol-gel	270
Si-C12A7: $e^-$ <sup>43</sup>	Modified sol-gel	222
Sn-C12A7: $e^-$ <sup>43</sup>	Modified sol-gel	290
Sn-C12A7: $e^-$ <sup>15</sup>	SSR + Mg reduction	1.42
V-C12A7: $e^-$ <sup>41</sup>	Modified sol-gel	40

The electrical conductivity of both the undoped C12A7: $e^-$  and the Sn-doped C12A7: $e^-$  increased with increasing temperature, in accordance with the semiconductor behavior, i.e., thermal energy overcomes the activation energy for electron transport<sup>15</sup>. This can be estimated by the Arrhenius relationship, written as:

$$\sigma = \sigma_0 \exp\left(\frac{-E_a}{k_B T}\right) \quad (1.2)$$

$\sigma_0$  being the constant of conductivity,  $E_a$  being the activation energy,  $k_B$  being the Boltzmann constant, and  $T$  being the temperature in K. The cationic doping of C12A7: $e^-$  resulted in increased electrical conductivity compared to undoped C12A7: $e^-$  synthesized by similar methods in each study in Table 1.2.

### 1.3 Solid State Diffusion

The movement of atoms in space is called diffusion. This process occurs between any two-phase combination (solid, liquid, or gas), specifically solid-solid interactions in this study. Diffusion occurs via Fick's law given by Eq (1.3) and (1.4):

$$\frac{\partial c_i}{\partial t} = D_i \nabla c_i \quad (1.3)$$

$$D_i = D_{i0} \exp\left(\frac{-E_{diff}}{k_B T}\right) \quad (1.4)$$

where  $c_i$  is the concentration of species  $i$ ,  $D_i$  is the diffusion coefficient,  $t$  is time,  $D_{i0}$  is the diffusion coefficient constant,  $k_B$  is Boltzmann's constant,  $T$  is temperature in K, and  $E_{diff}$  is the activation energy for diffusion. Without a driving force, the motion of atoms is random, called Brownian motion, lead to no net flux. In Fick's law, the driving force is a concentration gradient. Atoms move from an area of high concentration to an area of low concentration. Given enough time, the atoms will be distributed uniformly in the containment volume in the absence of any exterior forces. There are three main types of diffusion: surface, grain boundary, and lattice.

Doping is a lattice diffusion process where foreign ions occupy vacant sites in the structure of another material. In C12A7: $e^-$ , cationic dopants can occupy calcium or aluminum sites in the cage framework, as shown in Fig. 1.3, where one niobium ion substitutes an aluminum ion.

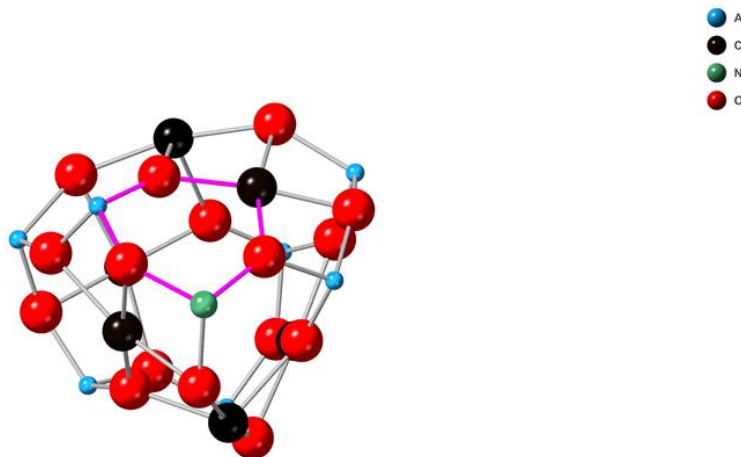


Figure 1.3: Model of aluminum site occupation by niobium in cage structure

Copper has been used to dope metal oxides such as zinc oxide ( $\text{ZnO}$ ). Huang et al was successful in doping  $\text{ZnO}$  nanorods with copper by diffusion doping using furnace heating. A copper foil was held  $\sim 3$  mm from the nanorod array in an argon atmosphere at  $800\text{ }^{\circ}\text{C}$  for up to 6 hours<sup>45</sup>. Another study doped  $\text{ZnO}$  with copper by diffusion doping by annealing coated nanorods in a quartz tube. E-beam evaporation was used to deposit the copper film with a thickness of  $\sim 5$  nm. Annealing was done under vacuum ( $10^{-2}$  Torr) at  $700\text{ }^{\circ}\text{C}$  for 8, 16, and 24 hours. Doped copper cations were determined to be in the divalent state<sup>46</sup>.

Lithium niobate ( $\text{LiNbO}_3$ ), a more complex metal oxide, has also been doped with copper. A copper film was deposited onto polished plates using magnetron sputtering. Samples were heated at a rate of  $340\text{ }^{\circ}\text{C min}^{-1}$  up to  $1000\text{ }^{\circ}\text{C}$  with film thicknesses between  $100 - 900$  nm and hold times ranging from 2 – 20 hours. Copper cations were detected in  $\text{LiNbO}_3$ <sup>47</sup>.

Spark plasma sintering (SPS) is utilized in this study to reduce processing time to synthesize highly reduced C12A7: $\text{e}^-$  compared to calcination using a high temperature furnace with an argon environment or under vacuum.

Spark plasma sintering (SPS) is utilized in this study to reduce processing time for the synthesis of near maximum electron dense C<sub>12</sub>A<sub>7</sub>:e<sup>-</sup> compared to calcination using a high temperature furnace with an argon environment or under vacuum. There are additional advantages to SPS that are discussed in the next section.

#### 1.4 Spark Plasma Sintering

Mayenite electride (C<sub>12</sub>A<sub>7</sub>:e<sup>-</sup>) has been efficiently fabricated by spark plasma sintering (SPS) in prior studies<sup>16, 29, 48–51</sup>. In general, sintering describes the densification of a powder compact at elevated temperatures, usually pressed into a green body prior to heating. The main driving force in sintering is the reduction of Gibbs free energy change by reducing surface area via Equation 1.5,

$$\delta G_{sys} = \delta \int \gamma_s dA_s + \delta \int \gamma_{ss} dA_{ss} \quad (1.5)$$

where G<sub>sys</sub> is the total interfacial energy, A<sub>s</sub> is the specific free surface area, γ<sub>s</sub> is the surface energy, A<sub>ss</sub> is the area of newly created surfaces, and γ<sub>ss</sub> is its energy. Sintering will spontaneously occur while the energy produced by the eliminated free surface area, γ<sub>s</sub>A<sub>s</sub>, is higher than the energy required to form new surfaces, γ<sub>ss</sub>A<sub>ss</sub>. Various factors cause local driving forces such as diffusion promoted by thermal energy, differences in particle size, number of adjacent particles, and morphology of particles. Three stages typically occur during a sintering process. Stage I, the early stage, consists of neck formation between particles primarily driven by surface diffusion. Minimal densification takes place during this stage because particle centers do not move closer. Neck formation creates areas of negative curvature causing rapid diffusion of atoms toward the site transitioning into the next stage. Stage II, the intermediate stage, is characterized by high rates of densification from particle fusion driven by grain boundary diffusion and lattice diffusion. Pores are created in an open network then isolated between

particles fusing together. In stage III, the final stage, pore shrinkage and grain growth ensue.

Materials are very dense entering this stage so only minimal densification can occur.

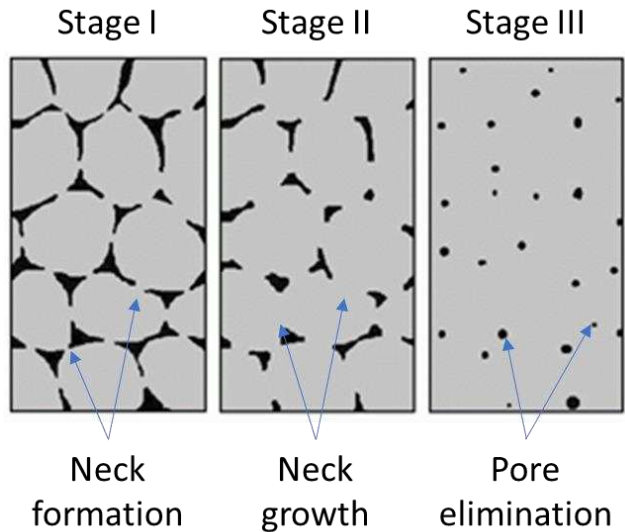


Figure 1.4: Three stages of solid-state sintering<sup>52</sup>

Powder characteristics, heating rates, and presence of mechanical load or an applied electrical field affect the sintering process. Free sintering is the process of heating a packed green body without any other external forces. Herring's scaling law describes how particle size can affect sintering. The same sintering rate can be achieved for smaller particles at lower temperatures or shorter times than larger particles.

Spark plasma sintering (SPS), also referred to as the field assisted sintering technique (FAST), utilizes a pulsed DC current through graphite tooling to achieve high heat rates via joule heating<sup>53</sup>. Fig. 1.5 shows a schematic diagram of a SPS apparatus that includes a DC pulse power connected to electrodes in contact with graphite tooling to create high electron currents that result in high heating rates by joule heating. Sample powders are loaded into a graphite die

between two graphite punches with graphite foil caps to decrease contact resistance. The temperature of samples cannot be directly measure so temperature of the graphite die or a graphite punch near the sample are monitored via thermocouple or pyrometer. The process occurs under vacuum in a vacuum chamber.

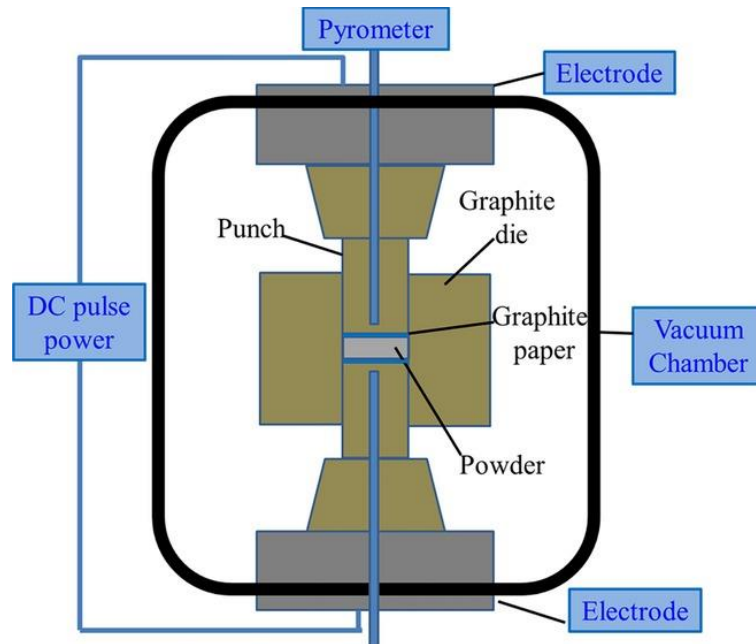


Figure 1.5: Schematic of SPS apparatus<sup>54</sup>

In SPS, the combination of an applied electric field and mechanical load provide a rapid sintering rate. The electrical field promote the mobility of migrating species, allowing for increased diffusion such as Mg in Al<sub>2</sub>O<sub>3</sub><sup>55</sup>. The applied electrical field also increases the concentration of vacancies<sup>56</sup>, defect mobility and diffusivity. Other mechanisms that are commonly referred to as occurrences during SPS include electromigration and thermodiffusion. However, evidence of electromigration is limited in SPS since the applied current mostly passes through surrounding graphite tooling with only low currents passing through specific types of

material. High heating rates achieved through joule heating can cause large temperature gradients in a material being processed, which is the driving force for thermodiffusion. This is the movement of atoms with high thermal energy to an area of low thermal energy. Atomic flux is accompanied by a vacancy flux in the opposite direction. Since  $E_{\text{diff}}$  for each diffusion process is:  $E_{\text{surface}} < E_{\text{grain boundary}} < E_{\text{lattice}}$ , surface diffusion dominates at lower temperatures. High heating rates can limit the amount of surface diffusion that occurs. Applied pressure is required during SPS to ensure good surface contact for the current throughout processing. Mechanical stress also enhances densification by activating plastic deformation or grain boundary sliding. Stress that the powder compact is subjected to is greatest in the initial stage of sintering when powder particles have a low amount of contact surfaces with one another causing higher concentrations in those areas.

The combined contribution of increases in migrating species mobility, vacancy concentration, defect mobility, diffusivity by electric field and thermal driving forces make diffusion doping using SPS an attractive area for research.

SPS has been used to synthesize C12A7: $e^-$  by the solid-state reduction of C12A7 using titanium<sup>16</sup>. Polycrystalline C12A7 was produced by heating CaCO<sub>3</sub> and  $\alpha$ -Al<sub>2</sub>O<sub>3</sub> at 1400°C for 2 hours then crushed into fine powder. After being pressed into a green body in graphite tooling, titanium powder was added to the top and bottom surfaces in equal amounts. Powders were heated in SPS up to 1100°C at a heating rate of 120 °C min<sup>-1</sup>. Samples were held at a uniaxial pressure of 40 MPa under vacuum ( $10^{-2}$  Pa) for 20 minutes. Polycrystalline C12A7: $e^-$  with high conductivity (138 S/cm) and a low work function (2.13 eV) was achieved.

Li et al has applied reactive sintering in the SPS to produce C12A7: $e^-$  without the need for an external reducing agent. A C12A7 + C3A mixture was produced via solid state reaction of

$\text{CaCO}_3$  and  $\gamma\text{-Al}_2\text{O}_3$  in a 27:15 stoichiometric ratio. Powders were heated to 1350 °C for 10 hours then ground into a fine powder producing the precursor material. Aluminum was added to the precursor powder making the Ca:Al stoichiometric ratio 12:14 then processed using SPS. Samples were heated to 1050 °C for 5 minutes at a rate of 50 °C/min. Experiments were done under vacuum ( $10^{-3}$  Pa) with a uniaxial pressure of 60 MPa applied.  $\text{C}_{12}\text{A}_{7:\text{e}^-}$  was produced with a high electron density ( $N_e \approx 2.3 \times 10^{21} \text{ cm}^{-3}$ )<sup>48</sup>. This group also experimented with a one-step synthesis using reactive sintering and SPS processing to eliminate the need for an initial crystallization step using solid state reactions. Precursor  $\text{CaO}$ ,  $\gamma\text{-Al}_2\text{O}_3$ , and Ca powders were mixed in a  $12-x : 7 : x$  stoichiometric ratio using a ball mill in an inert atmosphere with  $0 \leq x \leq 1.6$ . The mixture was then processed in the SPS. This process is shown in Fig. 6.

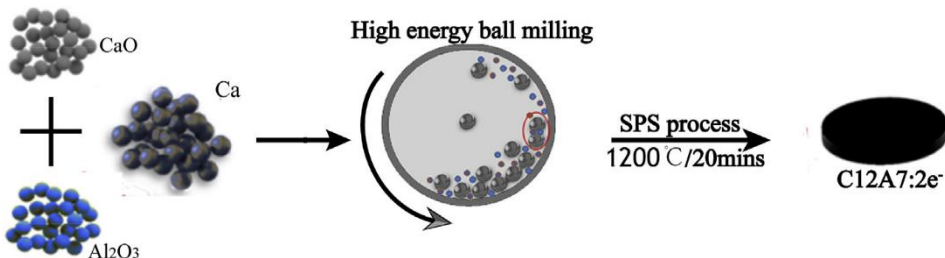


Figure 1.6: Schematic of the one-step synthesis process for  $\text{C}_{12}\text{A}_{7:\text{e}^-}$ <sup>57</sup>

SPS was done at 1000 – 1200 °C for 20 minutes under vacuum ( $10^{-2}$  Pa) with an applied uniaxial pressure of 60 MPa. Heating rate was not reported.  $\text{C}_{12}\text{A}_{7:\text{e}^-}$  with a high electron density ( $N_e \approx 2.1 \times 10^{21} \text{ cm}^{-3}$ ) was obtained<sup>57</sup>.

In this study, SPS is used to fabricate the bulk  $\text{C}_{12}\text{A}_{7:\text{e}^-}$  samples. In addition, my work aimed to utilize the combination of the increased mobility of migrating species, increased

vacancy concentration, increased defect mobility, enhanced diffusivity by electric field, and thermal driving forces to develop a diffusion doping method using SPS.

### 1.5 Motivation and Objectives

As described in the literature review above, extensive research has been done in the fabrication of C<sub>12</sub>A<sub>7</sub> and C<sub>12</sub>A<sub>7</sub>:e<sup>-</sup> to obtain single crystals, thin films, or polycrystalline bulk materials. Experimental studies have been conducted on cationic doping of mayenite, including Mg, Si, Fe, Ga, V and so forth, for which most of the synthesis methods caused a decrease in electrical conductivity. However, cationic doping of C<sub>12</sub>A<sub>7</sub>:e<sup>-</sup> was much less experimentally studied. Therefore, it remains relatively unknown in terms of how to effectively dope C<sub>12</sub>A<sub>7</sub>:e<sup>-</sup>, i.e., fabrication of M-C<sub>12</sub>A<sub>7</sub>:e<sup>-</sup> where M stands for cationic dopants, and how the cationic dopants would affect the crystal structure and electronic properties of C<sub>12</sub>A<sub>7</sub>:e<sup>-</sup>. Moreover, little effort had been put into how to improve the stability of the C<sub>12</sub>A<sub>7</sub>:e<sup>-</sup> at higher temperatures, despite significant progress achieved in studying its crystal structure and electrical conductivity. Higher operating temperatures of C<sub>12</sub>A<sub>7</sub>:e<sup>-</sup> based materials would expand their efficacy for use in ion thrusters or electron transpiration cooling<sup>27</sup>. New insight into the thermal stability and oxidation resistance of cation-doped C<sub>12</sub>A<sub>7</sub>:e<sup>-</sup> will bring in a new frontier in thermionic cooling and thermionic energy conversion as these applications require resistance to oxygen and operating temperatures higher than the reported upper limit of stable temperature for C<sub>12</sub>A<sub>7</sub>:e<sup>-</sup> (400 °C).

Therefore, this study had three-fold objectives: (a) to explore effective and efficient synthesis approaches to produce cation-doped C<sub>12</sub>A<sub>7</sub>:e<sup>-</sup> materials via solid-state diffusion doping, including a novel in-situ SPS doping method; (b) to experimentally identify cationic

dopants that can improve the thermal stability of C12A7: $e^-$ ; (c) to elucidate the effect of select cationic dopants on the structure and oxidation behavior of C12A7: $e^-$ .

Two types of dopants, copper (Cu) and niobium (Nb), were selected in this study as proxy for low valence and high valence dopants, respectively, relative to the Al<sup>3+</sup> and Ca<sup>2+</sup> cations in the C12A7: $e^-$ . Previous modeling work suggested that Cu-doping could alter the cage structure of the C12A7: $e^-$  to open a transport channel, leading to a higher conductivity of the doped C12A7: $e^-$  than undoped C12A7: $e^-$ <sup>40</sup>. In addition, the DFT result predicted that the lattice parameters of both mayenite and C12A7: $e^-$  would be reduced by Cu-doping compared to the undoped counterparts<sup>40</sup>. However, no experimental work had been reported on Cu-doped C12A7: $e^-$  before my study. Thus, its structural and electrical properties were not experimentally verified and its thermal stability was unknown. Based on the DFT work by Huang et al, we hypothesized that the potential reduction in lattice parameter might retard oxygen diffusion and hence, improve the oxidation resistance of C12A7: $e^-$ , finally leading to improved thermal stability at higher temperatures. Therefore, Cu was selected as one dopant candidate in my study. Niobium was chosen as the 2<sup>nd</sup> dopant candidate in this study due to its high valence (+4 and +5) compared to Al<sup>3+</sup> and Ca<sup>2+</sup> in C12A7: $e^-$ , as well as its superconducting and thermal properties<sup>58-60</sup>. To my knowledge, neither computational nor experimental work had been done on Nb doping of C12A7 or C12A7: $e^-$ . Hence, it was hypothesized that Nb might serve as an electron donor to increase the electron concentration in C12A7: $e^-$  and sustain the unique electride properties resulting from the intrinsic anionic electron. Nb dopant was selected with the awareness of high risk due to lack of support from any previous modelling work.

To achieve doping, both diffusion doping in a conventional furnace filled with Ar atmosphere and a novel *in-situ* SPS doping were investigated. Details in materials, synthesis

methods, and experimental procedures are provided in Chapter 2. Chapter 3 describes characterization and testing techniques used for the structural, electronic, and thermal analyses. Results and discussion on the effect of Cu-doping and Nb-doping are presented in Chapter 4 and Chapter 5, respectively. Finally, Chapter 6 will summarize key findings and provide a brief outlook on future research directions.

## CHAPTER 2: Material Synthesis and Doping Process

To achieve the goal of improving thermal stability of mayenite electride (C12A7:e), cationic doping was investigated as a potential solution. Two dopants, copper (Cu) and niobium (Nb), were selected in this study as proxy for low valence and high valence dopants, respectively, relative to the Ca<sup>2+</sup> and Al<sup>3+</sup> cations in C12A7:e<sup>-</sup>. The characteristics of the relevant cations were provided in Table 2.1. The motivation of selecting Cu and Nb as the dopant candidates were briefly discussed in Chapter 1. This chapter will further explain the rationales of dopant selection. In addition, this chapter describes the details of the experimental procedure for material synthesis and doping process. Fig. 2.1 provides an overview of the various processing routes that were investigated in my study. Particularly, diffusion doping in SPS is a novel approach introduced in this study.

Table 2.1: Characteristics of Ca, Al, Cu and Nb elements<sup>61</sup>

<b>Element</b>	<b>Atomic radius</b>	<b>Covalent radius</b>	<b>Ionic radius</b>	<b>Valence states</b>	<b>Electro-negativity</b>	<b>Melting point</b>
	[Å]	[Å]	[Å]			[°C]
Calcium (Ca)	2.23	1.76	1.26	+2	1.0	839
Aluminum (Al)	1.82	1.21	0.675	+3	1.5	660
Copper (Cu)	1.57	1.32	0.86	+1 , +2	1.7	1083
Niobium (Nb)	2.08	1.64	0.78	+2 , +3 , +4 , +5	1.6	2468

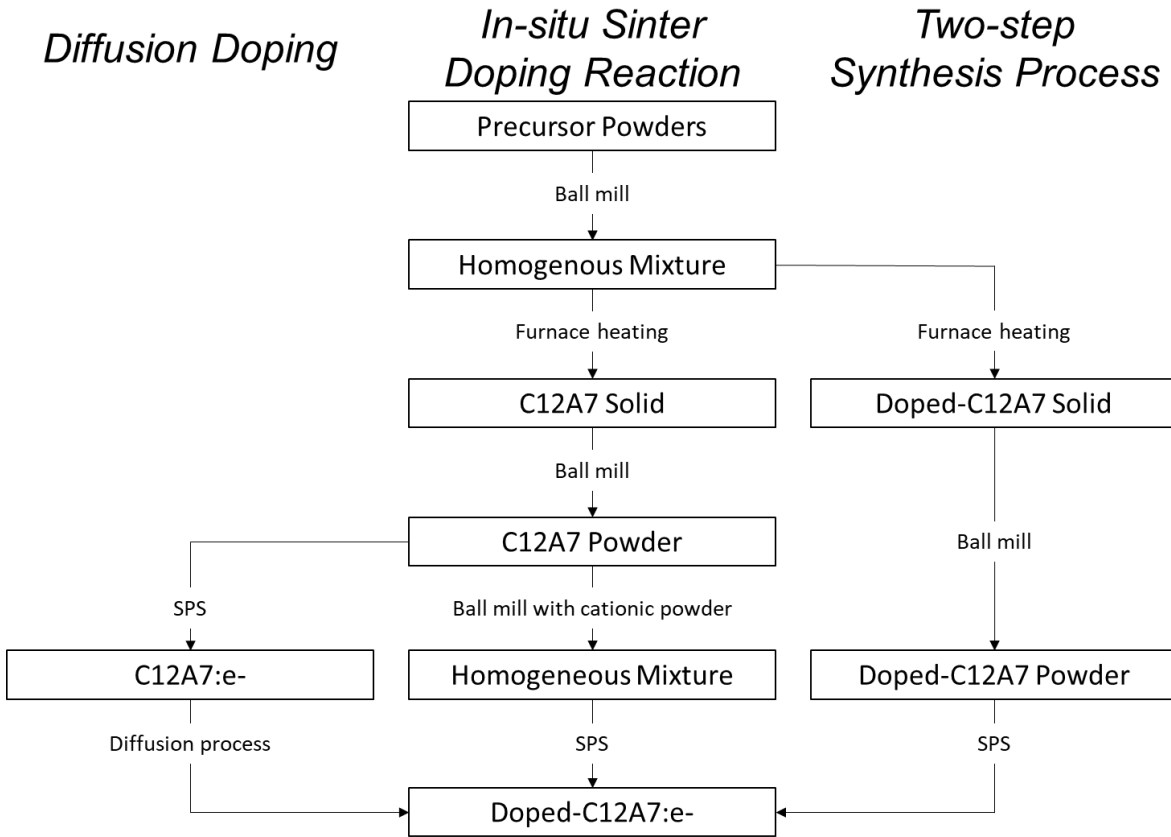


Figure 2.1: Processing flow chart of material synthesis methods used in this study

## 2.1 Synthesis of Materials

### 2.1.1 Mayenite

A precursor powder mixture of  $\text{CaCO}_3$  and  $\text{Al}_2\text{O}_3$  with a 12:7 stoichiometric ratio was ball milled (Across International PQ-N4 planetary ball mill) for a 10-minute run time to create a homogenous distribution of the two types of powders in the mixture. Furnace sintering was utilized to fabricate C12A7 using the precursor mixture in ambient air via solid state reaction (SSR). The first stage of heating brings the powder mixture up to 900°C and  $\text{CaCO}_3$  outgasses  $\text{CO}_2$ , then  $\text{CaO}$  reacts with the  $\text{Al}_2\text{O}_3$  to create Calcium Aluminate phases. The heated powders

were then transferred to a high temperature furnace and held at 1350°C, below the melting temperature of C12A7 (1415°C), for 10 hours to form high purity C12A7.

### 2.1.2 Mayenite Electride

Sintered solid C12A7 is ball milled for a 10-minute run time to form powder. SPS is utilized to consolidate the C12A7 powder and simultaneously reduce it to the electride phase, C12A7: $e^-$ . The powder was loaded into a graphite die and then pressed into a green body. Titanium foil caps were used to catalyze continuous reduction into C12A7: $e^-$ . Sintering parameters were selected including load (15 MPa), pressure (vacuum), heating rate (100 °C/min), hold temperature (1300°C), and hold time (10 min). Samples were cooled to room temperature under vacuum. Further explanation of the C12A7 synthesis and C12A7: $e^-$  reduction processes can be found in previous work<sup>49</sup>.

## 2.2 Dopant Selection

### 2.2.1 Copper

Huang et al<sup>40</sup> used computational methods to model what effects various cationic dopants; including Mg<sup>2+</sup>, Sr<sup>2+</sup>, Cu<sup>2+</sup>, Fe<sup>3+</sup>, Ir<sup>4+</sup>, P<sup>5+</sup>, and V<sup>5+</sup>; would have on C12A7: $e^-$ . Copper was shown to form an electron transfer channel which could enhance the electrical conductivity. Maurelli et al<sup>31</sup> used copper to dope C12A7 with a nominal concentration of 0.86% at, one copper atom per unit cell. The lattice constant of Cu-C12A7 ( $a = 11.974 \text{ \AA}$ ) was found to be smaller than undoped C12A7 ( $a = 11.998 \text{ \AA}$ ). The reduction was attributed to the replacement of calcium ions ( $r = 1.0 \text{ \AA}$ ) by the smaller copper ions ( $r = 0.73 \text{ \AA}$ ). The covalent radius, described as the size of an atom when it forms a covalent bond, for copper ( $1.17 \text{ \AA}$ ) is also less than for calcium ( $1.74 \text{ \AA}$ ) indicating a reduction in the cation-oxygen bond length as Cu occupies Ca sites in the cage framework. Another study synthesized Cu-C12A7 powder that had a higher BET

surface area than the undoped C12A7 produced with the same self-propagating high-temperature method<sup>32</sup>. Higher BET surface area can be attributed to a decreased lattice parameter of the Cu-C12A7. This would be done by creating powder particles with a higher surface area to volume ratio achieved by smaller unit cell size. A reduction in the lattice parameter can contribute to decreased anion mobility due to an increase of the activation energy ( $E_a$ ) for diffusion. In C12A7: $e^-$  cage structures act as a barrier between extra-framework electrons and surrounding atmosphere at room-temperature. Smaller interaction area between adsorbed oxygen and the requirement of higher energy to diffuse oxygen anions into the bulk would improve thermal stability. Our hypothesis is that the inclusion of a Cu-doped C12A7: $e^-$  surface layer will inhibit oxidation of the material at elevated temperatures by acting as a barrier or boundary between the material and atmosphere.

Cu has been successfully doped into other semiconductor metal oxides like zinc oxide (ZnO), in which copper speciation was identified to be in monovalent or divalent states by x-ray photoelectron spectroscopy (XPS)<sup>45, 46</sup>. The copper concentration achieved in that study was 1~2.2 at.% by diffusion doping in high temperature furnaces. In C12A7: $e^-$ , the atomic percentage associated with one Cu ion occupying one Ca<sup>2+</sup> site per unit cell is 0.86%. Lattice reduction is not observed in Cu-doped ZnO, due to the similar ionic radii of zinc (0.74 Å) and copper (0.73 Å). Due to the smaller atomic size, divalent state, predicted effects, successful synthesis of Cu-doped C12A7, and diffusion doping into other metal oxides, Cu was chosen as one dopant candidate for C12A7: $e^-$ .

## 2.2.2 Niobium

Niobium (Nb) is selected as a second dopant candidate because of its performance at high temperatures and its flexible valence states. First, Nb has a high melting point (Table 2.1).

Nb containing alloys were commonly used as coatings for high temperature applications such as aircraft engines<sup>62, 63</sup>. Macroalloyed Nb-Al intermetallic compounds have high oxidation resistance up to 1200 °C. Second, Nb ions have flexible valence states (II, III, IV, and V). Divalent Nb could potentially occupy Ca sites while trivalent and higher states could occupy Al sites in the cage framework of C12A7. C12A7 has been successfully doped by a Nb-similar element, vanadium (V), with each of these valence states in the literature<sup>35</sup>. However, Nb had not been reported as a dopant for C12A7 or C12A7: $e^-$ , neither experimentally nor in modeling work. Hence, selecting Nb as a dopant was a higher risk, but it is worthwhile to investigate. Replacing a small quantity of Al (III) cations with higher valence ions would create ‘holes’ in the electronic band structure which would decrease the energy required for electron conduction, resembling a p-type semiconductor. The hypothesis behind Nb-C12A7: $e^-$  is that doping with Nb (V) can potentially improve oxidation resistance of C12A7: $e^-$  by altering the cage size and increase its conductivity by introducing an acceptor level in the band structure.

## 2.3 Cationic Doping Methods

### 2.3.1 Diffusion Doping in an Argon Furnace

To protect from oxidation without significantly impacting the other material properties of C12A7: $e^-$ , a cation-doped surface layer can be applied to act as a membrane or oxygen barrier coating. Diffusion doping cations into the surface would create a thin layer of cationic-doped C12A7: $e^-$  with a concentration gradient profile while leaving the bulk of the material unchanged. The oxidation rate is limited by the slowest step in oxidation, i.e., adsorption of oxygen on the surface. Thereby, applying an oxygen-resistive outer layer is sufficient to improve thermal stability and meanwhile sustain the electronic properties of the bulk. Cationic doping of C12A7: $e^-$  is a substitutional diffusion process. The initial attempts of Cu doping of was

conducted by diffusion in a conventional furnace (Thermo Scientific Lindeberg Blue M mullite tube furnace with MTI endcaps for vacuum & inert gas control) with an Ar atmosphere using a pure metal in contact with a preformed C12A7:e<sup>-</sup> sample. The diffusion of Cu ions from Cu metal in a low oxygen furnace environment was utilized in the synthesis of Cu doped ZnO nanorod arrays<sup>45</sup>. Samples were prepared by placing a solid C12A7:e<sup>-</sup> disc on top of a Cu layer in an alumina boat with alumina caps put on top to maintain the contact at the Cu - C12A7:e<sup>-</sup> interface throughout heating. Graphite foil was used as a barrier from the surroundings. Two types of Cu, Cu foil (99.9%) provided by Yodaoke and Cu powder (99.5%) with a particle size > 149 µm provided by Consolidated Astronautics, were used. A diagram of the setup is presented in Fig. 2.2a. Furnace heating parameters were carefully selected based on studies that prepared Cu doped metal oxides via diffusion methods<sup>45-47</sup>, The parameters investigated were holding temperature at 700°C and at 900°C, hold time (8 and 16 hours), heating/colling rate (125 °C/hour), gas flow rate (50 ml/min), and applied pressure (5.7 MPa). The heating and cooling rates selected were the maximum capability of the furnace. At the beginning of each run the setup was placed in the center of the furnace, endcaps were fastened, and the furnace underwent three purge cycles before applying a steady gas flow. Time and temperature were varied because diffusion rate and diffusion length are dependent on both variables.

### 2.3.2 Diffusion Doping in Spark Plasma Sintering

Diffusion doping via SPS had not been reported in the literature. Samples were prepared by placing a preformed C12A7:e<sup>-</sup> disk in graphite tooling between two Cu foils. A diagram of the setup is presented in Fig. 2.2b. Cu powder was not used for this method to avoid the sintering of a thick Cu layer onto the surface of the C12A7:e<sup>-</sup> disk. Parameters for diffusion doping experiments in the SPS (Fuji MK 3.2 SPS System) were temperature (700°C, 800°C, and

900°C), hold time (30 min), heating rate (100 °C/min), ambient pressure (< 3 Pa), and applied mechanical pressure (3 MPa). Nb doping was also attempted via SPS diffusion doping. Nb metal disks were sintered using Nb powder with SPS parameters similar to C12A7 synthesis. Sintering temperature was increased to 1400 °C to give a homologous temperature  $T_H = 0.61$  which is considerably lower than  $T_H = 0.72$  for copper at 700°C. A higher temperature could not be chosen due to the melting temperature of C12A7: $e^-$  (1415°C). Samples were cooled under vacuum after processing. Table 2.2 provides a summary of the processing parameters and sample IDs for the various Cu-C12A7: $e^-$  samples.

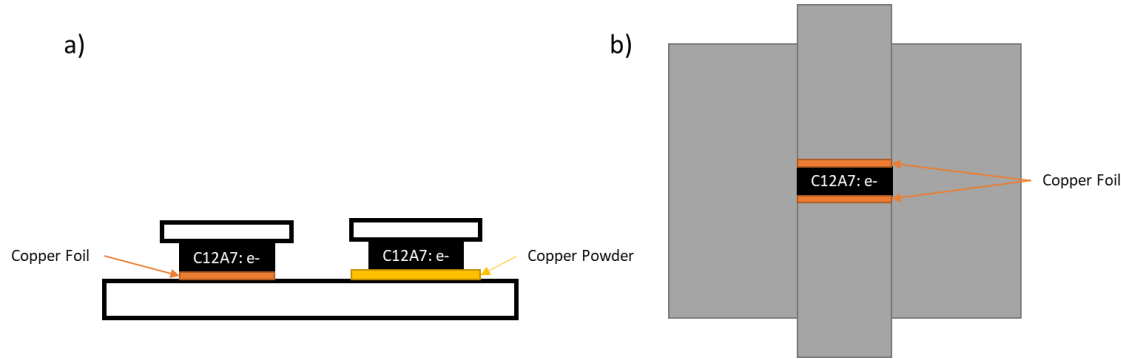


Figure 2.2: Diagram of the set-up of samples in (a) conventional furnace and (b) SPS.

Table 2.2: Summary of the processing parameters for various Cu-C12A7: $e^-$  samples and the corresponding IDs

Sample ID	Method	Processing Parameters				
		Hold Temperature	Heating rate	Copper	Hold time	Pressure
F1	Furnace	700 °C	125 °C/hour	Foil	8 hours	5.7 MPa
F2	Furnace	700 °C	125 °C/hour	Powder	8 hours	5.7 MPa
F3	Furnace	900 °C	125 °C/hour	Foil	8 hours	5.7 MPa
F4	Furnace	900 °C	125 °C/hour	Powder	8 hours	5.7 MPa
F5	Furnace	900 °C	125 °C/hour	Foil	16 hours	5.7 MPa
F6	Furnace	900 °C	125 °C/hour	Powder	16 hours	5.7 MPa
S1	SPS	700 °C	100 °C/min	Foil	30 min	3 MPa
S2	SPS	800 °C	100 °C/min	Foil	30 min	3 MPa
S3	SPS	900 °C	100 °C/min	Foil	30 min	3 MPa

### 2.3.3 Cationic Doping in Preformed Mayenite and Mayenite Electride Powder

Another way to improve oxidation resistance is to alter the entire base material (C12A7: $e^-$ ). Altering the entire sample has a higher possibility of significantly changing material properties or amplifying the changes compared to surface-only modification. Cation-doped C12A7: $e^-$  were synthesized using a modified sol-gel method<sup>41-43</sup> and reduction of cation doped C12A7 synthesized by SSR<sup>15</sup>. These experiments were often performed using a metal oxide containing the dopant in a desired valence state. This concept was adopted to achieve Nb-doping of C12A7: $e^-$  in this study. Preformed C12A7 or C12A7: $e^-$  powder was blended with niobium pentoxide ( $Nb_2O_5$ ) powder and then the powder mixture was densified in SPS, with simultaneous reduction of C12A7 to electride if the feedstock was C12A7+  $Nb_2O_5$ . It was anticipated that diffusion of Nb into the C12A7: $e^-$  lattice would occur at elevated temperatures during the stage III of sintering and simultaneous reduction. Sample A was formed using Niobium metal and C12A7: $e^-$  powders. Sample B was formed using Niobium pentoxide and C12A7: $e^-$  powders. Sample C was formed using Niobium pentoxide and C12A7 powders with Titanium foils to expedite reduction into the electride phase. Each powder combination was ball milled in a 0.1 L agate jar using a 10:1 ball to powder weight ratio for 10 minutes to create a homogenous mixture. Sintering parameters were selected including temperature (1300°C or 1350°C), heating rate (100 °C/min), hold time (10 minutes), ambient pressure (< 3 Pa), and applied pressure (15 MPa). Samples were cooled under vacuum to room temperature.

### 2.3.4 Synthesis of Cationic Doped Mayenite Electride from Precursors

Another process that was attempted was the direct synthesis of cation-doped C12A7 with subsequent reduction into C12A7: $e^-$ . A precursor blend of  $CaCO_3$ ,  $Al_2O_3$ , and  $Nb_2O_5$  powders with a 24:13:1 molar ratio was ball milled for 10 minutes in a 0.1 L agate jar to create a

homogenously dispersed powder mixture. A minimal amount of preformed C12A7 powder was added to the mixture as a phase growing template. The precursor powder mixture was then placed into an alumina crucible and heated in a furnace for reaction sintering and diffusion doping to form Nb-C12A7. The parameters for furnace heating were outgassing temperature at 900°C with a hold time of 10 minutes, and then increase to a temperature at 1300°C or 1350°C with a hold time of 10 or 12 hours for reaction sintering and diffusion doping. Samples were then cooled to room temperature in air. Sintered solids were ball milled for 10 minutes under the same conditions as described previously to rend the sample into powder. The preformed powder was then packed into a graphite die with Ti foils on the top and bottom, cold pressed, and processed in SPS for reduction to the electride phase Nb- C12A7: $e^-$ . SPS parameters were holding temperature (1300°C or 1350°C), heating rate (100 °C/min), hold time (10 minutes), ambient pressure (< 3 Pa), and applied pressure (15 MPa). Samples were cooled to room temperature under vacuum.

In summary, Cu-doping were attempted by diffusion doping in conventional furnace (F-type) or in SPS (S-type). Nb-doping was attempted by a more variety of methods due to lack of literature guidance on the processing approach. Five different methods were investigated to achieve Nb-doping, with sample IDs and detailed parameters provided in Table 2.3. Plan A used Nb metal and C12A7: $e^-$  powders as the starting materials. Plan B used Nb<sub>2</sub>O<sub>5</sub> and C12A7: $e^-$  powders as the starting materials. Plan C used Nb<sub>2</sub>O<sub>5</sub> and C12A7 powders as the starting materials and reduced the C12A7 to the electride phase using Ti foils in SPS. Plan D corresponded to the synthesis method of doping from precursors of C12A7 discussed above (Section 2.3.4). Plan E is the SPS doping method using a Nb metal disk as the Nb-dopant source.

Table 2.3: Summary of the processing routes for various Nb-C12A7: $e^-$  samples and the corresponding IDs.

Type	Powders	Processing	Sample	Conductivity* [S/cm]	Additional parameters
A	Mayenite electride and Nb powder	Ball mill → SPS	A1	0.0710	
B	Mayenite electride Niobium pentoxide	Ball mill → SPS	B1	0.0179	Same parameters as B1
			B2	0.1680	
C	Oxy-Mayenite Niobium pentoxide	Ball mill → SPS reduction with titanium foil	C1	0.0887	Same parameters as C1
			C2	0.0712	
			C3	Unreduced	Fine powder size Same parameters as C3 Higher sintering temperature (1350 °C)
			C4	Unreduced	
			C5	0.0295	
D	Calcium carbonate Alumina Niobium pentoxide	Ball mill → Furnace sintering → SPS reduction with titanium foil	D1	0.1820	Increased atomic percentage of Nb Same as D2 Higher sintering temperature (1350 °C)
			D2	Unreduced	
			D3	0.0657	
			D4	0.0545	
E	Mayenite electride and Nb metal disc	SPS diffusion doping	E1	Melted	Lower sintering temperature (900 °C)
			E2	0.0063	

\*Note: the values of conductivity here were obtained from a 2-probe multimeter, which were significantly underestimated due to the high point-to point contact resistance.

## CHAPTER 3: CHARACTERIZATION AND TESTING

This chapter aims to describe the analysis methods used to evaluate the properties of the various mayenite electride ( $\text{C12A7:e}^-$ ) based samples. The primary phase and presence of any secondary phases were investigated due to impurities reported from literature discussed in Chapter 1. The crystal structure and lattice parameters were characterized to determine the effect of doping. The primary phase of each material and presence of any secondary phases are investigated due to impurities reported from literature discussed in Chapter 1. Changes in lattice parameter were expected due to a difference in atomic size and bond lengths of dopant ions and the framework ions that the dopants substitute for. Differences in valence states, such as the replacement of Al (III) with Nb (V), can affect properties like electrical conductivity or electron density. The electrical conductivity was measured to verify that the electride phase was sustained after the doping attempts. As stated in Chapter 2, the primary goal of this study is to improve the thermal stability of  $\text{C12A7:e}^-$ . Therefore, the onset temperature of mass gain, rates of mass gain, and total mass gain percentage due to oxidation were tested via thermal analysis.

### 3.1 Phase identification and Crystal Lattice Characterization

#### 3.1.1 Powder X-ray Diffraction

Phase identification in each material and calculation of lattice parameters were done using X-ray diffraction (XRD) (Bruker D8 Discover DaVinci). XRD is a technique that utilizes the diffraction of incident X-rays when they encounter atoms that are arranged in different crystal structures. Constructive interference occurs when the Bragg condition is met at a specified angle that is unique to the type of crystal structure and elements, known as Debye-Sherrer cones. Bragg's law, given by Eq. 3.1 below, describes the position (angle) where constructive interference would be the strongest.

$$n\lambda = 2d \sin \theta \quad (3.1)$$

A diffraction pattern is obtained by incident a beam of X-rays with a known wavelength ( $\lambda$ ) onto the material surface while sweeping through a range of angles set between the X-ray source and the detector. Each diffraction peak is associated with a specific plane of the crystal structure. The unique crystal structure of a material creates a specific diffraction pattern. Phases can be identified by matching the Bragg peaks of the pattern with standard values. Using peak positions and known parameters, the interplanar spacing ( $d$ ) of specified planes can be calculated from Bragg's law. With plane spacing and the known Miller indices ( $hkl$ ) for specified peaks, the lattice parameter ( $a$ ) of a phase can be calculated with equation 3.2.

$$a = \sqrt{h^2 + k^2 + l^2} * d_{hkl} \quad (3.2)$$

Using multiple peaks corresponding to different planes, the lattice parameter of the material can be estimated based on averaging. The various samples were polished with a 1- $\mu\text{m}$  diamond suspension finish to reduce lattice strain and remove surface contaminates from processing. Analysis of peak positions is highly reliant upon the distance from the detector so solid samples were leveled to provide consistent parameters. Powder samples were adhered to zero diffraction discs using an amorphous material to nullify any additional peaks. It is worth to note that many calcium aluminate phases have similar crystal structures, which cause overlapping of some diffraction peaks.

### 3.1.2 Scanning Electron Microscopy

Microstructure of the materials was characterized by scanning electron microscopy (SEM) (JEOL 6500 FE-SEM-EDS). SEM utilizes a focused beam of high-energy electrons and the electron-atom interactions on the sample surface to reveal the microstructure and chemical composition of the material. Specifically, detection of secondary electrons determines

morphology and topography, while back scattered electrons show contrasts in chemical composition for multiphase materials. The samples were polished flat with a finishing step of 0.05- $\mu$ m diamond suspension. This would eliminate any morphology or topography variations on the sample surface so that any detected contrasts would be associated with composition variations, which were further analyzed using electron dispersive spectroscopy.

### 3.1.3 Electron Dispersive Spectroscopy

Relative element concentrations and local phases were evaluated with electron dispersive spectroscopy (EDS). SEM and EDS are done concurrently because this technique also uses an electron-atom interaction on the material surface. EDS detectors measure the energy of radiated photons when an electron relaxes from an excited state into a lower energy level. These photons have discrete energies that depend on the element they are produced by. Detection of these radiated photons allow for a qualitative and semi-quantitative analysis of the analyzed surface. Mapping of a specified area shows a relative distribution of elements. Secondary phases and agglomerations of certain elements can be identified. Line scans that produce a spectrum based on position of the line provide variations in chemical composition across particle-bulk or phase-phase boundaries. Spectra taken at specified points within a map can give a relative idea of atomic percentages and the elements present. Mapping was utilized to determine the presence and location of the relative rich area of certain elements, like the Cu and Nb dopant candidates, within the material. When Cu-rich or Nb-rich areas were detected, line scans were used to determine the concentration profile of dopant candidates to qualitatively evaluate the diffusion from the concentrated region into the bulk material. Point spectra were obtained from high-dopant, low-dopant, and non-dopant areas to compare the variations in chemical composition. A limitation of EDS is the ability to detect and accurately determine light atomic elements (atomic

# < 11) which would include oxygen. Therefore, atomic ratios of the cationic elements were used to evaluate calcium aluminate phases and the relative dopant concentrations. The penetration depth of electrons in a C12A7: $e^-$  matrix is not documented; so the interaction volume is unknown for C12A7 or C12A7: $e^-$ , which causes uncertainties in measurements.

### 3.1.4 X-ray Photoelectron Spectroscopy

Material surfaces are the interaction point between an external environment and the bulk material. This boundary is especially important for C12A7: $e^-$  as an electron emitter. X-ray photoelectron spectroscopy (XPS) is a quantitative surface analysis technique with the capability to determine elemental composition, chemical states, and electronic states in a sample surface. XPS was done by PHI Physical Electronics PE-5800 X-ray Photoelectron Spectrometer instrument in this study to determine the valence status of Nb dopant. The analysis depth is 1~10 nm depending on material and analysis parameters. A beam of x-rays is irradiated onto the surface and the kinetic energy (KE) of the electrons ejected from the surface atoms is measured. KE is dependent upon the photon energy ( $h\nu$ ) and binding energy (BE), as shown in Eq. 3.3.

$$BE = h\nu - (KE + \phi) \quad (3.3)$$

A known  $h\nu$  is set using a monochromator in the instrument and KE is detected allowing for the calculation of electron BE. Elements emit electrons with specific BE peak(s) depending on the chemical state of the specific element and which orbital the electron was occupying. An argon bombardment of the surface can etch into the surface to obtain a depth profile or subsurface analysis. This was done before each analysis to remove surface contamination. Each sputtering remove ~5 nm of surface material.

## 3.2 Electrical Conductivity Testing

### 3.2.1 Two-probe Resistance Measurement

Conductivity ( $\sigma$ ) and resistivity ( $\rho$ ) of the samples were calculated using resistance (R), cross-sectional area ( $A_c$ ), and sample thickness (t) using equations 3.4 and 3.5.

$$\rho = R * A_c / t \quad (3.4)$$

$$\sigma = 1/\rho \quad (3.5)$$

Two-probe resistance measurements were taken using a digital voltmeter (CEN TECH p37772) on the as-sintered samples. Removal of titanium or graphite foils adhered to the sample surface from SPS processing and subsequent polishing cause damages to the surface cages in the C12A7:e<sup>-</sup> material, leading to a loss in ohmic contact. As a consequence, the resistance readings are higher than the actual values or not available. Therefore, the thin foils on either face were left intact for resistance and thickness measurements. An advantage of using the two-probe method is its capability of quick determination of conductivity through the entire sample in a non-destructive manner. Probes can also be easily moved to different locations to evaluate conductivity on a single surface to determine if there is limited to no conductivity through the bulk of a sample. However, the results of electrical conductivity obtained by this 2-probe method are preliminary and there are concerns about the accuracy of the values. Resistances are recorded to the deciohm with only one or two significant figures for highly conductive samples. Calculations depend on the accuracy of geometric measurements as well. Manual probe measurements cannot apply an identical amount of force per measurement causing variations in contact resistances. The loss of ohmic contact from polishing made evaluation of conductivities only relative to individual samples before and after processing or analyzing techniques were

performed. It is common that the electrical conductivity of the material is underestimated when a two-probe multimeter is used, due to the high probe-material surface contact resistance.

### 3.3 Thermal Stability Characterization

#### 3.3.1 Thermal Gravimetric Analysis

Mass change in samples as a function of temperature was evaluated using thermal gravimetric analysis (TGA) (Seiko Instruments Inc. RTG220 Robot TG/DTA). The onset of mass gain, total percentage of mass gained, maximum rate of mass gain, and stabilization after mass gain were all analyzed. TGA uses arm balances with an optical detector to sense changes in mass on the scale of micrograms from variations in the arm position. Mass change can occur due to many factors. Outgassing (dehydration) and oxidation are the two main causes of mass change in C<sub>12</sub>A<sub>7</sub>:e<sup>-</sup> when the tests are performed in air or other oxygen-containing atmosphere. At elevated temperatures, C<sub>12</sub>A<sub>7</sub>:e<sup>-</sup> oxidizes by replacing the free cage electrons with occluded oxygen anions. In undoped C<sub>12</sub>A<sub>7</sub>:e<sup>-</sup>, the maximum mass gain percentage (1.16 %) is associated with complete replacement of the electrons by divalent oxygen anions if the sample achieved maximum theoretical electron concentration. The mass gain percentage is often used for the estimation of electron concentration. Mass gain percentage that are lower than the theoretical maximum could result from the presence of secondary calcium aluminate phases in the C<sub>12</sub>A<sub>7</sub>:e<sup>-</sup> samples that were not fully reduced to 100% electride phase during processing. Dopants incorporated into the matrix and secondary phases that readily oxidize can cause higher percentages of mass gain. Therefore, calculation of electron densities for cationic doped C<sub>12</sub>A<sub>7</sub>:e<sup>-</sup> using TGA would be inaccurate. Thermal stability of the materials can be compared relative to one another based on the onset temperature of mass gain, which is attributed to the beginning of oxidation, and the maximum rate of mass gain, which is attributed to the rate of

oxidation. 10~50 mg samples were weighed then placed into a platinum crucible. The parameters for TGA were maximum temperature (1100 °C), heating rate (10 °C/min), gas type (N<sub>2</sub> balanced - 5% O<sub>2</sub> or Argon), and gas flow rate (50 ml/min). In other studies, there is a mass loss that occurs between 900 and 1350 °C attributed to the transition of occluded oxygen anions from superoxide ions (O<sup>-</sup> and O<sub>2</sub><sup>-</sup>) to divalent oxide ions (O<sup>2-</sup>) because it is more thermodynamically stable at elevated temperatures<sup>51</sup>. Material behavior in the higher temperature region between 1100 and 1400 °C could not be analyzed due to instrument constraints.

### 3.3.2 Differential Thermal Analysis

Exothermic and endothermic processes in a material during heating can be determined using differential thermal analysis (DTA). DTA and TGA can be ran concurrently using the same equipment. This technique uses thermocouples attached to stages with one holding the reference and the other containing the sample to detect differences in energy needed to heat the sample stage. These differences are represented by peaks. Various processes are associated with thermal changes such as evaporation of adhered water, oxidation, phase transformation, and so forth. Enthalpy can be determined by integrating the peaks. DTA equipment must be carefully calibrated using a material standard for quantitative analysis.

## CHAPTER 4: EFFECT OF COPPER DOPING ON MAYENITE ELECTRIDE

This chapter discusses the results of Cu doping mayenite electride ( $\text{Cu-C12A7:e}^-$ ). Phase and structural analyses revealed that Cu doping was successfully achieved by both furnace heating in argon atmosphere (F-type) and the *in-situ* SPS doping approach (S-type). Thermal analysis results suggested that Cu-doping effectively improved the electrical conductivity, oxidation resistance, and thermal stability compared to undoped C12A7: $e^-$ . Finally, the novel spark plasma sintering (SPS) diffusion process efficacy is addressed.

### 4.1 Phase Constitution and Microstructure

Fig. 4.1 displays the representative XRD patterns for select F-type and S-type Cu-C12A7: $e^-$  samples in comparison to the undoped C12A7: $e^-$ . All patterns were normalized so that the peak intensity can represent the relative amounts of individual phases. Peaks corresponding to Cu metal phase were observed in F-type samples, suggesting that some Cu was present as a metal phase in these samples which can be seen in F3 and F4. Sample F4, processed in contact with Cu powder, exhibited a higher relative amount of Cu phase than F3, processed in contact with Cu foil. It is worth noting that F3 and F4 were processed simultaneously in the same furnace experiment. S-type Cu-C12A7: $e^-$  samples and undoped C12A7: $e^-$  presented as single phase C12A7: $e^-$  in diffraction patterns. Peaks for secondary calcium aluminate phases CA and C3A were also observed in F-type samples. Small peak shifts resulted from changes in lattice parameter and is to be discussed later. The presence of excess Cu disrupted local Ca/Al stoichiometric ratios causing the secondary calcium aluminate phase formation in Cu-rich regions. This would explain the presence of CA and C3A in samples that contain Cu metal phase (F3 and F4) and the presence of single phase C12A7: $e^-$  in the sample that does not show Cu metal phase, e.g., S2.

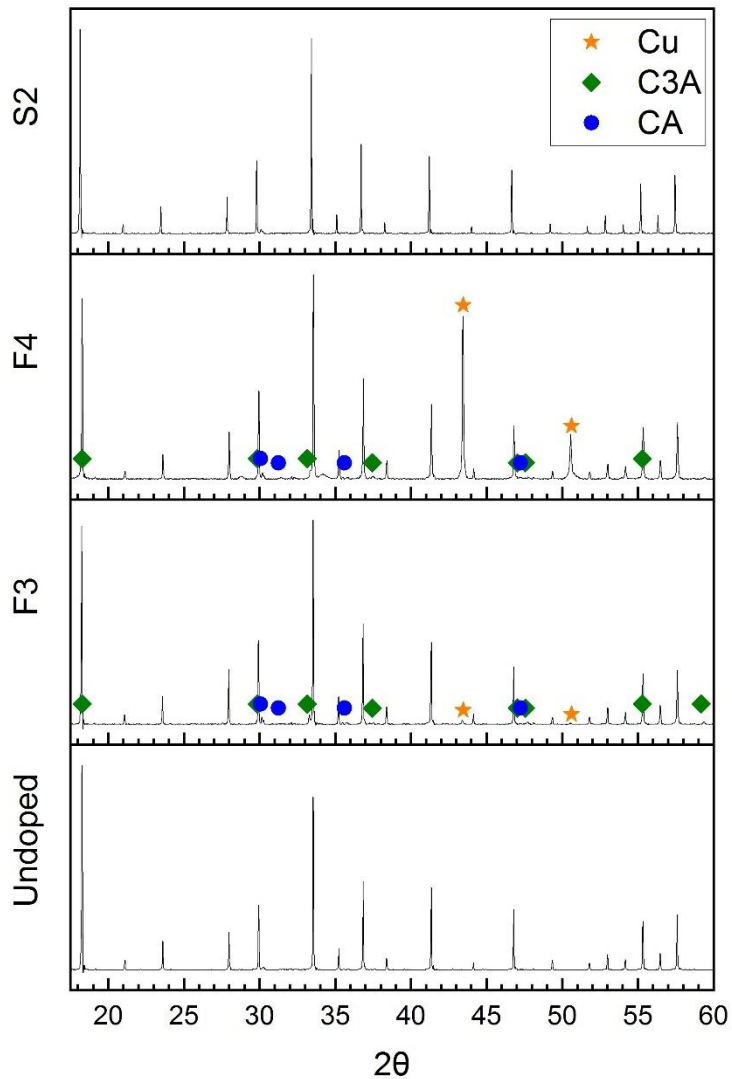


Figure 4.1: X-ray diffraction (XRD) patterns of undoped C12A7: $e^-$ , F3, F4, and S2. The unindexed peaks correspond to the C12A7: $e^-$  phase.

The microstructure of all Cu-C12A7: $e^-$  samples were examined in optical microscope and SEM. Fig. 4.2 displays representative microstructure of the F-type Cu-C12A7: $e^-$  sample surface. Metallic copper was present on the sample surface after F-type processing. F3 and F5, which used Cu foil as the diffusion source, only exhibited formation of Cu regions at the edge of contacted faces. During sintering Cu foil bonded to the C12A7: $e^-$  samples and when removed left residue Cu metal on the edges. Fig. 4.2a shows the boundary between Cu and C12A7: $e^-$  formed

on F3 surface. The interface between metallic Cu (light grey) and the nominally Cu-C12A7:e<sup>-</sup> (dark grey) was clearly visible in SEM (Fig 4.2c). Formation of Cu regions covered the entire contact surface of F2, F4, and F6 (Fig 4.2b), which used Cu powder as the dopant source.

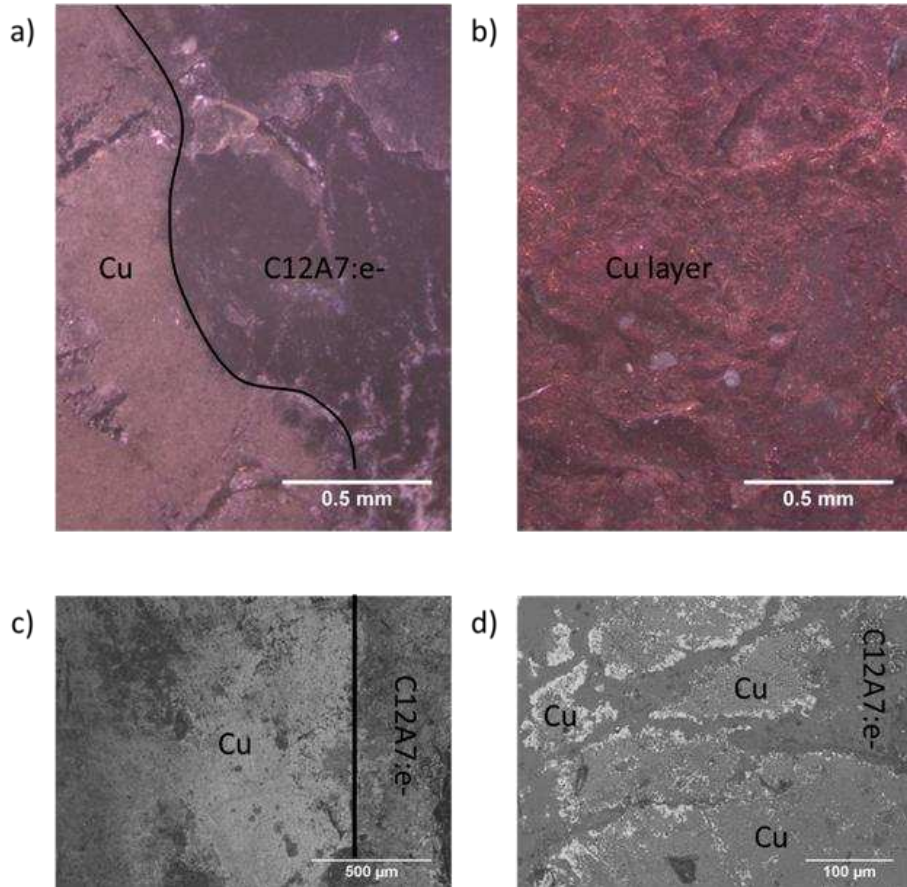


Figure 4.2: Optical images of the (a) F3 surface and (b) F4 surface, and SEM images showing (c) the Cu-C12A7:e<sup>-</sup> boundary on F3 and (d) the copper surface layer on F4

Surface diffusion is the dominant mechanism of mass transport at moderate temperatures for a significant time length due to low heating rates (125 °C/hr) used in F-type processing. Both the Cu surface layer sintered from Cu powder and the bonding of Cu foil resulted from surface diffusion. As the furnace reached hold temperatures and provided a steady thermal energy, the sintered Cu regions continued to transport atoms into the bulk C12A7:e<sup>-</sup> by grain boundary and lattice diffusion. In comparison with the Cu powder - C12A7:e<sup>-</sup> contact interface, the Cu foil -

C12A7:e<sup>-</sup> interface had an ‘infinite curvature’ (relatively flat) attributed to mitigating Cu surface diffusion. The F4 cross-section SEM images (Fig. 4.3) showed Cu diffused up to a depth, or diffusion length, of ~ 100 µm from the surface Cu powder - C12A7:e<sup>-</sup> interface. Sub surface Cu atoms indicated grain boundary or lattice diffusion.

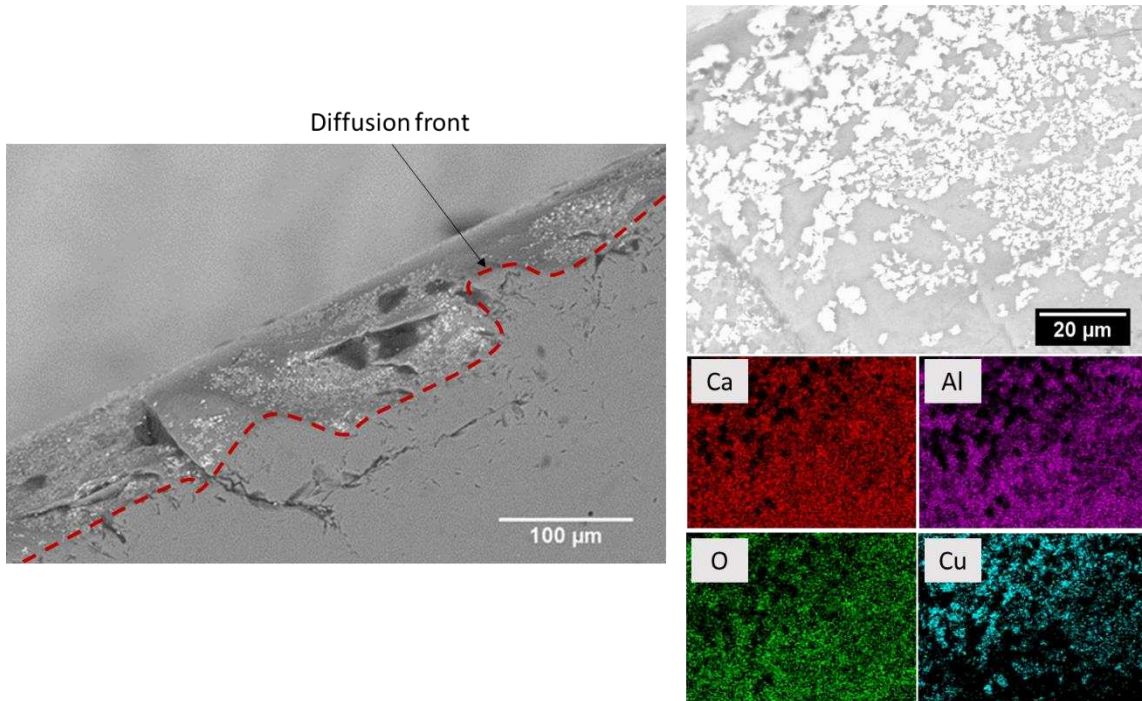


Figure 4.3: SEM images and EDS maps of the cross-section of F4

Cu-rich regions at the diffusion front were further analyzed with EDS line scans (Fig. 4.4). Concentration profiles across the visible particle – bulk interface displayed a gradual concentration gradient of each element. As the location approached the white regions, the Cu concentration increased while the concentrations of Ca, Al, and O decreased.

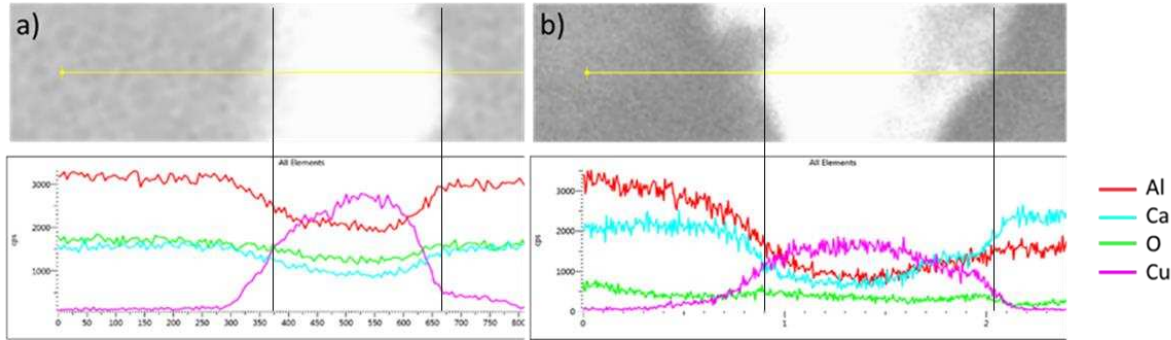


Figure 4.4: EDS line scans of Cu regions at the diffusion front

A spread function given in Eq. 4.1<sup>64</sup> described the Cu concentration profile in the C12A7: $e^-$ .

$$c(x, t) = \bar{c} + \Delta c \cdot \text{erf}\left(\frac{x}{\sqrt{4Dt}}\right) \quad (4.1)$$

For Eq. 4.1  $c(x,t)$  is the concentration of Cu at a distance  $x$  from the average concentration at time  $t$ ,  $\bar{c}$  indicated by black lines in Fig. 4.4.  $\Delta c$  is the initial concentration difference of Cu between the particle and bulk and  $D$  is the diffusion coefficient. Concentration gradients into the sample suggest Cu atoms undergo lattice diffusion into C12A7: $e^-$ , which is the main mechanism for solid state diffusion doping.

Changes in the Ca/Al ratio were also observed, as shown in Fig 4.4b. The difference in Ca/Al ratio on either side of the Cu-rich region suggested a secondary calcium aluminate phase. The phase with a higher concentration of Al is presumed to be C12A7: $e^-$  while a higher Ca content indicated C3A phase presence. This observation was consistent with C3A peaks identified in the XRD pattern. Previous study on Cu-C12A7 reported the formation of other calcium aluminate phases<sup>31</sup>. Maurelli et al. determined that Cu atoms occupy calcium sites as divalent cations. Excess Cu therefore increases the Ca(Cu)/Al ratio resulting in the observed C3A phase formation. The Cu foils were investigated due to coloration observed after thermal processing. Fig 4.5 displays SEM and EDS of calcium aluminate phase(s) on Cu foil.

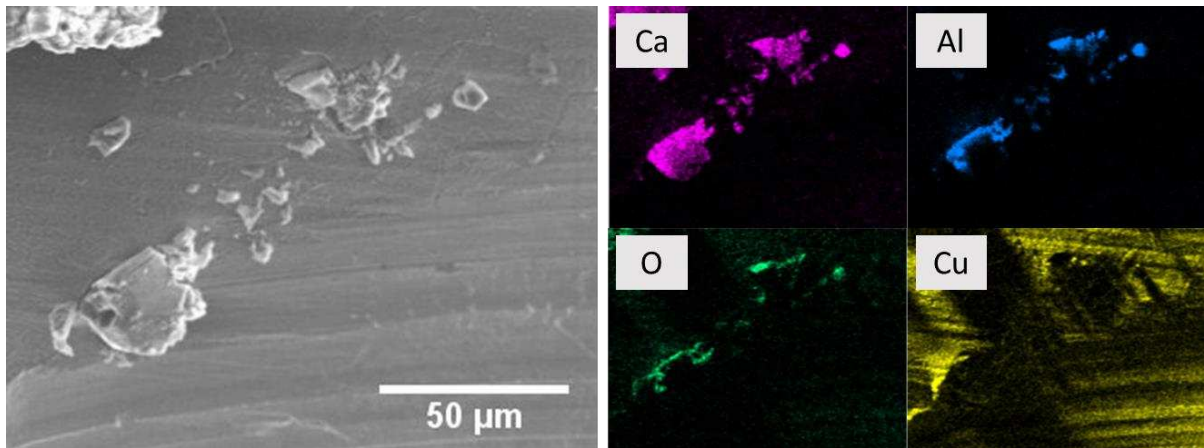


Figure 4.5: Post processing (a) SEM image and (b) EDS maps of Cu foil surface

The concentration gradients created by Cu-rich foil and Ca, Al, O-rich C12A7: $e^-$  are the main driving force for Cu diffusion into C12A7: $e^-$ , coupled with a flux of calcium ions, aluminum ions, and oxygen ions from C12A7: $e^-$ . Cu atoms at the interface were oxidized to Cu ions,  $Cu \rightarrow Cu^+$  or  $Cu^{2+}$ , and then Cu cations diffuse into the C12A7: $e^-$  lattice site by substituting the Ca cations. The presence of Ca-rich regions on Cu foil post thermal process supported Cu cation occupation at  $Ca^{2+}$  cation sites and is consistent with Cu-C12A7 studies<sup>31, 32</sup>. To my knowledge, this was the first time that Cu-C12A7: $e^-$  was experimentally synthesized.

In contrast, the S-type Cu-C12A7: $e^-$  samples did not exhibit large Cu-rich regions. Rather, the distribution of Cu element was scattered on the sample surface. Representative SEM and EDS mapping results are shown in Fig 4.6. Compared with F4 sample, Cu powder dopant source, the contact between the Cu-foil and the solid C12A7: $e^-$  disks in SPS provided more homogeneous diffusion paths for Cu, resulting in a uniform distribution of Cu across the sample. In addition, the relatively flat interface between the Cu foil and C12A7: $e^-$  along with the high heating rates of SPS limited surface diffusion. As a result, grain boundary and lattice diffusion

dominated during SPS diffusion, promoting incorporation of Cu into bulk C12A7: $e^-$  without forming a Cu metal region on the surface. Moreover, the thermal gradient and electrical field applied during SPS accelerated diffusion kinetics<sup>53</sup>, and thus, reduced the time length required for effective doping. Detection of Cu on the surface either visibly in an optical microscope, or in SEM/EDS maps does not guarantee Cu diffused into the C12A7: $e^-$  framework as a dopant. Therefore, the lattice parameter of C12A7: $e^-$  in both F-type and S-type Cu-C12A7: $e^-$  samples was calculated, to be discussed in next section.

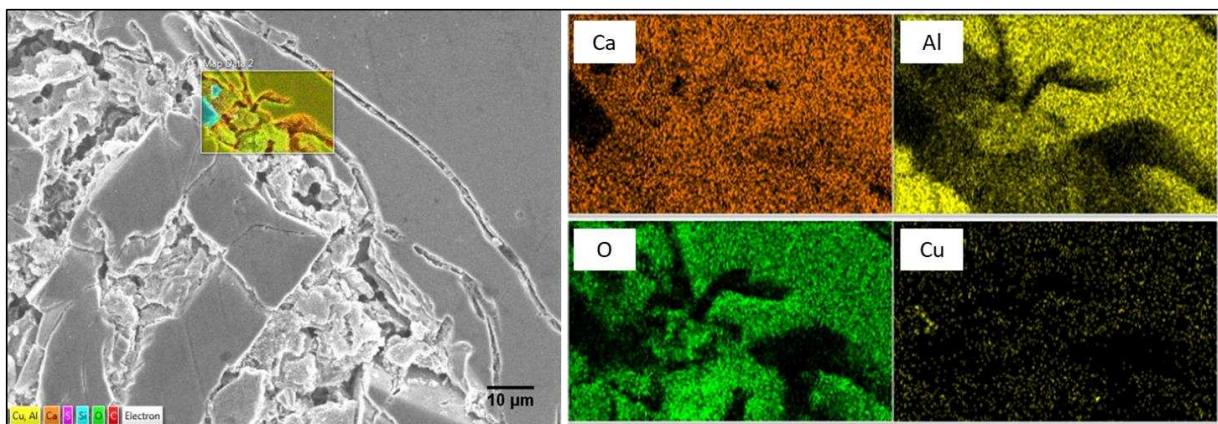


Figure 4.6: SEM image and EDS maps of S2 surface

#### 4.2 Structural Analysis

The lattice parameter of C12A7: $e^-$  in Cu-C12A7: $e^-$  and undoped C12A7: $e^-$  were determined from peak positions in XRD patterns. Peaks shifted to higher diffraction angles (see Fig. 4.7a) in F-type and S-type samples which confirmed reduced lattice parameters. It was found that the lattice parameter of C12A7: $e^-$  ( $a = 11.981 \text{ \AA}$ ) is smaller than that of C12A7 ( $a = 12.016 \text{ \AA}$ ). Fig. 4.7b demonstrated that Cu-doping further reduced the lattice parameter of C12A7: $e^-$ . Particularly, S2 exhibited the smallest lattice parameter,  $11.942 \text{ \AA}$ . Similar lattice parameters achieved by F3 ( $a = 11.943 \text{ \AA}$ ) and F4 ( $a = 11.944 \text{ \AA}$ ) suggested Cu doping was

successfully achieved in all three. The  $0.039 \text{ \AA}$  decrease in lattice parameter was comparable to the  $\Delta = -0.025 \text{ \AA}$  change reported for Cu-doped C12A7<sup>31</sup>.

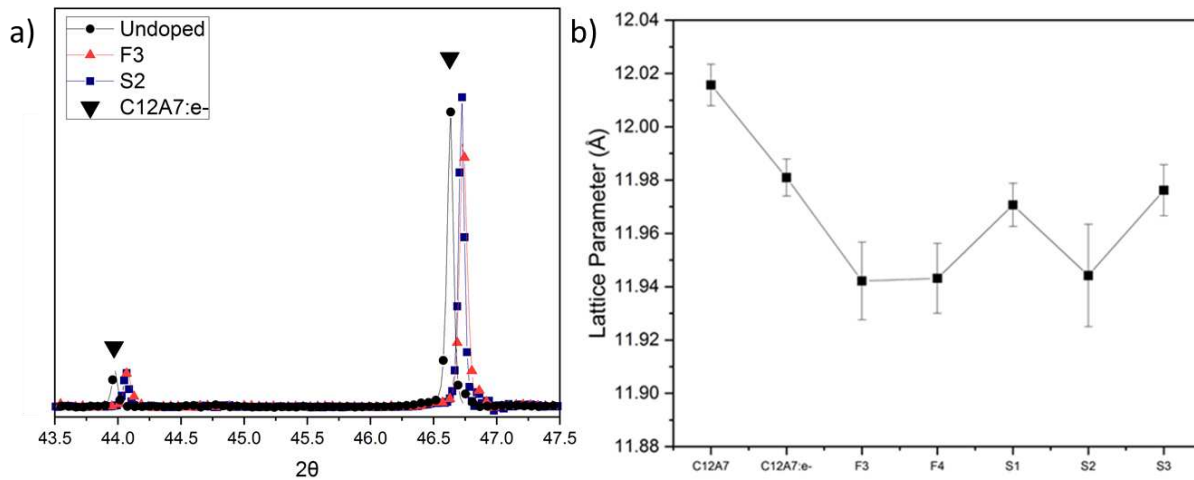


Figure 4.7: (a) XRD pattern of C12A7: $e^-$  peaks for undoped C12A7: $e^-$ , F3, and S2 and (b) lattice parameters of the C12A7: $e^-$  in undoped and Cu-C12A7: $e^-$  samples

The nominal concentration of Cu in Cu-doped C12A7 in reference <sup>31</sup>, was one atom per unit cell, corresponding to  $\sim 0.86$  at%. A larger reduction in lattice parameter indicated the average Cu dopant concentration in the subsurface of S2, up to the diffusion depth, was higher. Ga and Co doped C12A7 derivatives are reported stable up to  $x = 1$ , corresponding to a dopant concentration of  $\sim 1.62$  at %. Secondary calcium aluminate phases begin to form due to excess dopant concentrations<sup>34, 38, 44</sup>. The other S-type samples S1 ( $a = 11.971 \text{ \AA}$ ) and S3 ( $a = 11.976 \text{ \AA}$ ) did not show a significant decrease in lattice parameter. In comparison to S2, the conventional furnace heating method for F3 and F4 samples used higher temperature ( $900 \text{ }^\circ\text{C}$ ) and took 16 hours to obtain a similar lattice parameter. Extending the holding time via furnace heating indicated no further decrease in lattice parameter could be achieved. Despite the minimal

reduction in lattice parameter, S1 and S3 were included for further analysis as Cu-doping was successfully achieved.

#### 4.3 Electrical Conductivity

The electrical resistance was measured by a two-probe multimeter and four-probe physical property measurement system (PPMS). As-fabricated samples were first measured by two-probe multimeter as a quick and preliminary testing, then the electrical conductivity was calculated based on measured resistance and sample geometries. Subsequently, a more delicate four-probe method was utilized to measure the electrical conductivity via PPMS. Fig. 4.8a and 4.8b shows a diagram of the two-probe and four-probe resistance analysis techniques, respectively. When a multimeter is used, two probes were placed on the opposite circular faces giving electrical resistance from point contacts. In contrast, the PPMS uses planar contacts along specimens machined into rectangular parallelepipeds then attached with four Cu leads equally spaced, giving more accurate electrical resistance measurements and conductivity calculations. It is important to note Cu leads were attached using an electrically conductive paste that improved ohmic contact.

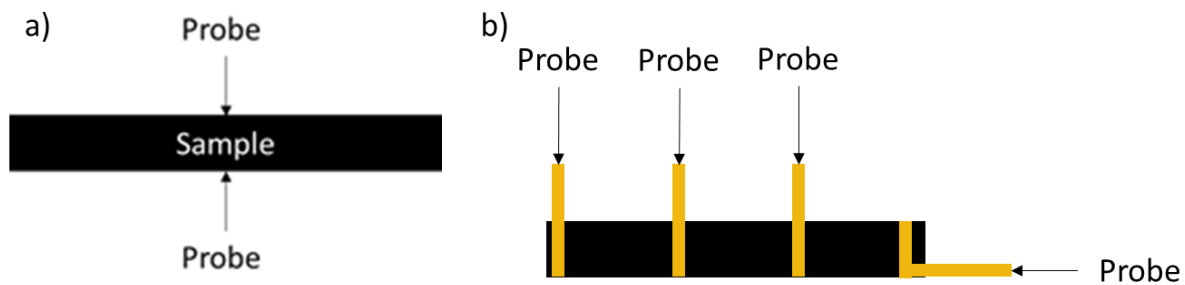


Figure 4.8: Electronic conductivity measurement diagram for the (a) two-probe and (b) four-probe testing

Based on measurement by a two-probe multimeter, as-sintered C<sub>12</sub>A<sub>7</sub>:e<sup>-</sup> had an electrical conductivity ( $\sigma = 0.106 \text{ S/cm}$ ), on the same order of magnitude as polycrystalline C<sub>12</sub>A<sub>7</sub>:e<sup>-</sup>

reported in other studies that used two-step solid-state synthesis and reduction<sup>15</sup>. Undoped C12A7:e<sup>-</sup> exhibited a comparable electrical conductivity (103.7 S/cm) to the maximum obtained using a similar synthesis method (138 S/cm) by four-probe measurements. Well-polished C12A7:e<sup>-</sup> samples showed an overload reading of electrical resistance when tested by a two-probe multimeter due to loss of ohmic contact from mechanical polishing and limited point contact between the probe tips and sample. F-type samples had a resistance higher than the upper limit detectable by the multimeter. The formation of a thin Cu layer on the surface did not provide a sufficient pathway for ohmic contact to be restored. Possible reasons for this included (1) the secondary calcium aluminate phases, such as C3A and CA, formed at the interface between Cu-rich region and C12A7:e<sup>-</sup> cut off the electron conduction path; (2) the sintered Cu does not form a coherent interface with C12A7:e<sup>-</sup>, or (3) atmospheric molecules adsorb onto the sample surface causing an insulative behavior.

The electrical resistance of S-type Cu-doped C12A7:e<sup>-</sup> samples were detectable using the multimeter, which was further converted to electrical conductivity, provided in Table 4.1. S2 showed minimal change in electrical conductivity ( $\sigma = 0.127$  S/cm) compared to the undoped counterpart. S1 and S3 had a lower conductivity ( $\sigma = 0.017$  S/cm and  $\sigma = 0.042$  S/cm) compared to undoped C12A7:e<sup>-</sup>. We do not know the concentration or diffusion length of copper atoms within Cu-doped C12A7:e<sup>-</sup>, however it is assumed that only a thin surface layer of Cu-doped C12A7:e<sup>-</sup> is achieved during the short (< 40 minutes) hold time. The inner bulk sample remained undoped C12A7:e<sup>-</sup>. Therefore, a minimal change in electrical conductivity was anticipated. It is a promising sign that the Ohmic contact was sustained after copper incorporation into the C12A7:e<sup>-</sup> cage structure via SPS doping, indicating a leap toward industrial production and use of M-doped C12A7:e<sup>-</sup> materials. The RT conductivities from PPMS measurement of S-type Cu-

doped C12A7: $e^-$  samples are also provided in Table 4.1. In general, the conductivities from PPMS were higher than those values obtained from a multimeter. This is because of the 4-probe set-up in PPMS and larger planar contact area, in contrast to the 2-probe point contact when a multimeter is used (Fig. 4.8). The important point to take away was that S2 showed an increase in electrical conductivity. The primary goal of this study was to improve the thermal stability of the C12A7: $e^-$  by cationic doping. Therefore, the thermal stability of the Cu- doped C12A7: $e^-$  samples was investigated by thermal analysis and the results is to be discussed in next section.

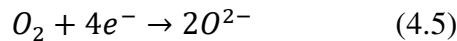
Table 4.1: Electrical conductivities of C12A7: $e^-$  and Cu-C12A7: $e^-$  at room-temperature

SAMPLE	TWO-PROBE CONDUCTIVITY [S/cm]	PPMS CONDUCTIVITY [S/cm]
C12A7: $e^-$	0.106	103.7
F1	Overloaded resistance	2.4
S1	0.017	6.5
S2	0.127	389.4
S3	0.042	61.9

#### 4.4 Thermal Stability

Fig. 4.9 shows the TG and DTA curves of S-type doped samples compared to the undoped C12A7: $e^-$ . Three distinct regions were observed below 1050°C. Region I is characterized by a steady mass gain at a low rate up to ~500°C with a mass gain percentage of 0.165%, 0.181%, and 0.133% for S1, S2, and S3, respectively. Undoped C12A7: $e^-$  samples experienced a mass gain less than 0.1% in this region. Region II is characterized by linear mass gain behavior with a relatively constant rate, higher than the rate in Region I. It was observed that the mass gain rate followed an order of S1<S2<S3<undoped C12A7: $e^-$  in this region. However, S1 exhibited a transition at about 850°C to another subregion that had a higher mass gain rate. Region III exhibited steady mass gain again, with a low rate up to 1050°C, the maximum testing temperature. S2 had the lowest percentage of final mass gain (0.928%)

followed by S3 (1.058%), C12A7: $e^-$  (1.113%), and S1 (1.326%) shown in Fig 4.9a. All mass gains during the thermal analysis were attributed to the uptake of oxygen from the testing medium, air. In other words, oxidation occurred to the specimens during the heating in all specimens. However, the onset temperatures at which the rapid oxidation started were varied among the samples. The transition from the steady region I to the rapid oxidation region II is also reflected as an exothermic peak in the DTA curve (Fig. 4.8b). For the undoped C12A7: $e^-$  specimen, this exothermic peak occurred at 575°C, while all three S-type Cu-C12A7: $e^-$  samples exhibit the first exothermic peak at 625°C. Initial slow mass gain in Region I resulted from the adsorption of oxygen from the surrounding environment onto the material surface. The first inflection into a rapid mass gain accompanied by the 1st exothermic peak in DTA represented that oxygen molecules adsorbed on the surface reacted with the encaged electrons in C12A7: $e^-$  to form O<sup>2-</sup> anions per Reaction 4.5 which caused a phase change.



Consequently, rapid oxidation occurred to the C12A7: $e^-$ . Undoped C12A7: $e^-$  has the largest initial exothermic peak followed closely by S3, then S2 and S1, which exhibited significantly smaller peaks. The peak intensity is proportional to the degree of inflection in the mass gain rate. Increase of the reaction onset temperature by ~ 50°C indicated improvement in the oxidation resistance. The second change in mass gain rate (a decrease in oxidation rate highlighted by circles in Fig. 4.9a), signaling transition from region II to region III, also corresponded to an exothermic peak in the DTA curves (Fig. 4.9b), which occurred at different temperatures for the various samples. The order of the peak temperatures, from higher to lower, was S1 (950°C), S2 (800°C), S3 (790°C) and C12A7: $e^-$  (655°C).

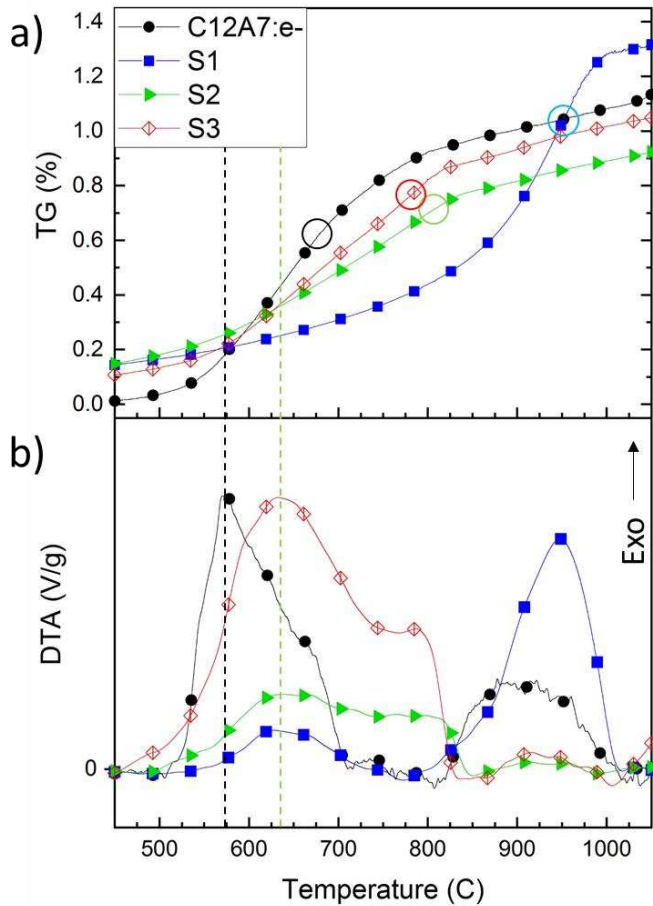
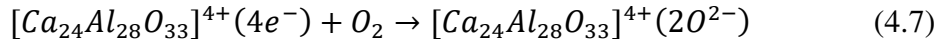


Figure 4.9: (a) Thermalgravimetric mass gain and (b) differential thermal peaks of S-type samples in comparison to an undoped counterpart. The dash lines match the 1<sup>st</sup> exothermic peaks in DTA curves for the various samples with the first change in mass gain rates in TG curve; the various circles in TG curve correspond to the 2<sup>nd</sup> exothermic peaks in DTA curves for the various samples.

Subsequently, an equilibrium proceeded through region III with a constant mass gain rate lower than that in region II, resulting from the adsorption of oxygen from the environment and subsequent conversion. Xiao et al tested C12A7:e<sup>-</sup> by TG/DTA up to 1350 °C in 70% argon 30% oxygen, where a maximum mass gain was achieved after a second influx of oxygen<sup>51</sup>. This was attributed to the formation of superoxide anions via the equilibrium reaction below<sup>51, 65</sup>.



After an apex was reached the specimen started to decrease in mass as temperature continued to increase, indicating a shift to the left in reaction 4.6. It should be noted that the maximum temperature tested in this study is lower than the temperature mass loss was observed. At the upper temperature limit (1350°C) a mass gain of 1.178% was achieved, corresponding to the theoretical maximum gain for oxidation of fully reduced C12A7: $e^-$  given by Reaction 4.7.



The delay in the oxidation onset and peak temperatures for S-type specimens suggested that copper doping on the C12A7: $e^-$  surface retarded the reaction between adsorbed oxygen and extra-framework electrons in C12A7: $e^-$ , and thus improved thermal stability compared to undoped C12A7: $e^-$ . Lower mass gain rates in Region II and lower overall mass gain percentages at 1050°C further supporting an increase in the oxidation resistance was achieved.

To further understand the oxidation behavior at the transition from region I to region II, C12A7: $e^-$  specimens were heat treated in the TG to 550°C, 600°C, and 650°C then taken out for characterization of the surfaces (Fig. 4.10). It was observed that one face of the C12A7: $e^-$  specimens was fully oxidized at 550°C, which was near the onset of the exothermic peak. At 550°C, oxygen adsorbed to the surface started to react with the anionic electrons in the C12A7: $e^-$ , creating oxide anions, which replaced the encaged electrons as extra-framework anions to maintain the neutral charge. As a result, C12A7: $e^-$  transformed to oxy-C12A7. The specimen heated to 600°C showed a diffusion front from the original sample surface (Fig. 4.10b). The distinct color change in the side view represented the oxidation front, with white (bright) corresponded to oxy-C12A7 and black (dark) corresponded to C12A7: $e^-$  (or limited oxidized electride). An oxidation front originated from one surface indicated that certain surface areas were preferable for either oxygen adsorption from the atmosphere or oxygen – electron

interaction to produce  $O^{2-}$  anions. This preference most likely stemmed from some surface characteristics, such as damaged cages or defect-rich (e.g., O-vacancies) regions or favorable adsorption onto the smooth surface, that promoted oxygen adsorption or oxygen diffusion. It should be noted that the surface from which the diffusion front originated was well-polished while the sides of specimen were roughly cleaved from brittle fracture.

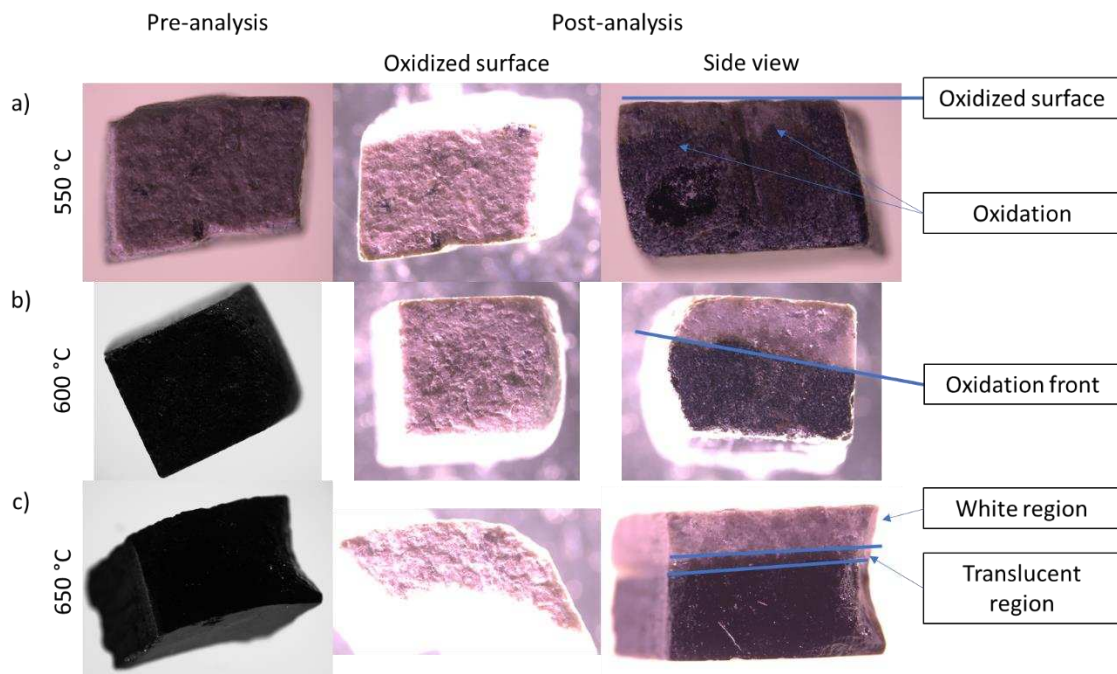


Figure 4.10: C12A7: $e^-$  specimens thermally analyzed to (a) 550°C, (b) 600°C, and (c) 650°C

The specimen heated up to 650°C, near the peak temperature of the exothermic reaction corresponding to the highest rate of mass gain for all C12A7: $e^-$  specimens, also exhibited a uniform oxidation front (Fig. 4.10c). In addition, a translucent layer was observed between the top white oxidized region and the dark C12A7: $e^-$  region. Since diffusion length increases as temperature increases as the reaction continues, eventually the low concentration of electrons and long diffusion path slow the reaction causing a transition from region II to region III.

To provide insight into the thermal stability of C12A7: $e^-$  and the associated oxidation or phase transformation, C12A7: $e^-$  specimens were also heat treated in air using a furnace. The color change, which was commonly used as a preliminary judgement on phase transformation in the field of C12A7 and C12A7: $e^-$ , of the same sample for the full temperature range, room temperature to 1350°C, with a 50°C increment, was examined. The thermal stability of the C12A7: $e^-$  was to be used as a baseline to compare with the doped samples. While the TG analysis recorded the mass change (gain or loss), it did not provide the real-time examination of the sample color change. In contrast, furnace heating allowed for optical characterization of the sample surface at select temperatures during the heating process where the surrounding air was stagnant. The same specimen was taken out from the furnace for observation then quickly placed back in the furnace to minimize fluctuations in the heating/cooling profile. The top surface of the specimen was exposed to the air while the bottom surface was in contact with a Ti foil placed inside the Al<sub>2</sub>O<sub>3</sub> crucible.

Fig. 4.11 showed the color evolution of the C12A7: $e^-$  specimen during the furnace heating. Visible white regions started to form on the bottom surface at 550°C. At 600°C, oxidation was indicated by white a mostly white bottom surface and the oxidation continued to 900 °C. The top surface started to show clear oxidation (white regions) at the edge at 400 °C while the majority of the sample remained a dark color. The color of one edge of the top surface became completely white at 700 °C, showing a diffusion front similar to what was observed in post-TG-tested sample (Fig. 4.9c). Except the edge, the majority of the top surface did not show visible change until 750 °C at which the color started to turn brown which spread throughout the surface. Subsequently, the top surface turned to the previously observed translucent status when temperature was increased to 900 °C. XRD analysis (Fig. 4.12) showed that the white color

corresponded to oxy-C12A7 containing some secondary calcium aluminate phases (CA and C3A) and the tan color corresponded to single phase oxy-C12A7.

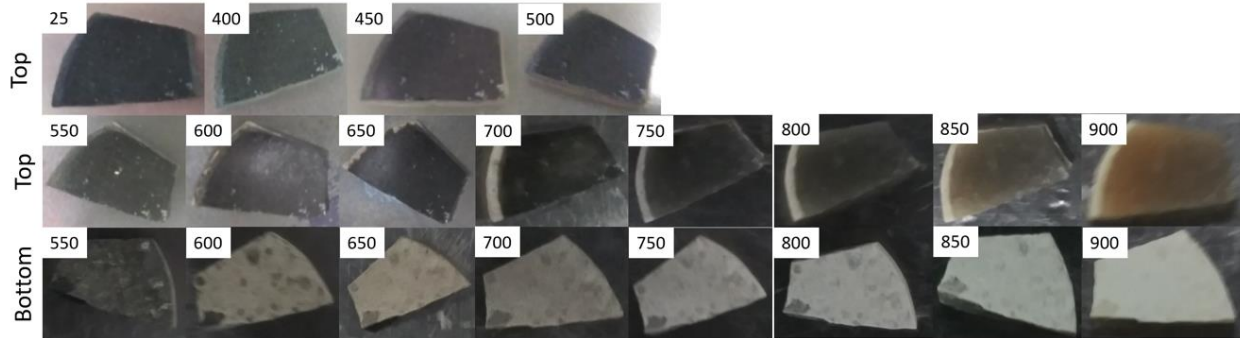


Fig. 4.11: Photos of the two surfaces of C12A7: $e^-$  at different temperatures showing the color evolution during heating in air in a furnace

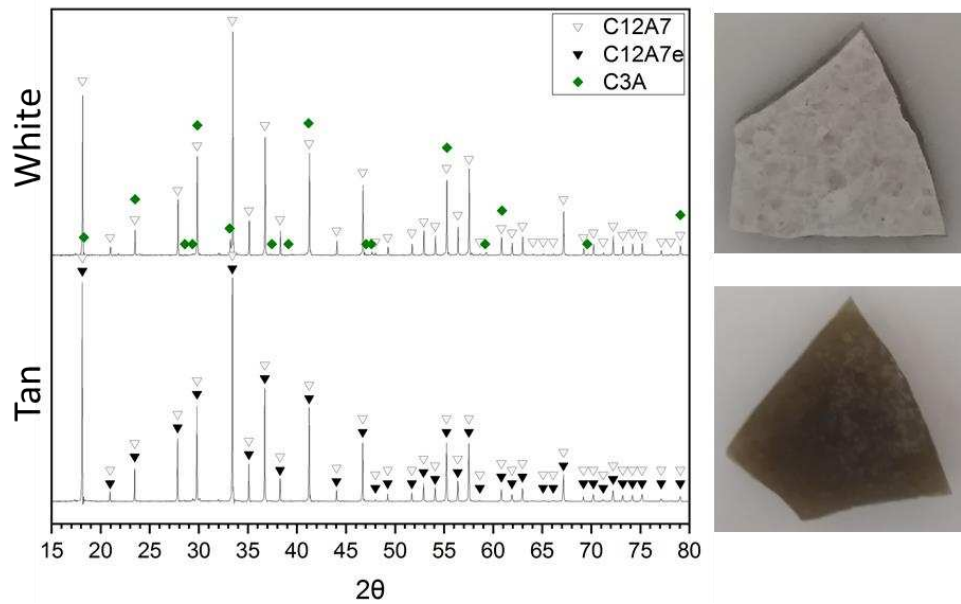


Figure 4.12: XRD pattern of the (a) white and (b) tan surfaces of C12A7

When the temperature was increased to 1000°C and above, the specimen surfaces maintained the two observed colors (Fig. 4.13a). After being held at 1350°C for 10 minutes, the specimens were quickly put under vacuum in a desiccator to avoid undesired reactions from air cooling such as oxygen or hydroxide adsorption that occurred between 500°C and 900°C. These

specimens completely crystallized into the translucent tan status shown in Fig 4.13b. This color change from white to tan suggested that the secondary calcium aluminate phases formed previously were mitigated or they reacted to reform almost pure oxy-C12A7 when the temperature increased from 1000°C to 1350°C.

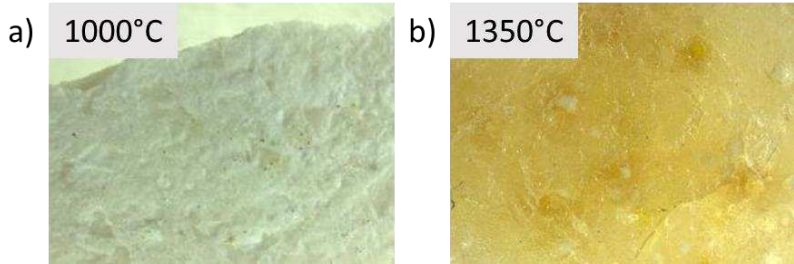


Figure 4.13: Optical images of the specimen bottom surface after being held at (a) 1000°C and (b) 1350°C

It was not completely clear yet why the bottom surface displayed formation of the white regions, oxy-C12A7 containing CA and/or C3A phases, while the majority of top surface (except one edge) only exhibited tan regions (pure oxy-C12A7 with little other calcium aluminate phases). However, it was correlated to the contact with another solid media (Ti foil or Al<sub>2</sub>O<sub>3</sub> crucible) at the bottom surface of the specimen, while the top surface was just exposed to air. This phenomenon of different colors on the two surfaces was also observed in the samples after thermogravimetric test as shown in Fig 4.10. It appeared that the formation of white color regions resulted from the contact with different solid media (Al<sub>2</sub>O<sub>3</sub>, platinum, carbon, and titanium). Any interdiffusion occurring at the solid/solid interface disrupted the stoichiometric 12:7 ratio of Ca to Al in the C12A7:e<sup>-</sup> or partially oxidized mayenite, finally leading to the formation of CA or C3A phases.

The S-type Cu-doped C12A7:e<sup>-</sup> samples also exhibited color change after the TG/DTA testing (Fig. 4.14). A representative specimen (cut from S3) without evidently visible Cu regions on the surface exhibited a solid white layer, representing oxy-C12A7 containing C3A phase, on the surface that contacted the Pt pan in the sample holder in TG equipment, and several black spots were present on this surface (Fig. 4.14a). The black spots corresponded to copper oxide CuO, the peaks for which was observed in XRD pattern of the post-TG sample. The rest of the post-TG specimen turned to the translucent tan color, representing oxy-C12A7 with minimal 2<sup>nd</sup> phases. Fig. 4.14b displayed the color change for a representative specimen that contained evident Cu regions on the surface. The surface containing the visible Cu regions, which was also the surface exposed to the air flow during testing, exhibited a small amount of white regions. In contrast, the other surface that was in contact with the Pt pan of the sample holder turned to a layer of solid white after the thermal exposure of TG test. The rest bulk of this specimen turned to the translucent tan color, i.e., oxy-C12A7 with minimal other calcium aluminate phases. The visible Cu regions in the pre-testing sample turned to became black regions due to the formation of CuO, which was confirmed by XRD analysis as shown in Fig. 4.15.

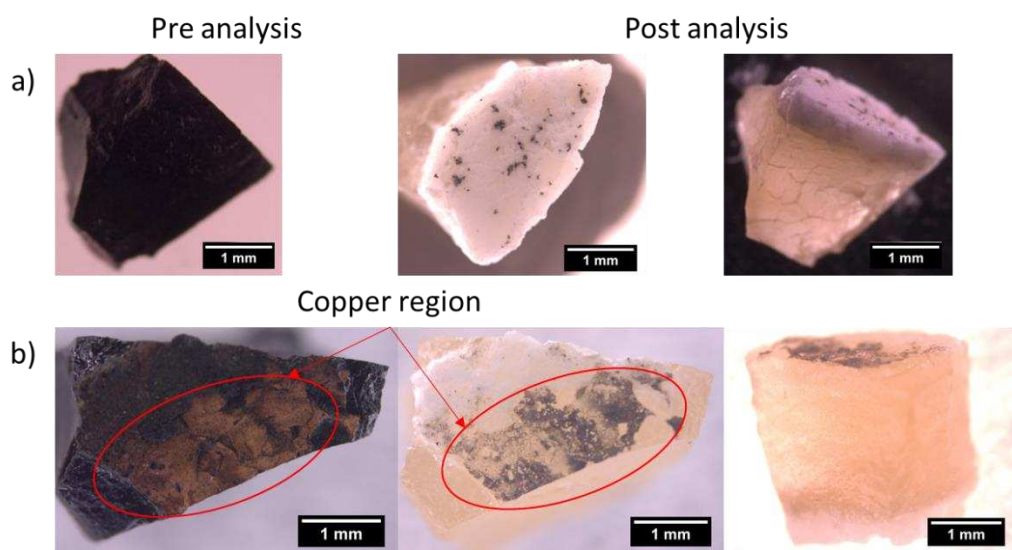


Figure 4.14: Pictures of specimens cut from S3 after TG test in air (a) a representative specimen without evident Cu-region on surface; and (b) a representative specimen with evident Cu-region on surface.

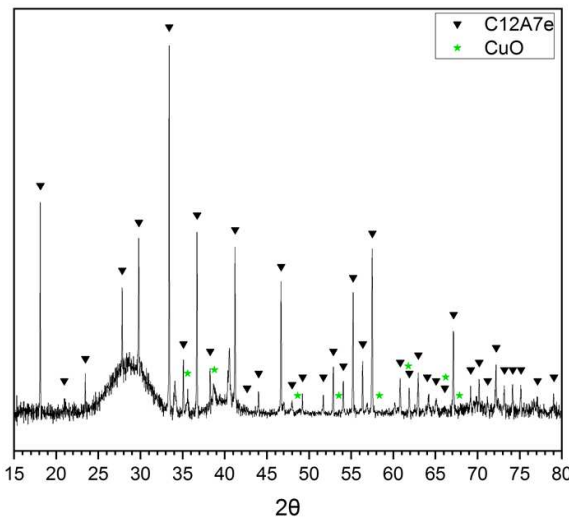


Figure 4.15: XRD pattern for S3 specimen post thermal analysis

A visible difference in the oxidation characteristics was also visibly observed. Fig 4.16 displays optical images of an S2 specimen incrementally heated in a furnace.

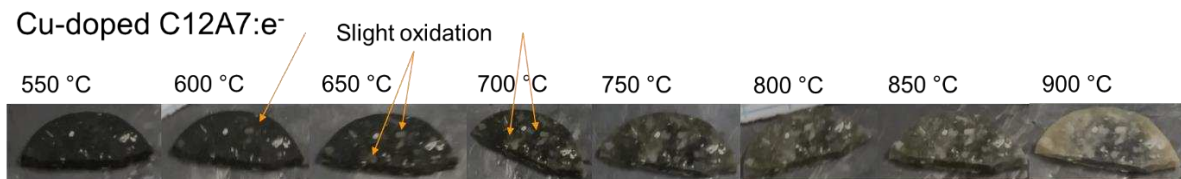


Figure 4.16: Optical images of thermally analyzed S2 specimen via furnace heating

The Cu-doped C12A7: $e^-$  showed slight oxidation from 600°C to 700°C. Significant changes were not visible on the Cu-doped C12A7: $e^-$  surface until temperature exceeded 750°C compared to undoped C12A7: $e^-$  which had complete white coloration of a similar surface at 600°C. The presence of a black phase in the Cu-doped specimen at 900°C suggested that the electride phase had not been fully oxidized. Hence, Cu-doping reduced the rate of oxidation.

#### 4.5 Efficiency of doping by SPS Diffusion

S-type samples were produced via SPS as a novel method for solid state diffusion to achieve doping. The distribution of Cu observed in SEM combined with EDS confirmed that Cu diffused into C12A7: $e^-$  despite the holding time in SPS was on the order of a few minutes in contrast to several hours for F-type samples. The reduction in lattice parameter and the improved oxidation resistance, as discussed in previous sections, suggested lattice diffusion was the dominant mechanism and Cu-doping was achieved during SPS diffusion. The flat interface between the Cu foil and the preformed C12A7: $e^-$  disk samples decreased the energy reduction that can be achieved by surface area reduction to a negligible level. High heating rates and the applied electrical field in SPS accelerated diffusion kinetics and promoted grain boundary and lattice diffusion shortly after the processing started. Diffusion doping achieved in this relatively short time (< 40 minutes) using this method can be attributed to factors previously mentioned in section 1.4. Thermal-activated diffusion and electromigration are two different concepts in SPS, but both assisted the diffusion mechanisms. Thermodiffusion would have the highest impact during the heating portion of S-type experiments due to large thermal gradients resulted from high heating rates<sup>54</sup>. When the electrical currents did not uniformly flow through the sample, the temperature distribution in the sample exhibited a gradient (shown in Fig. 4.16) The Cu foils underwent a higher temperature than the internal bulk C12A7: $e^-$  at any given time during the heating. When the sample was held at the select diffusion temperatures, the thermal difference between the Cu foils and the internal bulk C12A7: $e^-$  was reduced as with increasing holding time. Both Cu and C12A7: $e^-$  are electrically conductive though C12A7: $e^-$  has a significant lower conductivity than Cu and the graphite tooling. Some electrical current flew through the C12A7: $e^-$  sample during SPS, which would reduce the temperature gradient limiting thermodiffusion,

promoted electromigration. Electromigration was an active mechanism through entire SPS diffusion doping as the electrical current was applied during the whole process. Nominally, higher temperatures should lead to more diffusion, i.e., it was anticipated that S3 should achieve more significant diffusion and thus a higher Cu dopant concentration in the C12A7: $e^-$  lattice than S2. However, S2 exhibited a smaller lattice parameter and better improvement in thermal stability (oxidation resistance) than S3. It is imperative to determine the optimal dopant concentration for C12A7: $e^-$  to enhance its thermal stability and oxidation resistance, which is yet unknown and being explored.

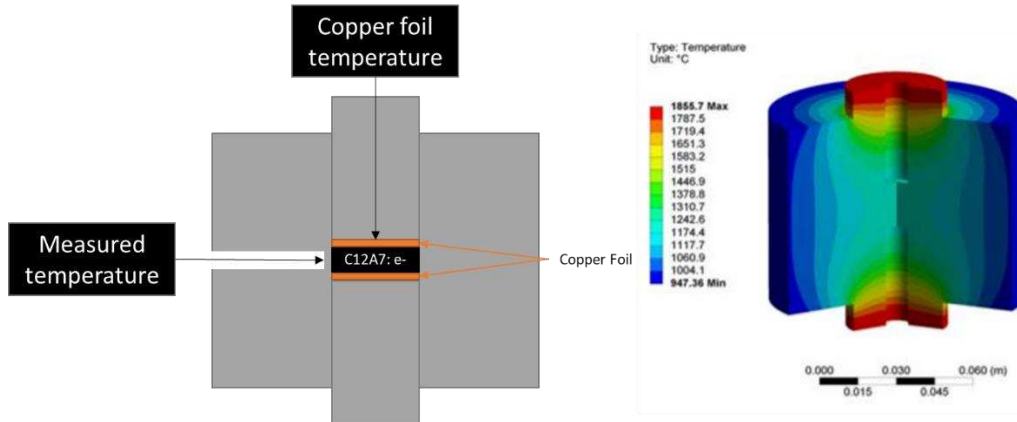


Figure 4.17: SPS measurement set-up and thermal gradient model<sup>54</sup>

The key finding to take away from this section was that novel SPS diffusion doping successfully resulted in a Cu-doped C12A7: $e^-$  surface layer, which subsequently improved the stability of C12A7: $e^-$ . Compared to traditional diffusion doping in a furnace, doping can be achieved more efficiently, i.e., shorter holding time, in SPS diffusion. The optimal temperature for copper doping into C12A7: $e^-$  via SPS diffusion was found to be 800 °C out of three select temperatures in this study.

#### 4.6 Cu Doping Summary

Cu-doped C<sub>12</sub>A<sub>7</sub>:e<sup>-</sup> synthesis was successfully achieved by both conventional furnace diffusion (F-type) and SPS diffusion (S-type). Secondary calcium aluminate phases like CA and C<sub>3</sub>A and a surface Cu layer were observed in F-type samples while S-type samples exhibited primarily C<sub>12</sub>A<sub>7</sub>:e<sup>-</sup> phase except that S3 displayed small amount of visible Cu regions on the surface. All doped samples showed a reduction in lattice parameter of C<sub>12</sub>A<sub>7</sub>:e<sup>-</sup> with S2 showing the largest decrease in lattice parameter (i.e., smallest lattice parameter). The distribution of Cu on the S2 sample surface was uniform in contrast to the presence of local Cu-rich regions observed in F-type samples. All S-type Cu-doped samples exhibited better oxidation resistance and thermal stability than the un-doped counterpart, represented by the higher onset and peak temperatures for oxidation, lower mass gain rates, and overall lower mass gain percentage. The mass gain during TG testing started with adsorption of oxygen on the specimen surface, which reacted with the extra-framework electrons to form oxide anions when the temperature was increased. The modification of sample surface by Cu-doping either retarded the oxygen adsorption or the reaction between the adsorbed oxygen and the anionic electrons in the C<sub>12</sub>A<sub>7</sub>:e<sup>-</sup> lattice, giving rise to the improved oxidation resistance and thermal stability to higher temperatures. S2 exhibited the best combination of electrical conductivity, oxidation resistance, and thermal stability, corresponding to the smallest lattice parameter and minimal presence of second phases. Diffusion doping via SPS was proved to be a much more efficient way to achieve effective Cu-doping. And the effect of Cu-doping on C<sub>12</sub>A<sub>7</sub>:e<sup>-</sup> was experimentally investigated, which showed that Cu-doping was an effective approach to improve the thermal stability of C<sub>12</sub>A<sub>7</sub>:e<sup>-</sup>.

## CHAPTER 5: NIOBIUM DOPING OF MAYENITE ELECTRIDE

This chapter discusses the results of Nb-doping of C<sub>12</sub>A<sub>7</sub>:e<sup>-</sup>. Phase and structural analyses revealed that Nb doping was successfully achieved via two methods: (1) the SPS of the preformed mixture of C<sub>12</sub>A<sub>7</sub> and Nb<sub>2</sub>O<sub>5</sub> and simultaneous reduction (C-type) and (2) the subsequent reduction of preformed Nb-C<sub>12</sub>A<sub>7</sub> produced from SSR (D-type). Thermal analysis results suggested Nb-doping successfully increased the oxidation resistance of C<sub>12</sub>A<sub>7</sub>:e<sup>-</sup> by increasing the onset temperature of the oxidation. However, catastrophic pest oxidation occurred during thermal analysis, which is attributed to the presence of metallic niobium phases.

### 5.1 Nb-C<sub>12</sub>A<sub>7</sub>:e<sup>-</sup> Phase and Microstructural Analysis

Uniform distribution of the niobium species is ideal for in-situ doping. It would allow for short diffusion lengths and ideally have a similar distribution to aluminum site vacancies in the C<sub>12</sub>A<sub>7</sub>:e<sup>-</sup> cage structure.

#### 5.1.1 Analysis of Plan A samples

Ball milling precursor materials successfully created a well distributed powder mixture to be used in SPS processing shown in Fig. 5.1. It was anticipated that uniform distribution of the Nb particles would allow for short diffusion lengths and promote the substitution of Al site vacancies by Nb in the C<sub>12</sub>A<sub>7</sub>:e<sup>-</sup> cage structure.

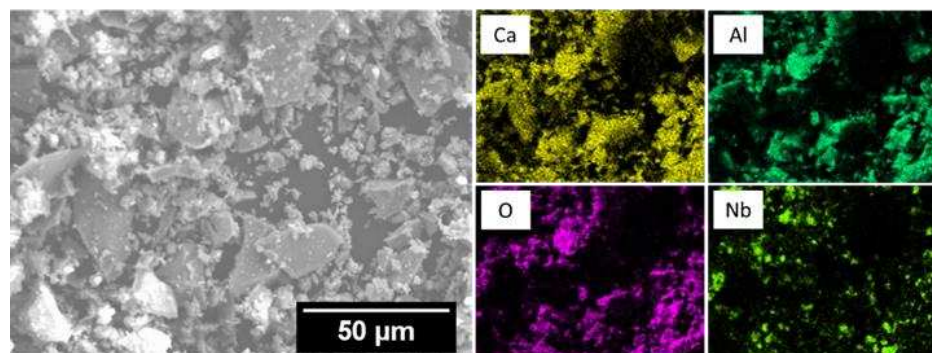


Figure 5.1: SEM and EDS images of the mixed C<sub>12</sub>A<sub>7</sub>:e<sup>-</sup> + Nb powder for Plan A

Fig 5.2 displays the XRD pattern, SEM images, and EDS maps of sample A1. The presence of Nb metal peaks (Fig 5.2b) and separated Nb particles (Fig 5.2c) suggest the combination of C12A7:e<sup>-</sup> with Nb metal for doping using SPS (A-type) resulted in a Nb – C12A7:e<sup>-</sup> composite. There was not a source that could oxidize Nb metal into a higher valence state, therefore little to no Nb-doping was achieved.

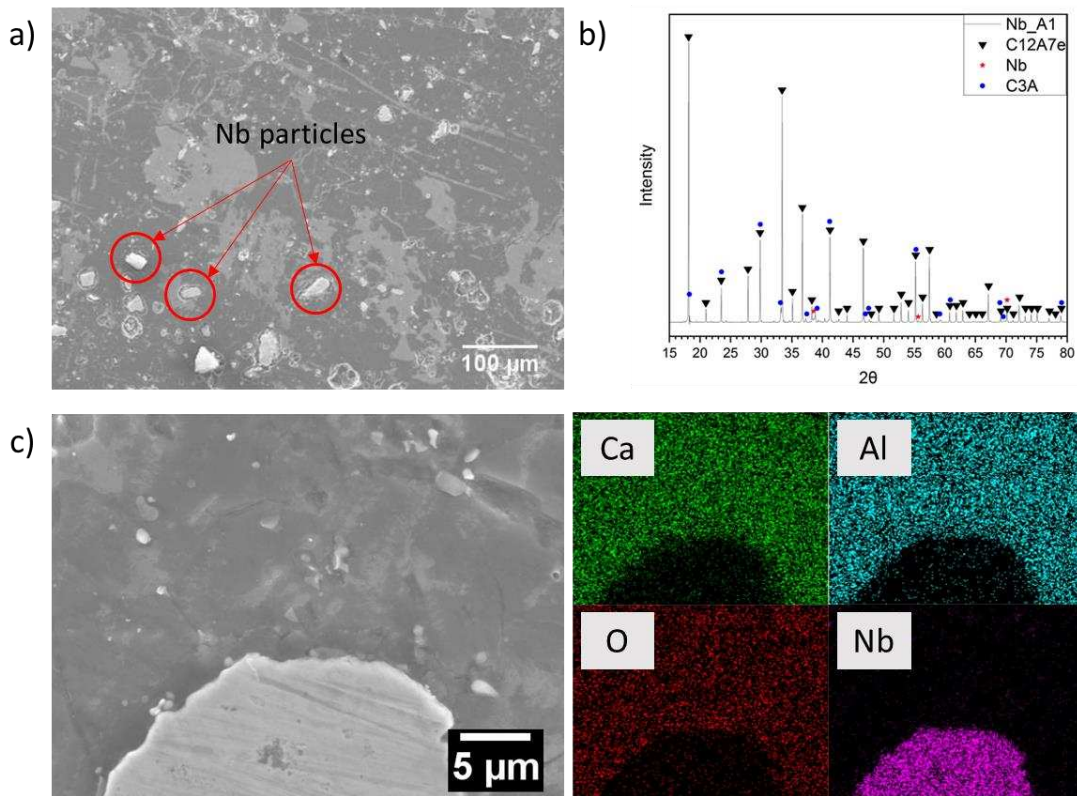
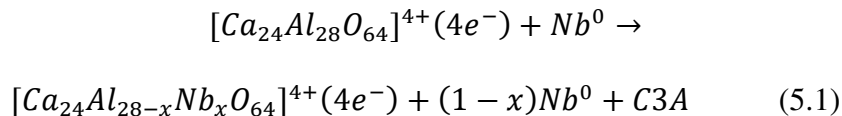


Figure 5.2: (a) SEM image of A1 surface, (b) XRD pattern of A1 surface, and (c) SEM image and EDS maps of Nb particle on the surface of A1

Reaction 5.1 represents the phase evolution undergone by the sample A1.



Nb metal particles would indicate  $x < 1$ . C<sub>3</sub>A formation has been shown to occur due to cationic doping of C<sub>12</sub>A<sub>7</sub><sup>15,38</sup>, which indicated some Nb-doping may have taken place ( $x > 0$ ). But the majority of the Nb was present as the metal phase.

#### 5.1.2 Analysis of Plan B samples

The ball milled C<sub>12</sub>A<sub>7</sub>:e<sup>-</sup> with Nb<sub>2</sub>O<sub>5</sub> powder (B-type) turned green (Fig 5.3c). It is important to note that green C<sub>12</sub>A<sub>7</sub>:e<sup>-</sup> indicates an electron density less than the maximum (<  $2.3 \times 10^{21} \text{ cm}^{-3}$ )<sup>66</sup>.

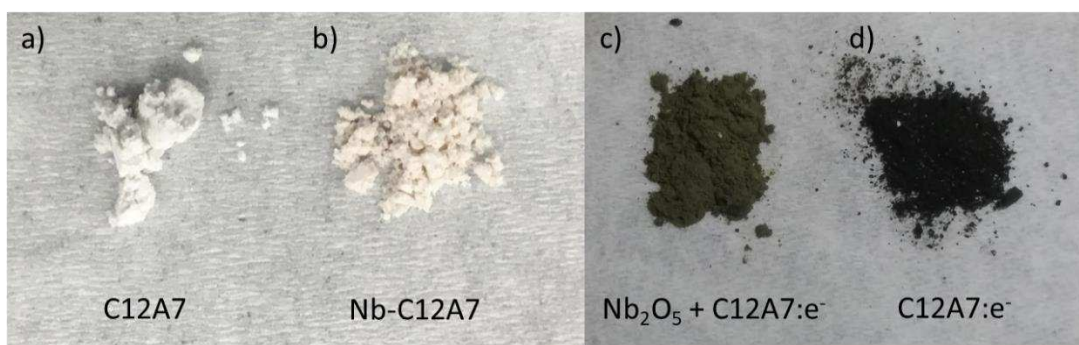


Figure 5.3: Powders of (a) C<sub>12</sub>A<sub>7</sub>, (b) preformed Nb-C<sub>12</sub>A<sub>7</sub>, (c) starting material for Plan B, and (d) C<sub>12</sub>A<sub>7</sub>:e<sup>-</sup>

Fig. 5.4 displays the optical image and XRD pattern of B1. Nb<sub>2</sub>O<sub>5</sub> reacted with C<sub>12</sub>A<sub>7</sub>:e<sup>-</sup> to form two Nb-containing oxide compounds(Ca<sub>4</sub>Nb<sub>2</sub>Al<sub>2</sub>O<sub>12</sub> and AlNbO<sub>4</sub>). Ca<sub>4</sub>Nb<sub>2</sub>Al<sub>2</sub>O<sub>12</sub> is a CaO:Nb<sub>2</sub>O<sub>5</sub>:Al<sub>2</sub>O<sub>3</sub> stoichiometric compound and is the only ternary compound that has been identified<sup>67</sup>. The blue coloration presented in Fig 5.4a is attributed to Ca<sub>4</sub>Nb<sub>2</sub>Al<sub>2</sub>O<sub>12</sub>.

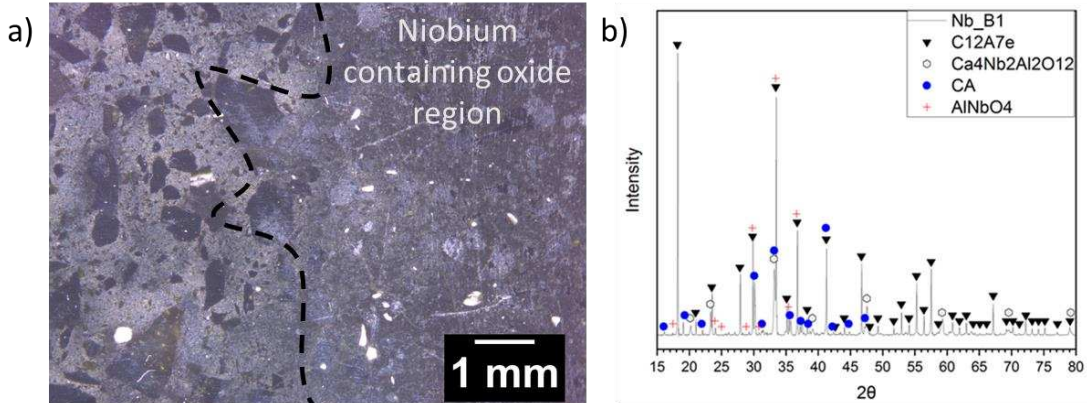
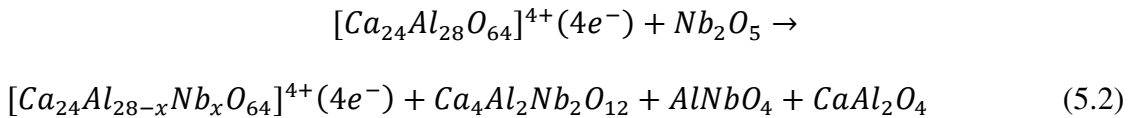


Figure 5.4: Sample B1 (a) optical image and (b) XRD pattern

Reaction 5.2 represents the phase evolution undergone by sample B1.



The presence of Nb-containing oxides suggests there are excess oxygen atoms introduced by  $Nb_2O_5$  without an efficient oxygen sink. Nb atoms are pentavalent in all Nb-containing compounds formed in Plan B samples, which indicated Nb-doping can occur.

### 5.1.3 Analysis of Plan C samples

The use of C12A7 with  $Nb_2O_5$  precursor powder as the starting material in Plan C, followed by concurrent reduction and doping in SPS, resulted in a partially reduced sample. Fig 5.5 displays optical imaging and the XRD pattern for sample C1. Peaks for metal Nb were identified in the diffraction pattern (Fig 5.5b). Secondary calcium aluminate phase peaks suggest C3A and CA also formed during SPS.

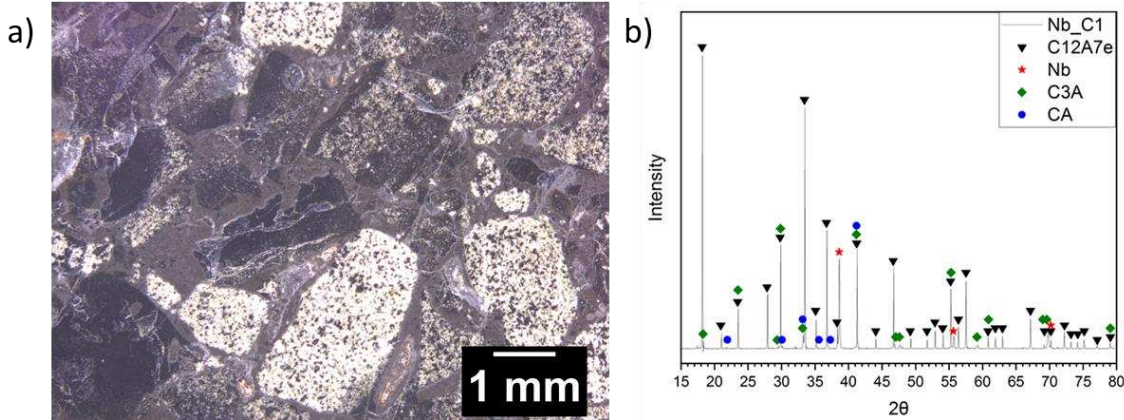
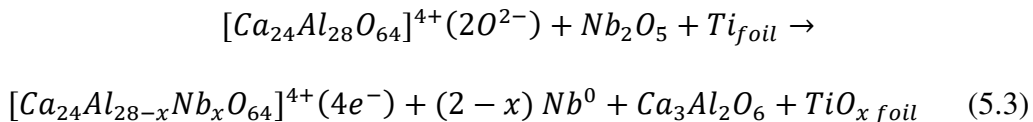


Figure 5.5: Sample C1 (a) optical image and (b) XRD pattern

Reaction 5.3 demonstrates the phase evolution undergone by C1.



The white and green regions observed throughout the sample suggest that conversion of  $Nb_2O_5$  into Nb metal, partial reduction of C12A7, and potentially Nb-C12A7: $e^-$  (or Nb-C12A7) occurred during the SPS. As mentioned in section 5.1.1, C3A formation has been shown in other M-C12A7 samples. The potential of Nb-doping was supported by that some Nb atoms existed in a pentavalent state by XPS, which is to be discussed in section 5.2. Fig 5.6 displays the microstructure of C2. Nb-rich region and several separate Nb-deficient regions were observed.

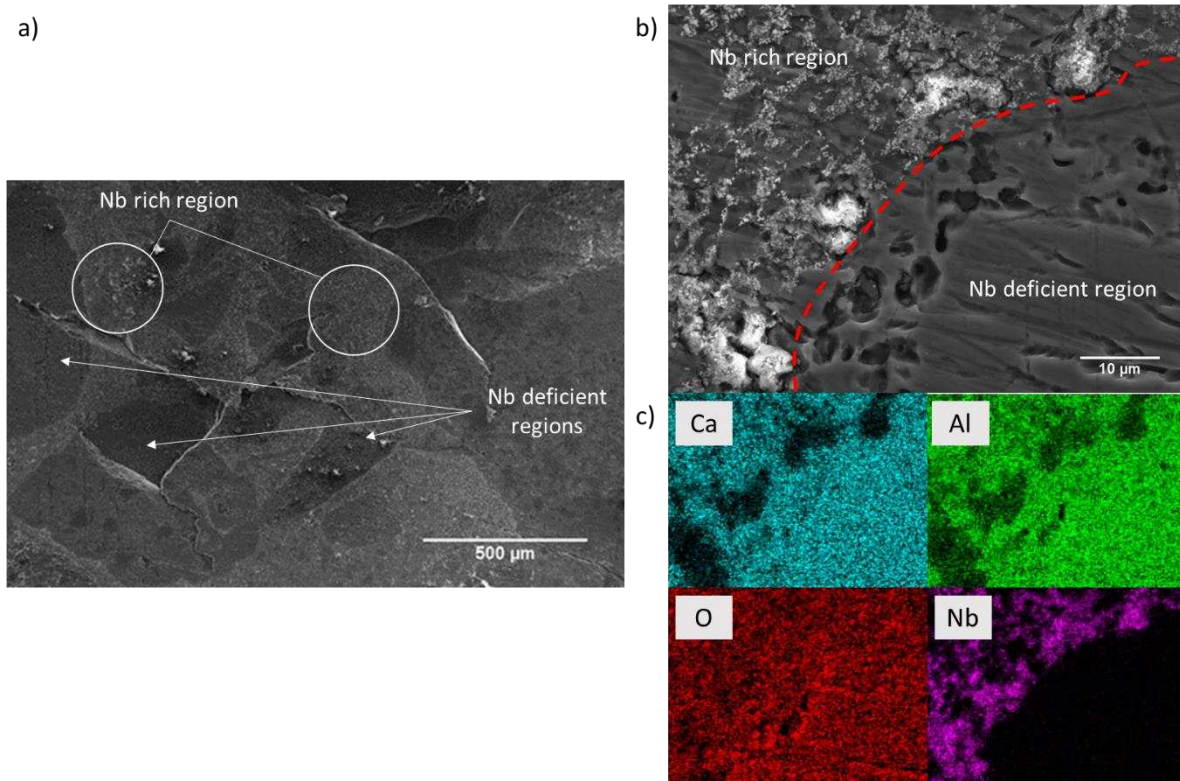


Figure 5.6: Microstructure of Sample C2. (a) SEM image of the sample surface and (b) SEM image showing a clear boundary between Nb-rich and Nb-deficient regions with (c) EDS maps

The Plan C method was modified to achieve better reduction of C12A7 to C12A7: $e^-$ . The first modification was reduction of initial powder particle size by grinding the powder mixture with a mortar and pestle. Smaller particle size creates greater homogeneity in the precursor mixture to mitigate Nb-rich areas previously observed. Fig 5.7 displays an optical image and XRD pattern for sample C4. This sample presents a blue surface with a scattered black phase Fig 5.7a). Peaks for  $\text{Ca}_4\text{Nb}_2\text{Al}_2\text{O}_{12}$  and  $\text{AlNbO}_4$  were identified in the XRD pattern. This was observed in B1 as well, which also showed some blue regions, indicating one or both of the  $\text{Ca}_4\text{Nb}_2\text{Al}_2\text{O}_{12}$  and  $\text{AlNbO}_4$  phases caused the color change.

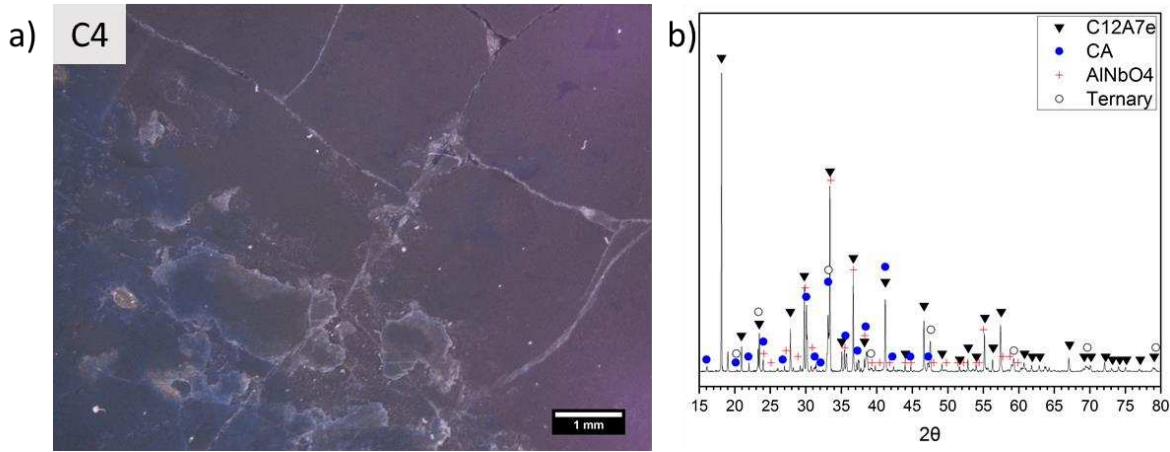
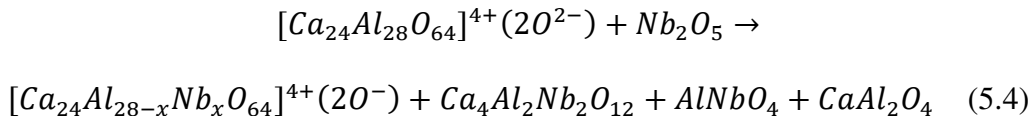


Figure 5.7: Sample C4 (a) optical image and (b) XRD pattern

Reaction 5.4 represents the phase evolution undergone by sample C4.



Color change can occur due to a metal-oxide surface layer on metals<sup>68, 69</sup>. Blue coloration of the surface and unreduced bulk suggested a Nb-oxide formed a surface layer and inhibited oxygen diffusion which slowed or prohibited further reduction of the C12A7 to its electride phase in C4. Based on the results observed in C2 and C4, the holding temperature in SPS was increased from 1300 °C to 1350 °C, close to the stability of Ca-Nb-O phases (1375 °C)<sup>67</sup>. Increasing the temperature of SPS resulted in near completely reduced Nb-C12A7: $e^-$  with no Nb-containing oxide formation, demonstrated by the formation of a grey bulk with dark particles (Fig 5.8a), and the XRD pattern (Fig 5.8b). In addition, the electrical conductivity of C5 is significantly increased compared to C1 to be discussed in Section 5.3, also supported that better reduction was achieved in C5.

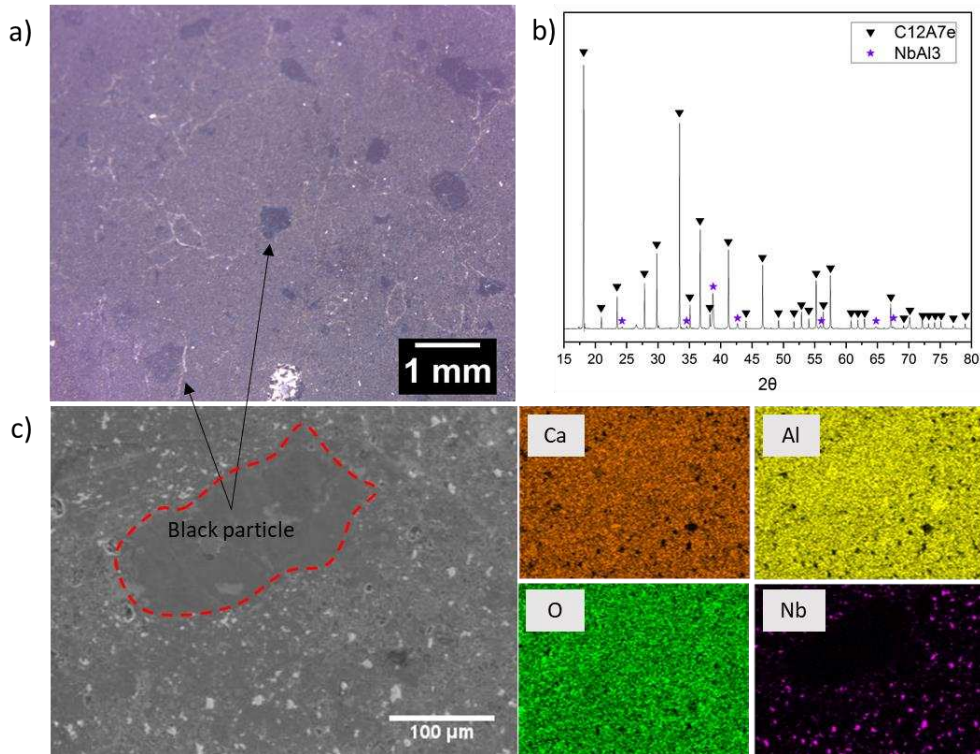


Figure 5.8: Sample C5 (a) optical image, (b) XRD pattern, and (c) SEM image with EDS maps of a dark particle on the surface

#### 5.1.4 Analysis of Plan D samples

Plan D was performed by two-step processing, solid state reaction followed by reduction in SPS. Fig 5.9 displays XRD patterns of Nb-C12A7 powders produced from  $\text{CaCO}_3$ ,  $\text{Al}_2\text{O}_3$ , and  $\text{Nb}_2\text{O}_5$  mixture by SSR in open air in a high temperature furnace (D-type step 1). The high relative peak intensity of CA and C3A in Nb-C12A7 (Fig 5.9a) indicated insufficient processing for single phase formation. Therefore, the hold temperature was increased from 1300 °C to 1350 °C and the hold time was extended from 10 hours to 12 hours in SSR to mitigate CA and C3A phases. Resulting Nb-C12A7 exhibited predominant C12A7 with much less C3A phase (Fig. 5.9b).

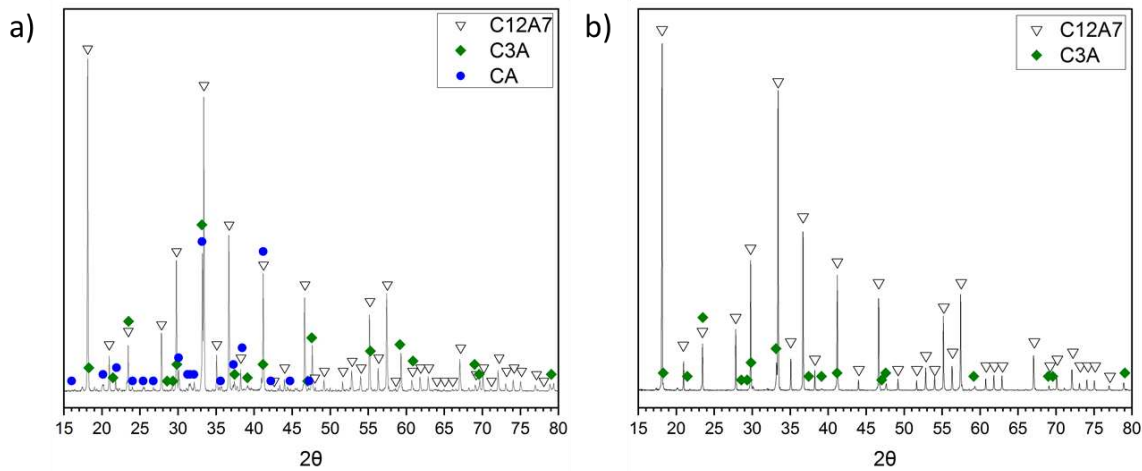


Figure 5.9: XRD patterns of Nb-C12A7 powders produced by SSR at (a)  $1300\text{ }^{\circ}\text{C}$ , 10 h and (b)  $1350\text{ }^{\circ}\text{C}$ , 12 h

Fig 5.10 displays an optical image, SEM image with EDS maps, and the XRD pattern of sample D1. D1 was made by using the Nb-C12A7 powders produced by SSR at  $1300\text{ }^{\circ}\text{C}$ . Nb metal formed during reduction of Nb-C12A7 (D-type step 2), evidenced by the XRD peaks (Fig 5.10b). Nb-rich particles were homogenously distributed across the sample surface (Fig 5.10c).

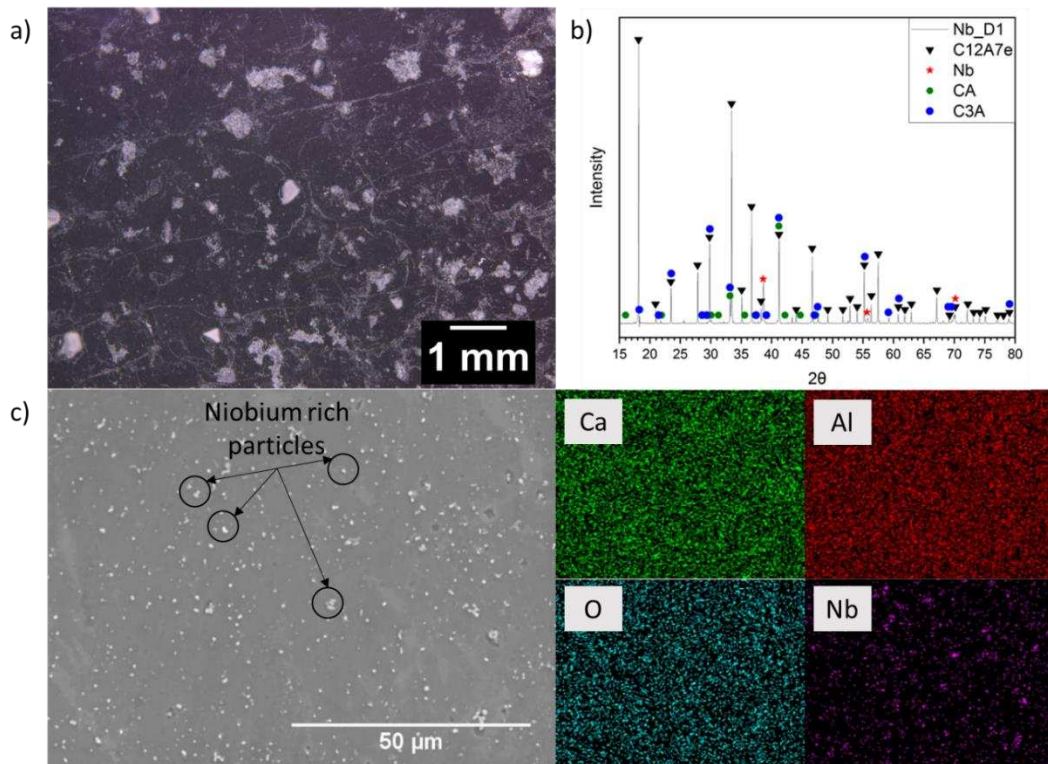
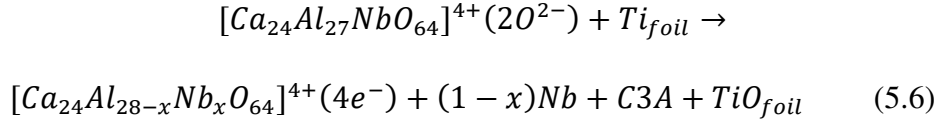
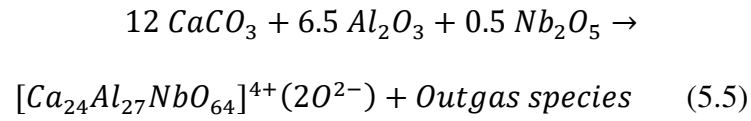


Figure 5.10: Sample D1 (a) optical image of the surface, (b) XRD pattern, and (c) SEM image with EDS maps of the surface

The phase evolution during D-type process are presented as (5.5) and (5.6) for step 1 and step 2, respectively.



The formation of Nb metal in reaction (5.6) is similar to the formation of metal Ga and C3A during reduction of Ga-doped C12A7 that was produced by SSR in a previous study<sup>38</sup>. The white regions observed in Fig 5.10a indicated D1 was not fully reduced.

D4 was made using the Nb-doped C12A7 powders produced by SSR at 1350 °C.

Mitigation of large white regions (Fig 5.11a) and increased electrical conductivity compared to D1, to be discussed in Section 5.3, suggested greater reduction was achieved. Peaks corresponding to metal Nb and C3A in sample D4 (Fig 5.11b) indicated separation of Nb from the C12A7 framework.

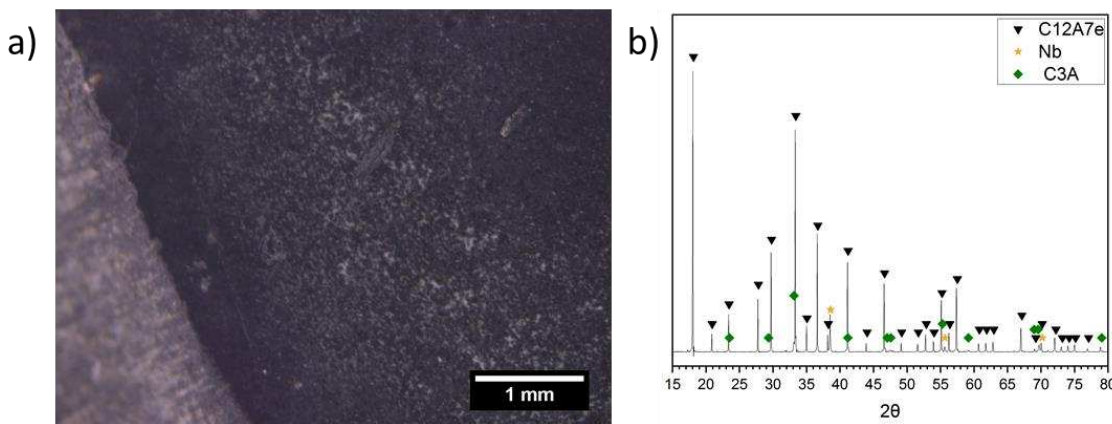


Figure 5.11: Sample D4 (a) optical image and (b) XRD scan

### 5.1.5 Analysis of Plan E samples

Plan E samples encountered melting issue during the processing and formed amorphous glassy materials, as shown in Fig. 5.12. Reduction of the processing temperature resulted in little to no changes compared to undoped C12A7: $e^-$ .

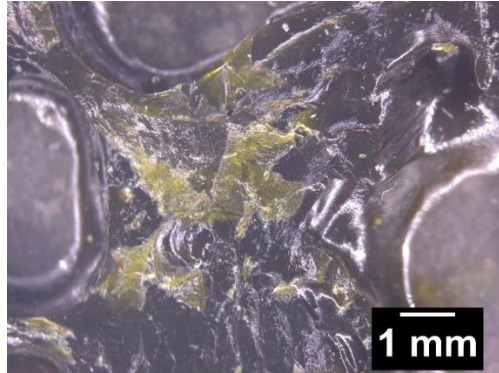


Figure 5.12: Resolidified C12A7: $e^-$  on Nb metal cap

In contrast to efficient Cu-doping of C12A7: $e^-$  via SPS diffusion doping discussed in Section 4.5 in Chapter 4, Nb-C12A7: $e^-$  was not successfully synthesized via diffusion doping of Nb using SPS with Nb metal caps. The absolute processing temperature for Nb doping was higher compared to Cu doping. However, the homologous temperatures ( $T_H$ ) used in Cu-doping (0.717, 0.79, and 0.864), given by equation 5.7, could not be achieved for Nb doping.

$$T_H = \frac{T(K)}{T_m(K)} \quad (5.7)$$

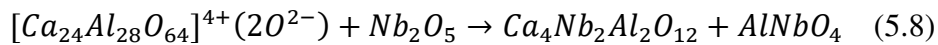
where  $T(K)$  is absolute processing temperature and  $T_m(K)$  is absolute melting temperature of the material.

Cu diffusion doping using SPS was found to be most effective at  $T_H = 0.79$ . The maximum  $T_H$  that could be achieved for Nb diffusion doping below the melting temperature of

C12A7: $e^-$  (1415 °C) was 0.61. The Nb diffusion doping attempted at 1350 °C resulted in a C12A7: $e^-$  melt in the die. Due to local overheating and the inability to directly measure absolute temperature of a sample in SPS, a temperature above 1415 °C at certain locations caused melting. Processing temperature was decreased to  $T_H = 0.54$ , which resulted in no significant changes to the phases or thermal resistance compared to undoped C12A7: $e^-$ . Electrical conductivity of E2 (0.0063 S/cm) was orders of magnitude lower than that of undoped C12A7: $e^-$ . Hence, Nb diffusion doping using SPS (Plan E) was not pursued further. The lack of doping effects at  $T_H$  lower than 0.6 indicated the diffusivity of Nb cations is too low for sufficient doping during the short (< 45 minutes) processing time even with the accelerated diffusion provided by the applied electrical field in SPS.

#### 5.1.6 Niobium-doping Process Summary

Plan A, B, and E processes were determined to be not suitable for synthesis of Nb-C12A7: $e^-$ . Plan A process lacked a driving force to oxidize Nb<sup>0</sup> to Nb cations, and it caused the formation of a composite rather than Nb-doping. Plan B process lacked an oxygen sink for the Nb<sub>2</sub>O<sub>5</sub> in the precursor, leading to the formation of Ca<sub>4</sub>Nb<sub>2</sub>Al<sub>2</sub>O<sub>12</sub> and AlNbO<sub>4</sub>. The ternary oxide compound Ca<sub>4</sub>Nb<sub>2</sub>Al<sub>2</sub>O<sub>12</sub> led to the blue coloration observed in B1 and C4, which suggested a side reaction between C12A7 or C12A7: $e^-$  and Nb<sub>2</sub>O<sub>5</sub> given in Reaction 5.8.



The XRD patterns for B2, C1, or C5 did not exhibit prominent peaks for the Ca<sub>4</sub>Nb<sub>2</sub>Al<sub>2</sub>O<sub>12</sub> phase. Increased processing temperature to 1350°C in Plan C and Plan D resulted in near fully reduced Nb-C12A7: $e^-$  samples, C5 and D4. The NbAl<sub>3</sub> in C5 and Nb metal in D4 demonstrated reduction of Nb atoms from Nb<sub>2</sub>O<sub>5</sub> in C5 or Nb-C12A7 from D4 to a lower valence status. Although Sample D4 contained C3A that has been shown to form concomitantly with the dopant

metal phase during reduction of cationic doped C12A7<sup>38</sup>, Plan C and Plan D processes were identified to be potential approaches to achieve Nb-doping of C12A7: $e^-$ . The C-type and D-type samples were investigated further to verify if Nb doping was successful.

## 5.2 Niobium Speciation in Nb-C12A7: $e^-$

X-ray photoelectron spectroscopy (XPS) was utilized to determine the bonding environments of atoms in Nb-C12A7: $e^-$  samples. Fig 5.13 displays the XPS spectra of C2. The binding energy (BE) for Nb 3d<sub>5/2</sub> electron (206.91 eV) indicates some Nb atoms are pentavalent with Nb-O-Ca bonding. The BE for Nb electrons identified by XPS (Fig 5.13e) indicated a similar binding environment to that of CaNb<sub>2</sub>O<sub>6</sub> or Ca<sub>2</sub>Nb<sub>2</sub>O<sub>7</sub> (Fig 5.13f), suggesting C2 contains Nb-O-Ca bonding. The bonding environment of Nb atoms and lack of diffraction peaks for Nb-containing oxides suggested Nb-doping of C12A7: $e^-$  was achieved in C2. The fully reduced C-type sample, C5, exhibited the Nb-doping of C12A7: $e^-$  as well.

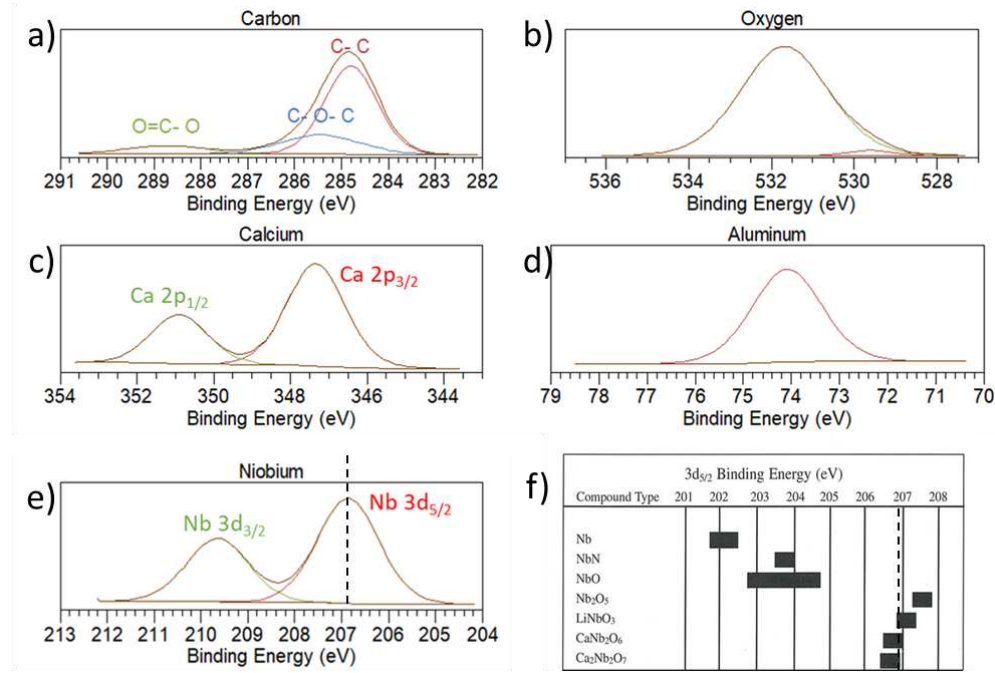


Figure 5.13: XPS spectrum of (a) C, (b) O, (c) Ca, (d) Al, and (e) Nb in sample C2 including (f) standard BE for Nb 3d<sub>5/2</sub> electrons. Note that the black dotted lines in (e) and (f) correspond to Nb 3d<sub>5/2</sub> peak BE

Atomic percentages of Ca, Al, and Nb were obtained at points surrounding the Nb-rich regions using EDS. Standard Ca/Al and Ca/Nb atomic ratios for unit cells with 0, 1, or 2 Nb atoms are given in Table 5.1. Fig 5.14 displays the SEM of a Nb-rich particle in sample C5 with EDS spectra scan points. It is important to note that EDS is a semi-quantitative analysis method. Ca/Al and Ca/Nb atomic ratios at positions 1, 2, and 6 (Table 5.2) indicated Nb-C12A7:e<sup>-</sup> with an average concentration near  $x = 1$  or  $x = 2$ . The Ca/Nb ratio at positions 1 and 2 suggest an average concentration of two Nb atoms per unit cell and the Ca/Nb ratio for position 6 suggests one Nb atom per unit cell.

Table 5.1: Standard Ca/Al and Ca/Nb atomic ratios for undoped and doped C12A7:e<sup>-</sup>

Nb atoms	0	1	2
Ca/Al ratio	0.857	0.889	0.923
Ca/Nb ratio	-	24	12

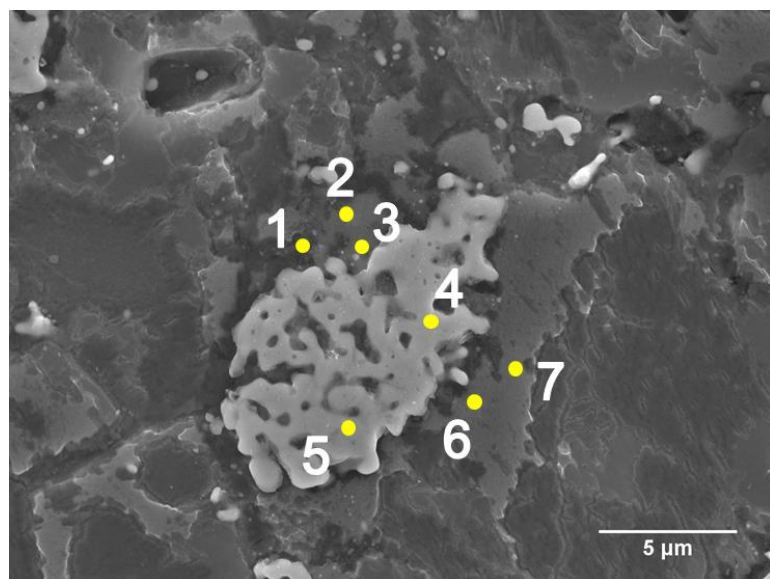


Figure 5.14: SEM image of an Nb-rich particle on the C5 surface with yellow dots representing EDS scan points

Table 5.2: Ca/Al and Ca/Nb atomic ratios of points in Fig 5.14

Position	1	2	3	4	5	6	7
Ca/Al ratio	0.886	0.787	0.718	0.333	0.348	0.837	0.869
Ca/Nb ratio	12.933	9.118	0.529	0.03	0.033	21.25	n/a

### 5.3 Electrical Conductivity

The electrical conductivity of select Nb-C12A7: $e^-$  samples were determined using the same method described in Section 4.3 in Chapter 4 for the Cu-doping. Table 5.3 provides the electrical conductivities calculated from two-probe and four-probe resistivity measurements for undoped, C-type, and D-type samples. The higher conductivity achieved by D1 and D4 than those of C1 and C5 suggested D-type processing was the most effective Nb doping method.

Table 5.3: Electrical conductivities of C12A7: $e^-$  and Nb-C12A7: $e^-$  at room-temperature

SAMPLE	TWO-PROBE CONDUCTIVITY [S/cm]	FOUR-PROBE CONDUCTIVITY [S/cm]
C12A7: $e^-$	0.106	103.7
C1	0.0887	0.1
C5	0.0295	6.9
D1	0.182	17.7
D4	0.0545	63.2

Electrical conductivity obtained from the four-probe method revealed an increasing trend from C1 to C5 and from D1 to D4. The increases in electrical conductivity suggested greater reduction was achieved by increased processing temperature. Nb-doping did not increase electrical conductivity, which is contrary to what has been reported for other high valence cation-doped C12A7: $e^-$ , but is consistent with H $^-$  anion substituted Mg-C12A7<sup>70</sup>. Sample D4 exhibited a comparable electrical conductivity to undoped C12A7: $e^-$ . The primary goal was to improve the thermal stability and oxidation resistance of C12A7: $e^-$ , which is the focus of the next section.

## 5.4 Thermal Stability

Samples from Plan A, B, C, and D (A1, B2, C2, and D1) were tested in thermogravimetric and differential thermal analysis (TG/DTA) up to 550°C and 600°C to compare with the undoped C12A7: $e^-$  discussed in Section 4.4 in Chapter 4. Nb- doped C12A7: $e^-$  disintegrated into white powder when heated to 1050°C. Specimen from C5 and D4 were sequentially heated in a furnace and analyzed in the same method as C12A7: $e^-$  in section 4.4.

In general, Nb- doped C12A7: $e^-$  specimens displayed three regions with distinct characteristics in thermal analysis results. Region I exhibited mass gain less than 0.1% with low rates of mass gain. A sudden increase in the rate of mass gain transitioned into region II that exhibited rapid mass gain. A sudden decrease in the rate of mass gain transitioned into region III that exhibited a low rate of mass gain similar to region I. In region III mass gain stabilized at a maximum mass gain percentage in contrast to undoped C12A7: $e^-$  and Cu-doped C12A7: $e^-$ . It is important to note all mass gain has been attributed to oxidation from oxygen uptake by specimens from the surrounding environment. Analysis of specific samples are provided below.

Fig 5.15 presents the TG and DTA curves of A1 and B2. A1 specimen experienced three mass gain rate fluctuations which indicated three oxidation events. In comparison, undoped C12A7: $e^-$  exhibited two mass gain rate fluctuations attributed to oxygen reacting with extra-framework electrons to form oxide anions ( $O^{2-}$ ) that occupy cages and superoxide anion ( $O^-$  and  $O_2^-$ ) equilibrium<sup>51</sup>. The third mass gain event in A1 is attributed to Nb oxidation, further evidenced by a final percent mass gain (3.784%) above the theoretical percent mass gain (1.16%) for undoped C12A7: $e^-$  with maximum electron density. DTA peaks accompanied each mass gain event. It was observed that DTA peak intensity correlated with the rate of mass gain which supported the assumption that all events resulted from oxygen molecules to oxide anion

conversion. B2 exhibits two mass gain events compared to A1. The third mass gain event, greater percent of final mass gain, and presence of Nb metal in A1 suggested Nb oxidation occurs. The oxidation of Nb is further evidenced by the lack of a third exothermic peak and lower percent of final mass gain (0.827%) for B2 which did not contain Nb metal.

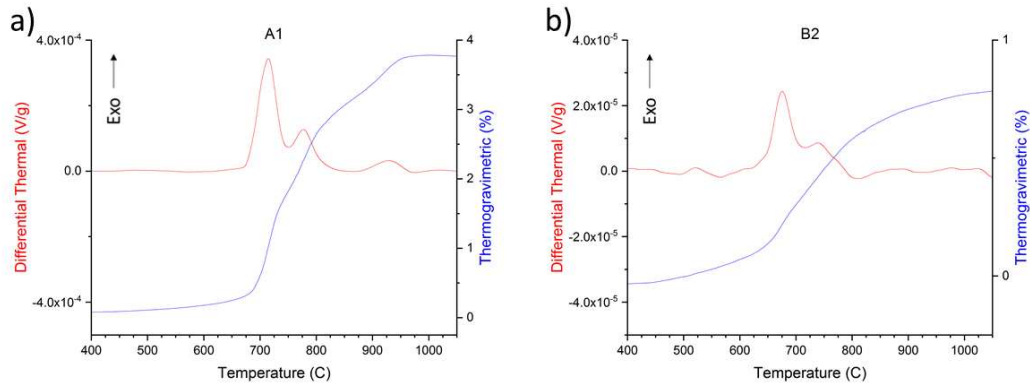


Figure 5.15: TG and DT curves of (a) A1 and (b) B2

Fig 5.16 presents mass gain percentage and normalized differential thermal curves for C2, C5, D1, and D4. The higher mass gain percentage of C5 (4.214%) compared to C2 (1.459%) and that of D4 (3.133%) compared to D1 (2.238%) indicated a greater concentration of Nb atoms in a metal phase or greater reduction of C12A7 to the electride phase in SPS or a combination of both. The lower mass gain percentage of D4 compared to C5 indicated a lower Nb metal phase concentration which suggested Nb did not completely separate from the C12A7: $e^-$  framework, leaving some Nb atoms present as dopants. It is important to note that the nominal concentration of Nb is the same for all Nb-C12A7: $e^-$  samples. It should also be noted that the electride phase in C5 and D4 is assumed to have achieved full reduction. C-type and D-type specimens experienced a greater rate of mass gain in region II compared to undoped C12A7: $e^-$  indicated by higher percentages of mass gained in shorter temperature ranges. Three exothermic peaks

observed in DT data for C5 were consistent with results from A1 which confirmed three oxygen conversion events occur in Nb-C12A7: $e^-$  specimen. The first exothermic peak was distinguished as the onset point for rapid oxidation. The onset temperature of oxidation peaks for Nb-C12A7: $e^-$  specimens were all above 650°C with the highest temperature onset points achieved by C5 (745°C) and D4 (770°C). Oxidation onset at higher temperatures compared to undoped C12A7: $e^-$  represent the improvement of oxidation resistance.

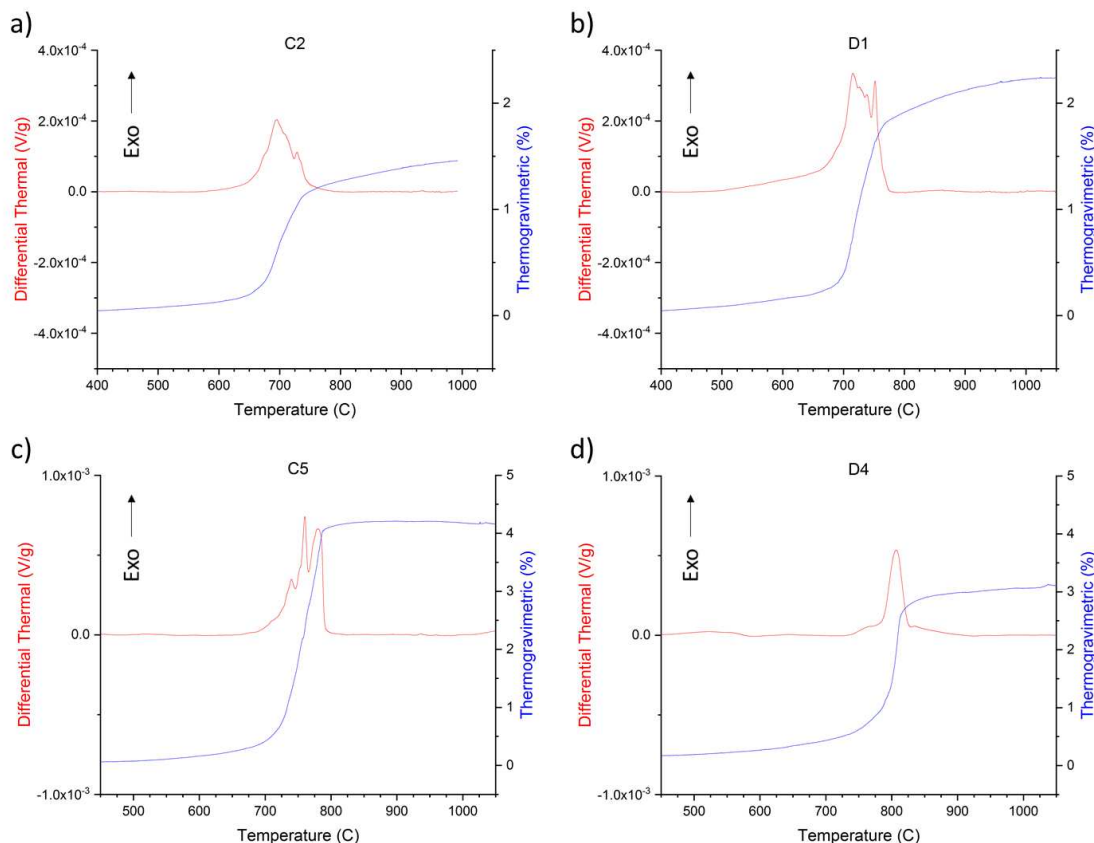


Figure 5.16: TG and DTA curves of (a) C2, (b) D1, (c) C5, and (d) D4

The Nb-doped C12A7: $e^-$  specimens disintegrated into white powder substances during thermal testing. White coloration indicated full oxidation of the specimen. Disintegration of intermetallic compounds in an oxidizing environment is known as ‘pest’ oxidation or ‘pesting’<sup>71</sup>.

The expansion coefficient of a unit cell from Nb metal to  $\text{Nb}_2\text{O}_5$ , also known as a Pilling-Bedworth ratio, is 2.68 which suggests high stress rates due to rapid expansion of dispersed Nb metal particles caused specimens to break apart into powder. Oxidation behavior of initially synthesized Nb-C12A7: $e^-$  samples was investigated between the onset oxidation temperatures for undoped C12A7: $e^-$  ( $575^\circ\text{C}$ ) and Nb-C12A7: $e^-$  ( $650^\circ\text{C}$ ).

Samples A1, B2, and D1 were analyzed in TG/DTA up to  $600^\circ\text{C}$  and  $650^\circ\text{C}$ . Fig 5.17 presents the percentages of mass gained by Nb-C12A7: $e^-$  and undoped C12A7: $e^-$  specimens. Fig 5.18 displays surface images of A1, B2, and D1 before and after TG/DTA. Nb-C12A7: $e^-$  specimen displayed minimal surface oxidation at  $600^\circ\text{C}$  with percentages of mass gain below 0.1%. Pest oxidation in B2 at  $650^\circ\text{C}$  was evidenced by white powder formation leaving craters (Fig 5.18b). An increasing mass gain rate suggested B2 underwent an onset of rapid mass gain. This was the lowest observed transition temperature for Nb-C12A7: $e^-$ . No significant change in the rate of mass gain for A1 and D1 confirmed the onset of rapid mass gain is above  $650^\circ\text{C}$  for those specimens. The onset temperature for rapid mass gain for undoped C12A7: $e^-$  is  $550^\circ\text{C}$  meaning Nb-doped C12A7: $e^-$  demonstrated an increased resistance to the onset of oxidation. At  $650^\circ\text{C}$ , A1, B2, and D1 gained 0.177%, 0.176%, and 0.160% of mass, respectively, suggesting that the oxidation resistance at intermediate temperatures ( $400^\circ\text{C}$  to  $700^\circ\text{C}$ ) was increased compared to undoped C12A7: $e^-$  that gained 0.498% percent mass.

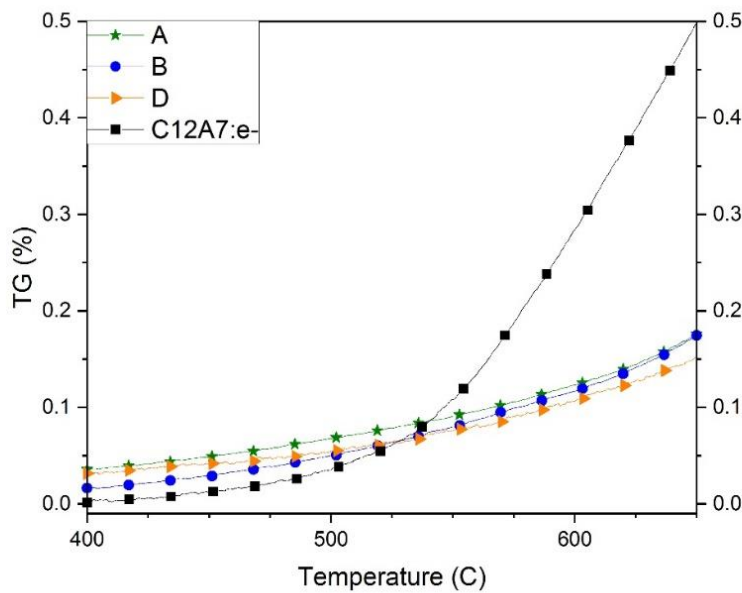


Figure 5.17: Thermogravimetric curves for Nb-C12A7: $e^-$  specimens and undoped C12A7: $e^-$  from 400°C to 650°C

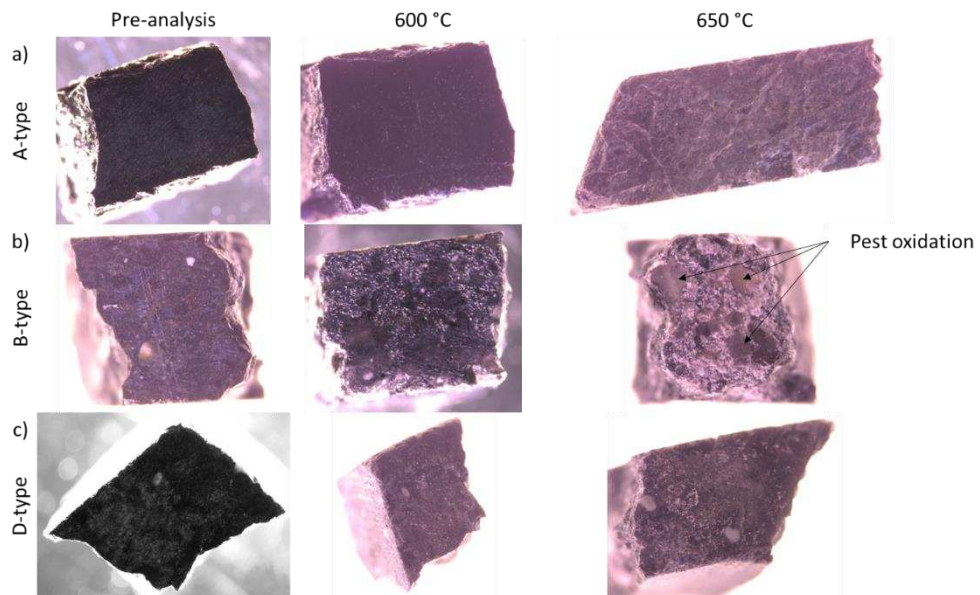


Figure 5.18: Microscope images of (a) A-type specimens, (b) B-type specimens, and (c) D-type specimens before thermal analysis and when held to 600°C or 650°C

To observe oxidation behavior in Nb-doped C12A7: $e^-$ , specimens of C5 and D4 were further studied by conducting thermal holds in a furnace at temperatures ranging from 400°C to 900°C

in 50°C increments. Specimens were held at each temperature for 5 minutes. Fig 5.19 displays images of C5 after being held at different temperatures. The breaking of C5 specimen at 750°C with no visible surface oxidation up to 700 °C indicated oxidation was initiated in the range of 700-750°C, which is consistent with the TG/DTA results. Nb-doped C12A7:e<sup>-</sup> experienced pest oxidation in that temperature range which was associated with the first exothermic peak in the C5 DT curve. The specimen had been near completely oxidized at 800°C evidenced by the transformation into white powder and maximum percentage of mass gain observed in the TG curve.

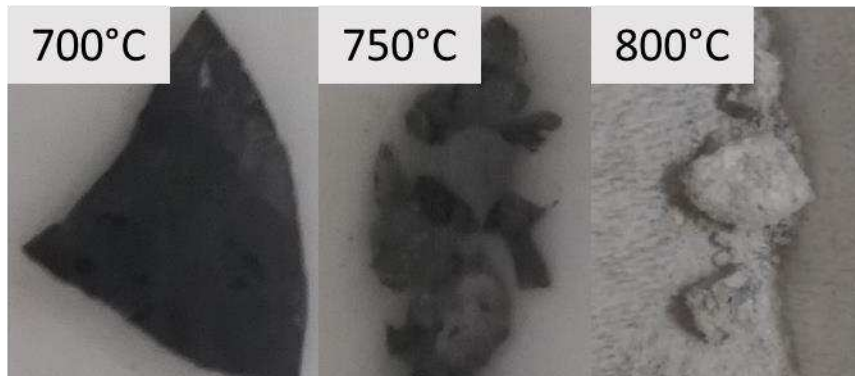


Figure 5.19: C5 specimen after being held at 700°C, 750°C, and 800°C in a furnace with an air atmosphere

Fig 5.20 displays the photos of specimens of D4 after heat treatment at different temperatures. At 700 °C, D4 experienced minimal surface oxidation, less than 0.1% determined by TGA. Cracking and the formation of white regions at 750°C resulted from pest oxidation, also observed in the C5 specimen, and further evidenced pest oxidation is initiated between 700-750°C. The specimen had been near completely oxidized at 850°C evidenced by the transformation into white powder and maximum percentage of mass gain observed in the TG curve.



Figure 5.20: D4 specimen after being held at 700°C, 750°C, and 850°C in a furnace with an air atmosphere

Nb-doped C12A7: $e^-$  experienced four oxygen uptake events causing rapid mass gain: (1) oxygen from the surrounding environment (air), was adsorbed onto the sample surface and then started to react with Nb; (2) oxidation of Nb metal phase occurred at a high rate and caused high internal stress inside the sample, leading to cracking; (3) the electride phase experienced a phase change to the oxy-C12A7 phase; and (4) remaining Nb oxidized. These events occurred rapidly within a small temperature range, approximately 725-770°C for C5 and 725-825°C for D4 (shown in Fig. 5.16), indicated by the large sudden increases in mass gain rate, nearly instantaneous mass gain up to 4.21%, followed by an abrupt decrease in mass gain rate and mass stabilization below 1050 °C.

Fig 5.21 displays the XRD patterns of the specimen from C5 and D4 after being held at 900°C. The primary phase identified in as-synthesized C5 (Fig 5.8b) and D4 (Fig 5.11b) was C12A7: $e^-$ . Peaks for NbAl<sub>3</sub> (Fig 5.8b) revealed the intermetallic as the only secondary phase present in C5. Peaks for Nb metal and C3A (Fig 5.11b) demonstrated Nb-C12A7: $e^-$  separation in D4 which is consistent with D1. After the thermal hold at 900°C, NbAl<sub>3</sub> peaks disappeared in C5 and the Nb metal peaks disappeared in D4. Meanwhile, CaNb<sub>2</sub>O<sub>6</sub> (CN) appeared in both post-thermal-hold samples, suggested that CaNb<sub>2</sub>O<sub>6</sub> was the Nb-containing oxide byproduct from pest oxidation.

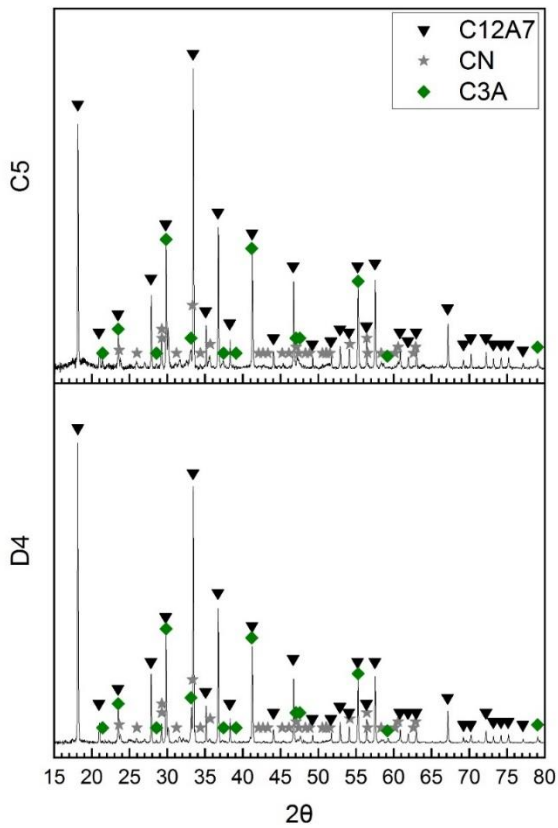


Figure 5.21: XRD patterns of C5 and D4 powders after TG/DTA

Reaction 5.9 and 5.10 represent the phase transition occurred in C5 and D4, respectively, during heating in TG.

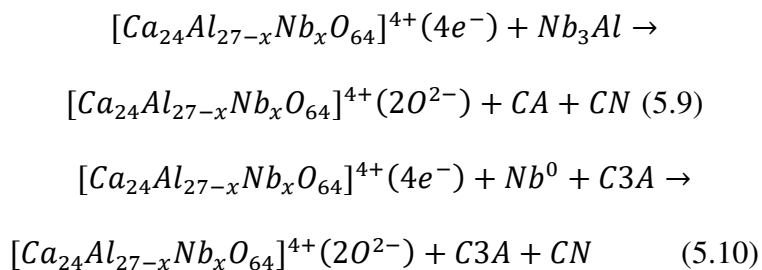


Fig 5.22 presents a flow diagram detailing the products that resulted from each process step in C5 and D4. In Nb-doped C12A7: $e^-$ , represented by  $[Ca_{24}Al_{27-x}Nb_xO_{64}]^{4+}(4e^-)$ , x

represents the average Nb concentration per unit cell in doped samples. The nominal concentration for C5 and D4 is  $x = 1$ . For these processes where the  $x$  value is  $0 < x < 1$ . It is important to note that  $x_C \neq x_D$ . The presence of  $\text{NbAl}_3$  in C5 confirmed  $x_C \neq 1$  and the presence of Nb metal in D4 confirmed  $x_D \neq 1$ . EDS analysis of C5 indicated successful Nb doping, i.e.,  $x_C > 0$ . Though D4 has some Nb separation during reduction by SPS, some Nb remained as dopants, i.e.,  $x_D > 0$ , indicated by the lower final percent mass gain compared to C5 with an assumed homogenous distribution of Nb and the same nominal concentration for both samples.

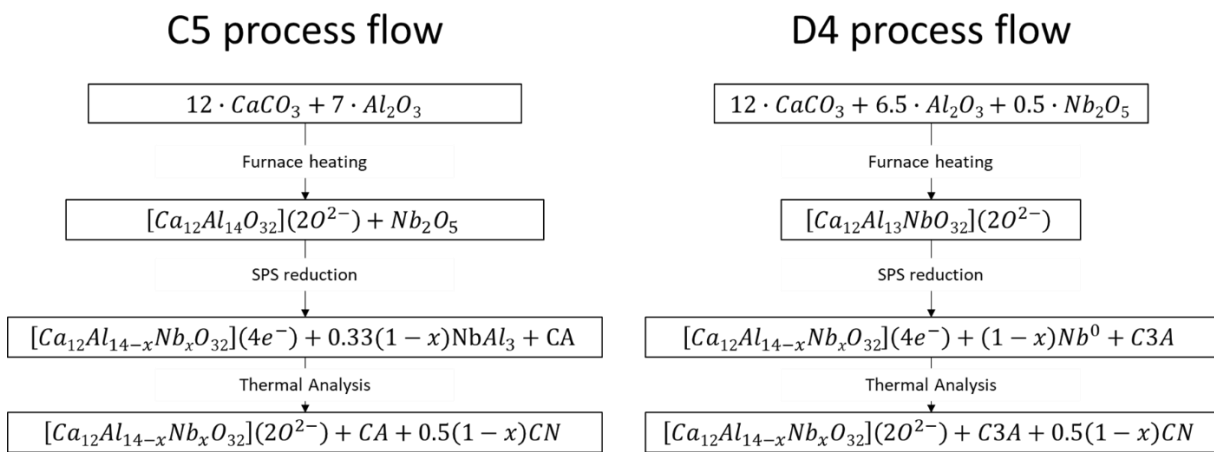


Figure 5.22: Phase evolution during the process flow for the C5 and D4

The important result to focus on from this section is Nb-doped C12A7: $e^-$  showed an increase in the onset temperature of oxidation. Pest oxidation caused Nb-doped C12A7: $e^-$  specimens to disintegrate when oxidized but was attributed to the presence of  $\text{NbAl}_3$  and Nb metal secondary phases.

## 5.5 Nb Doping Summary

Nb-doping of C12A7 and C12A7: $e^-$  was achieved in this study. Nb-doped C12A7: $e^-$  was successfully synthesized by the SPS of the preformed mixture of C12A7 and  $\text{Nb}_2\text{O}_5$  and

simultaneous reduction (Plan C) and the reduction of preformed Nb-doped C12A7 produced from SSR of CaCO<sub>3</sub>, Al<sub>2</sub>O<sub>3</sub>, and Nb<sub>2</sub>O<sub>5</sub> mixture (Plan D). Highly reduced Nb-doped C12A7:e<sup>-</sup> samples were obtained when the SPS processing temperature increased to 1350°C. Despite that none of the Nb-doped C12A7:e<sup>-</sup> samples had a higher electrical conductivity than undoped C12A7:e<sup>-</sup>, sample D4 exhibited a same level of electrical conductivity to that of undoped C12A7:e<sup>-</sup>. NbAl<sub>3</sub> secondary phase formed in the highly reduced C-type produced sample and Nb metal phase formed in the highly reduced D-type produced sample. Nb-doped C12A7:e<sup>-</sup> specimens exhibited an increased oxidation onset temperature up to 200°C higher than that of undoped C12A7:e<sup>-</sup>. Pest oxidation caused Nb-doped C12A7:e<sup>-</sup> specimens to disintegrate into white powder during thermal testing. The pest oxidation was attributed to high internal stress originated from the oxidation of the NbAl<sub>3</sub> and Nb metal phases.

## CHAPTER 6: CONCLUSION

In this work, the cationic doping of mayenite electride ( $\text{C}12\text{A}7:\text{e}^-$ ) using Cu and Nb as the dopant candidates was attempted with the aim of improving the thermal stability of  $\text{C}12\text{A}7:\text{e}^-$ . Cu-doping and Nb-doping of  $\text{C}12\text{A}7:\text{e}^-$  was successfully achieved. Diffusion doping via SPS was the effective and efficient method to produce Cu-doped  $\text{C}12\text{A}7:\text{e}^-$ . *In-situ* doping of  $\text{C}12\text{A}7:\text{e}^-$  via SPS with concurrent reduction of precursor  $\text{C}12\text{A}7$  with  $\text{Nb}_2\text{O}_5$  and reduction of preformed Nb-doped  $\text{C}12\text{A}7$  successfully synthesized Nb-doped  $\text{C}12\text{A}7:\text{e}^-$ . In this chapter, key findings are summarized. Finally, remaining scientific questions are discussed and an outlook of future research directions is provided.

### 6.1 Thermal stability of mayenite electride

Cu-doping and Nb-doping increased the onset temperature of oxidation compared to undoped  $\text{C}12\text{A}7:\text{e}^-$ . Therefore, increased thermal stability of  $\text{C}12\text{A}7:\text{e}^-$  can be achieved by cationic-doping. The thermal stability of undoped  $\text{C}12\text{A}7:\text{e}^-$  was analyzed using TG/DTA. The oxidation onset temperature was determined to be  $570^\circ\text{C}$ . Oxidation was found to initiate on the surface and then propagated through the bulk. The formation of white regions was observed on oxidation surfaces and then transitioned into translucent tan regions. Oxy-mayenite ( $\text{C}12\text{A}7$ ), as well as secondary calcium aluminate phases such as C3A or CA or both, were identified in the white regions, while the translucent bulk material was determined to be single phase of  $\text{C}12\text{A}7$ . Undoped  $\text{C}12\text{A}7:\text{e}^-$  held at  $1000^\circ\text{C}$  was translucent with a white surface layer. When the hold temperature was increased to  $1350^\circ\text{C}$ , the sample turned to completely translucent, which suggested that the secondary CA and C3A phases reacted to form  $\text{C}12\text{A}7$ . Results of undoped  $\text{C}12\text{A}7:\text{e}^-$  were used as a baseline to investigate the effect of Cu-doped  $\text{C}12\text{A}7:\text{e}^-$  and Nb-doped  $\text{C}12\text{A}7:\text{e}^-$ .

## 6.2 Copper Doping Experiments

The synthesis of Cu-doped C<sub>12</sub>A<sub>7</sub>:e<sup>-</sup> was achieved via solid-state diffusion via two methods: diffusion doping in a conventional furnace (F-type) and SPS diffusion doping (S-type). A reduction of the lattice parameter compared to the undoped C<sub>12</sub>A<sub>7</sub>:e<sup>-</sup> was achieved. F-type processing led to formation of Cu metal onto the surface of C<sub>12</sub>A<sub>7</sub>:e<sup>-</sup>, forming a metal-ceramic composite of Cu-C<sub>12</sub>A<sub>7</sub>:e<sup>-</sup> rather than solely Cu-doping. F-type methods also resulted in C<sub>3</sub>A formation. Cu-doping was effectively and efficiently achieved via the novel SPS diffusion doping method. S-type samples experienced little if any secondary phase formation. S1, S2, and S3 increased in onset temperature for oxidation to 625°C and peak temperatures to the range of 800-900°C, while S2 and S3 exhibited lower oxidation rates and lower total mass gain percentages at 1050°C, compared to the undoped C<sub>12</sub>A<sub>7</sub>:e<sup>-</sup>. SPS diffusion doping of Cu at 800 °C gave rise to a minimum lattice parameter ( $a = 11.942 \text{ \AA}$ ) of C<sub>12</sub>A<sub>7</sub>:e<sup>-</sup>, the lowest oxidation rate, and the smallest mass gain percent at 1050 °C. The electrical conductivity significantly increased to 389.4 S/cm in S2 compared to the undoped C<sub>12</sub>A<sub>7</sub>:e<sup>-</sup> (103.7 S/cm). In conclusion, Cu-doping was experimentally proved to be an effective approach to improve the thermal stability of C<sub>12</sub>A<sub>7</sub>:e<sup>-</sup> and meanwhile increase the electrical conductivity.

## 6.3 Niobium Doping Experiments

Five different processing routes were investigated with the goal of achieving Nb-doping of C<sub>12</sub>A<sub>7</sub>:e<sup>-</sup>. Nb-doped C<sub>12</sub>A<sub>7</sub>:e<sup>-</sup> was successfully synthesized via two methods: (1) the SPS of the preformed mixture of C<sub>12</sub>A<sub>7</sub> and Nb<sub>2</sub>O<sub>5</sub> and simultaneous reduction (C-type) and (2) the subsequent reduction of preformed Nb-C<sub>12</sub>A<sub>7</sub> produced from SSR (D-type). Thermal analysis results suggested Nb-doping successfully increased the oxidation resistance of C<sub>12</sub>A<sub>7</sub>:e<sup>-</sup> by

increasing the onset temperature of the oxidation. However, catastrophic pest oxidation occurred during thermal analysis, which is attributed to the presence of metallic niobium phases.

Increased processing temperatures for C-type and D-type processing resulted in better reduction of the oxy-C12A7 to the electride phase and simultaneously Nb-doping. The Nb doping methods that used a precursor mixture of C12A7: $e^-$  with Nb metal (A-type process) and a precursor mixture of C12A7: $e^-$  with Nb<sub>2</sub>O<sub>5</sub> (B-type process) were determined to be ineffective for Nb doping. The C-type samples contained a Nb rich bulk region and Nb deficient particles that could be visibly identified. Successful Nb-doping of C12A7: $e^-$  was confirmed in C2 and C5 by combination of XPS and EDS results. Sample D4 contained homogenously dispersed Nb metal particles that separated from Nb-doped C12A7, which caused C3A secondary phase formation.

Improvement in resistance to rapid oxidation was demonstrated in Nb-doped C12A7: $e^-$  samples compared to the undoped counterpart. The onset temperature of rapid oxidation was increased to 745°C and 770°C for the fully reduced Nb-doped C12A7: $e^-$  (C5 and D4). The thermal stability of the C12A7: $e^-$  was significantly improved by the increase in oxidation onset temperature by 150°C to 200°C. The first oxidation event was attributed to pest oxidation that caused disintegration of Nb-C12A7: $e^-$  specimens. The CaNb<sub>2</sub>O<sub>6</sub> was the Nb-containing compound formed during pest oxidation of NbAl<sub>3</sub> and Nb metal secondary phases. Nb-doped C12A7 and CA also formed due to Nb-doped C12A7: $e^-$  oxidation.

The essential findings of this study are the increased onset temperature for rapid oxidation for Nb-doped C12A7: $e^-$  and Cu-doped C12A7: $e^-$  when compared to undoped C12A7: $e^-$ . Cu-doping is the preferable method due to high amounts of secondary phases resulted from Nb-doping and pest oxidation of Nb-doped C12A7: $e^-$  samples. These results will intrigue additional studies of cation doped C12A7: $e^-$  materials with increased stability of the electride phase.

## 6.4 Future Research Directions

### Cationic Doped Mayenite Electride

Cationic doping of C<sub>12</sub>A<sub>7</sub>:e<sup>-</sup> is a growing field of research that has gained high interest in some industries including electronics and aeronautics. A limited number of cationic dopants have been researched in C<sub>12</sub>A<sub>7</sub>:e<sup>-</sup> and thermal stability had not been the primary goal. Creating cation doped C<sub>12</sub>A<sub>7</sub>:e<sup>-</sup> with greater thermal stability would allow the material to be used in applications that require high processing temperatures such as thermionic cooling devices. The findings of my work will encourage more research effort to look into the effect of cationic doping on the thermal stability of C<sub>12</sub>A<sub>7</sub>:e<sup>-</sup>.

### Cationic Dopant Selection

In this study, Cu-C<sub>12</sub>A<sub>7</sub>:e<sup>-</sup> and Nb-C<sub>12</sub>A<sub>7</sub>:e<sup>-</sup> exhibited greater thermal stability compared to undoped C<sub>12</sub>A<sub>7</sub>:e<sup>-</sup>. Optimization of the dopant concentration would maximize thermal stability of the electride phase. Nominal concentrations of cationic dopant elements can be used to synthesize cation-doped C<sub>12</sub>A<sub>7</sub>:e<sup>-</sup> which has been outlined in previous studies to test electrical conductivity changes. Based on the results of this study, Cu was the preferred dopant. Other divalent cationic dopants can be pursued in the future research. Table 6.1 displays properties of some dopant candidates that could potentially increase the thermal stability of C<sub>12</sub>A<sub>7</sub>:e<sup>-</sup>. It should be noted that Mg and Sr have been doped into C<sub>12</sub>A<sub>7</sub>:e<sup>-</sup> but thermal stability was not investigated.

Table 6.1: Element properties of possible dopants<sup>72</sup>

Element	Valence States	Metal Melting Point [°C]	Oxide Melting Point [°C]	Covalent Radius [Å]
Mg	2+	650	2852	1.5
Zr	3+, 4+	1855	2715	1.55
Sr	2+	777	2531	2.0
Pd	2+, 4+	1555	750	1.4
Cd	2+	321	1427	1.55

Zn	2+	419	1975	1.35
Ni	2+, 3+	1455	600	1.35
Co	2+, 3+	1495	895	1.35

Modeling can predict the thermal stability for C12A7: $e^-$  with potential dopants. Elements with high oxide phase melting temperatures, like Mg, Zr, Sr, Cd, or Zn, could increase thermal stability compared to the undoped C12A7: $e^-$ . High thermal stability of the oxide phase can decrease the oxide ion mobility in C12A7: $e^-$  lowering the rate of oxidation. Transition metals in the same period of the periodic table as Cu have comparable valence states, ionic radii, and covalent radii. The elements Zn, Ni, and Co fit that description and have been previously used to dope oxy-mayenite. In contrast to the findings of this study, Zn-doped C12A7: $e^-$  resulted in expansion of the lattice<sup>36</sup>, while it was hypothesized that reduction of lattice parameter contributed to the increased thermal stability in the Cu-doped C12A7: $e^-$ . However, cationic dopants that occupy Ca sites in the C12A7 framework, such as Mg, have been shown to affect anion mobility<sup>70</sup>, which has the potential to reduce oxidation rate. The optimal homologous temperature ( $T_H$ ) for Cu diffusion doping using SPS found in this study corresponds to a  $T_H \approx 0.8$ . Elements with metal melting temperatures near C12A7: $e^-$  would allow high dopant cation, native cation, and vacancy mobility. Those elements would be potential candidates for the novel SPS diffusion doping method introduced in this study. It will be time-consuming and cost ineffective if the cationic dopants were selected just by try-and-error experimentally. Therefore, computational and modeling work, such as density functional theory calculations and thermodynamic stability prediction, on the C12A7: $e^-$  rather than just on the oxy-mayenite, are also in demand to guide the dopant selection.

### SPS Diffusion Process

The effect of SPS on the cation mobility are not yet well understood. The general trend of the effect of the applied field, high heating rate, and applied pressure can be predicted from models and verified by relevant experiments. However, direct measurement of diffusion path during SPS is impossible to achieve. The SPS diffusion method has potential in industry to apply surface coatings or improve other processes that utilize diffusion. Surface layers applied by SPS could potentially have a semi-coherent interface with underlying materials compared to coatings that adhere to the surface, which would reduce adverse effects such as electrical conductivity losses. Multiple driving forces applied in SPS increase the cation mobility, allowing for faster diffusion compared to the conventional furnace heating methods. Diffusion bonding of two dissimilar materials, formation of intermetallic materials, and reinforcement of a material with a secondary phase (incorporation of carbon in iron to form cementite to make stainless steel) are a few examples. Both processes differ from the cationic doping of C<sub>12</sub>A<sub>7</sub>:e<sup>-</sup>. Neither process uses ion diffusion so mobility effects might be decreased or eliminated due to the lack of atomic charge. Further investigation should be put to elucidate the effects from SPS on diffusion kinetics to promote the application of this novel diffusion method in industry.

## References:

1. Lin Y, Smedskjaer MM, Mauro JC. Structure, properties, and fabrication of calcium aluminate-based glasses. *Int J Appl Glass Sci.* 2019;10(4):488–501. <https://doi.org/10.1111/ijag.13417>
2. Jeevaratnam J, Glasser LSD, Glasser FP. Structure of Calcium Aluminate,  $12\text{CaO}\cdot7\text{Al}_2\text{O}_3$ . *Nature.* 1962;194(4830):764–765. <https://doi.org/10.1038/194764b0>
3. Sushko PV, Shluger AL, Hayashi K, Hirano M, Hosono H. Mechanisms of oxygen ion diffusion in a nanoporous complex oxide  $12\text{CaO}\cdot7\text{Al}_2\text{O}_3$ . *Phys Rev B.* 2006;73(1):014101. <https://doi.org/10.1103/PhysRevB.73.014101>
4. Hosono H, Tanabe K, Takayama-Muromachi E, et al. Exploration of new superconductors and functional materials, and fabrication of superconducting tapes and wires of iron pnictides. *Sci Technol Adv Mater.* 2015;16(3). <https://doi.org/10.1088/1468-6996/16/3/033503>
5. Boysen H, Lerch M, Stys A, Senyshyn A. Structure and oxygen mobility in mayenite ( $\text{Ca}_{12}\text{Al}_{14}\text{O}_{33}$ ): a high-temperature neutron powder diffraction study. *Acta Crystallogr B.* 2007;63(5):675–682. <https://doi.org/10.1107/S0108768107030005>
6. Ebbinghaus SG, Krause H, Syrowatka F. Floating Zone Growth of Large and Defect-free  $\text{Ca}_{12}\text{Al}_{14}\text{O}_{33}$  Single Crystals. *Cryst Growth Des.* 2013;13(7):2990–2994. <https://doi.org/10.1021/cg400406t>
7. Lacerda M, Irvine JTS, Glasser FP, West AR. High oxide ion conductivity in  $\text{Ca}_{12}\text{Al}_{14}\text{O}_{33}$ . *Nature.* 1988;332(6164):525–526. <https://doi.org/10.1038/332525a0>
8. Hosono H, Hayashi K, Kajihara K, Sushko PV, Shluger AL. Oxygen ion conduction in  $12\text{CaO}\cdot7\text{Al}_2\text{O}_3$ :  $\text{O}_2^-$  conduction mechanism and possibility of  $\text{O}^-$  fast conduction. *Solid State Ion.* 2009;180(6):550–555. <https://doi.org/10.1016/j.ssi.2008.10.015>
9. Matsuishi S, Toda Y, Miyakawa M, et al. High-Density Electron Anions in a Nanoporous Single Crystal:  $[\text{Ca}_{24}\text{Al}_{28}\text{O}_{64}]^{4+}(4\text{e}^-)$ . *Science.* 2003;301(5633):626–629. <https://doi.org/10.1126/science.1083842>
10. Toda Y, Matsuishi S, Hayashi K, et al. Field Emission of Electron Anions Clathrated in Subnanometer-Sized Cages in  $[\text{Ca}_{24}\text{Al}_{28}\text{O}_{64}]^{4+}(4\text{e}^-)$ . *Adv Mater.* 2004;16(8):685–689. <https://doi.org/10.1002/adma.200306484>
11. Kim SW, Toda Y, Hayashi K, Hirano M, Hosono H. Synthesis of a Room Temperature Stable  $12\text{CaO}\cdot7\text{Al}_2\text{O}_3$  Electride from the Melt and Its Application as an Electron Field Emitter. *Chem Mater.* 2006;18(7):1938–1944. <https://doi.org/10.1021/cm052367e>
12. Kim SW, Matsuishi S, Nomura T, et al. Metallic State in a Lime-Alumina Compound with Nanoporous Structure. *Nano Lett.* 2007;7(5):1138–1143. <https://doi.org/10.1021/nl062717b>
13. Hosono H, Hayashi K, Kamiya T, Atou T, Susaki T. New functionalities in abundant element oxides: ubiquitous element strategy. *Sci Technol Adv Mater.* 2011;12(3):034303. <https://doi.org/10.1088/1468-6996/12/3/034303>
14. Zou W, Khan K, Zhao X, et al. Direct fabrication of C12A7 electride target and room temperature deposition of thin films with low work function. *Mater Res Express.* 2017;4(3):036408. <https://doi.org/10.1088/2053-1591/aa63c7>
15. Rudradawong C, Ruttanapun C. Combined effects of Mg reducing and Sn doping on the electrical conductivity of polycrystalline  $\text{Ca}_{12}\text{Al}_{14}\text{O}_{33}$  mayenite. *Appl Phys A.* 2019;125(4). <https://doi.org/10.1007/s00339-019-2548-2>

16. Li F, Zhang X, Liu H, *et al.* Rapid synthesis of inorganic  $[Ca_{24}Al_{28}O_{64}]^{4+}(e^-)_4$  electride and its performance as an electron thermal emitter. *Vacuum*. 2018;158:152–157. <https://doi.org/10.1016/j.vacuum.2018.09.055>
17. Watanabe S, Watanabe T, Ito K, *et al.* Secondary electron emission and glow discharge properties of  $12CaO\cdot7Al_2O_3$  electride for fluorescent lamp applications. *Sci Technol Adv Mater*. 2011;12(3):034410. <https://doi.org/10.1088/1468-6996/12/3/034410>
18. Hayashi K, Matsuishi S, Kamiya T, Hirano M, Hosono H. Light-induced conversion of an insulating refractory oxide into a persistent electronic conductor. *Nature*. 2002;419(6906):462–465. <https://doi.org/10.1038/nature01053>
19. Nishio Y, Nomura K, Yanagi H, Kamiya T, Hirano M, Hosono H. Short-channel nanowire transistor using a nanoporous crystal semiconductor  $12CaO\cdot7Al_2O_3$ . *Mater Sci Eng B*. 2010;173(1–3):37–40. <https://doi.org/10.1016/j.mseb.2009.12.018>
20. Kitano M, Inoue Y, Yamazaki Y, *et al.* Ammonia synthesis using a stable electride as an electron donor and reversible hydrogen store. *Nat Chem*. 2012;4(11):934–940. <https://doi.org/10.1038/nchem.1476>
21. Inoue Y, Kitano M, Kim S-W, Yokoyama T, Hara M, Hosono H. Highly Dispersed Ru on Electride  $[Ca_{24}Al_{28}O_{64}]^{4+}(e^-)_4$  as a Catalyst for Ammonia Synthesis. *ACS Catal*. 2014;4(2):674–680. <https://doi.org/10.1021/cs401044a>
22. Honkala K, Hellman A, Remediakis IN, *et al.* Ammonia Synthesis from First-Principles Calculations. *Science*. 2005;307(5709):555–558. <https://doi.org/10.1126/science.1106435>
23. Toda Y, Hirayama H, Kuganathan N, Torrisi A, Sushko PV, Hosono H. Activation and splitting of carbon dioxide on the surface of an inorganic electride material. *Nat Commun*. 2013;4(1):2378. <https://doi.org/10.1038/ncomms3378>
24. Wang Z, Pan Y, Dong T, *et al.* Production of hydrogen from catalytic steam reforming of bio-oil using  $C_{12}A_7-O^-$ -based catalysts. *Appl Catal Gen*. 2007;320:24–34. <https://doi.org/10.1016/j.apcata.2006.12.003>
25. Toda Y, Kubota Y, Hirano M, Hirayama H, Hosono H. Surface of Room-Temperature-Stable Electride  $[Ca_{24}Al_{28}O_{64}]^{4+}(e^-)_4$ : Preparation and Its Characterization by Atomic-Resolution Scanning Tunneling Microscopy. *ACS Nano*. 2011;5(3):1907–1914. <https://doi.org/10.1021/nn102839k>
26. Rand LP. Calcium aluminate electride hollow cathode, A. 2014.
27. Uriarri L, Allen EH. Electron Transpiration Cooling for Hot Aerospace Surfaces. *20th AIAA Int. Space Planes Hypersonic Syst. Technol. Conf.* American Institute of Aeronautics and Astronautics; n.d. <https://doi.org/10.2514/6.2015-3674>
28. Hanquist KM, Hara K, Boyd ID. Detailed modeling of electron emission for transpiration cooling of hypersonic vehicles. *J Appl Phys*. 2017;121(5):053302. <https://doi.org/10.1063/1.4974961>
29. Tang X, Kuehster AE, DeBoer BA, Preston AD, Ma K. Enhanced thermionic emission of mayenite electride composites in an Ar glow discharge plasma. *Ceram Int*. 2021;S027288422100612X. <https://doi.org/10.1016/j.ceramint.2021.02.233>
30. Liu YX, Ma L, Yan DT, *et al.* Effects of encaged anions on the optical and EPR spectroscopies of RE doped  $C_{12}A_7$ . *J Lumin*. 2014;152:28–32. <https://doi.org/10.1016/j.jlumin.2013.10.066>
31. Maurelli S, Ruszak M, Witkowski S, Pietrzyk P, Chiesa M, Sojka Z. Spectroscopic CW-EPR and HYSCORE investigations of  $Cu^{2+}$  and  $O_2^-$  species in copper doped nanoporous

- calcium aluminate ( $12\text{CaO}\cdot7\text{Al}_2\text{O}_3$ ). *Phys Chem Chem Phys PCCP*. 2010;12:10933–41. <https://doi.org/10.1039/c0cp00084a>
32. Mironova EYu, Ermilova MM, Orekhova NV, Tolkacheva AS, Shkerin SN, Yaroslavtsev AB. Transformations of Ethanol on Catalysts Based on Nanoporous Calcium Aluminate–Mayenite ( $\text{Ca}_{12}\text{Al}_{14}\text{O}_{33}$ ) and Mayenite Doped by Copper. *Nanotechnologies Russ.* 2017;12(11):597–604. <https://doi.org/10.1134/S1995078017060064>
33. Sato K, Fujita S, Suzuki K, Mori T. High performance of Ni-substituted calcium aluminosilicate for partial oxidation of methane into syngas. *Catal Commun.* 2007;8(11):1735–1738. <https://doi.org/10.1016/j.catcom.2007.02.006>
34. Teusner M, De Souza RA, Krause H, Ebbinghaus SG, Martin M. Oxygen transport in undoped and doped mayenite. *Solid State Ion.* 2016;284:25–27. <https://doi.org/10.1016/j.ssi.2015.11.024>
35. Tolkacheva AS, Shkerin SN, Plaksin SV, Pankratov AA, Moskalenko NI. Solid Solutions  $\text{Ca}_{12}\text{Al}_{14}\text{O}_{33\pm\delta}$ : V $^{5+}$ , Mo $^{5+}$ . *Refract Ind Ceram.* 2019;60(1):109–114. <https://doi.org/10.1007/s11148-019-00318-w>
36. Irvine JTS, West AR. Ca $_{12}\text{Al}_{14}\text{O}_{33}$ SOLID ELECTROLYTES DOPED WITH ZINC AND PHOSPHORUS. *Solid State Ion.* 1990;40:4.
37. Kurashige K, Toda Y, Matstuishi S, Hayashi K, Hirano M, Hosono H. Czochralski Growth of  $12\text{CaO}\cdot7\text{Al}_2\text{O}_3$  Crystals. *Cryst Growth Des.* 2006;6(7):1602–1605. <https://doi.org/10.1021/cg0600290>
38. Palacios L, Bruque S, Aranda MAG. Structure of gallium-doped mayenite and its reduction behaviour. *Phys Status Solidi B.* 2008;245(4):666–672. <https://doi.org/10.1002/pssb.200743425>
39. Yi H, Lv Y, Wang Y, Fang X, Mattick V, Xu J. Ga-doped  $\text{Ca}_{12}\text{Al}_{14}\text{O}_{33}$  mayenite oxide ion conductors: synthesis, defects, and electrical properties. *RSC Adv.* 2019;9(7):3809–3815. <https://doi.org/10.1039/C8RA08254E>
40. Huang J, Valenzano L, Sant G. Framework and Channel Modifications in Mayenite ( $12\text{CaO}\cdot7\text{Al}_2\text{O}_3$ ) Nanocages By Cationic Doping. *Chem Mater.* 2015;27(13):4731–4741. <https://doi.org/10.1021/acs.chemmater.5b01360>
41. Khan K, Tareen AK, Elshahat S, et al. Facile metal-free reduction-based synthesis of pristine and cation-doped conductive mayenite. *RSC Adv.* 2018;8(43):24276–24285. <https://doi.org/10.1039/C8RA02790K>
42. Khan K, Khan Tareen A, Elshahat S, et al. Facile synthesis of a cationic-doped  $[\text{Ca}_{24}\text{Al}_{28}\text{O}_{64}]^{4+}(4\text{e}^-)$  composite via a rapid citrate sol–gel method. *Dalton Trans.* 2018;47(11):3819–3830. <https://doi.org/10.1039/C7DT04543C>
43. Khan K, Tareen A khan, Khan U, et al. Single step synthesis of highly conductive room-temperature stable cation-substituted mayenite electrode target and thin film. *Sci Rep.* 2019;9(1). <https://doi.org/10.1038/s41598-019-41512-7>
44. Yi H, Lv Y, Mattick V, Xu J. Cobalt-doped  $\text{Ca}_{12}\text{Al}_{14}\text{O}_{33}$  mayenite oxide ion conductors: phases, defects, and electrical properties. *Ionics.* 2019;25(11):5105–5115. <https://doi.org/10.1007/s11581-019-03088-0>
45. Huang J, Hu L, Zhang H, et al. A facile method for the synthesis of tapered ZnO:Cu nanorod arrays and its secondary growth. *J Cryst Growth.* 2012;351(1):93–100. <https://doi.org/10.1016/j.jcrysgro.2012.04.018>

46. Yilmaz S, McGlynn E, Bacaksiz E, *et al.* Effects of Cu diffusion-doping on structural, optical, and magnetic properties of ZnO nanorod arrays grown by vapor phase transport method. *J Appl Phys.* 2012;111(1):013903. <https://doi.org/10.1063/1.3673861>
47. Mambetova KM, Smal' NN, Shandarov SM, Orlikov LN, Arrestov SI, Smirnov SV. Formation Dynamics of Transmission Holograms in Lithium Niobate Crystals Doped by Copper Through High-Temperature Diffusion. *Radiophys Quantum Electron.* 2015;57(8):603–609. <https://doi.org/10.1007/s11141-015-9545-x>
48. Li F, Zhang X, Liu H, *et al.* In situ synthesis of  $[Ca_{24}Al_{28}O_{64}]^{4+}(4e^-)$  electride ceramic from C12A7 + C3A mixture precursor. *J Am Ceram Soc.* 2019;102(3):884–888. <https://doi.org/10.1111/jace.16103>
49. Kuehster AE. Processing of Mayenite Electride and Its Composites in Spark Plasma Sintering. M.S.; Colorado State University; United States -- Colorado; 2019
50. Chung JH, Ryu JH, Eun JW, Choi BG, Shim KB. One-Step Synthesis of a  $12CaO \cdot 7Al_2O_3$  Electride via the Spark Plasma Sintering (SPS) Method. *Electrochim Solid-State Lett.* 2011;14(12):E41. <https://doi.org/10.1149/2.021112esl>
51. Xiao Y, Zhang X, Zhang J.  $[Ca_{24}Al_{28}O_{64}]^{4+}(4e^-)$  electrides ceramic with high-electron concentration rapidly fabricated by spark plasma sintering of Ca, Al organic powder precursor in spark plasma sintering. *Ceram Int.* 2020. <https://doi.org/10.1016/j.ceramint.2020.07.273>
52. Sintering in the Powder Metallurgy Process. *Powder Metall Rev.* 2016.
53. Castro R, Benthem K. Sintering: Mechanisms of Conventional Nanodensification and Field Assisted Processes. 2013 <https://doi.org/10.1007/978-3-642-31009-6>
54. Chen F, Yang S, Wu J, *et al.* Spark Plasma Sintering and Densification Mechanisms of Conductive Ceramics under Coupled Thermal/Electric Fields. *J Am Ceram Soc.* 2015;98(3):732–740. <https://doi.org/10.1111/jace.13381>
55. Mackenzie KJD, Ryan MJ. Effect of electric fields on solid-state reactions between oxides. *J Mater Sci.* 1981;16(3):579–588. <https://doi.org/10.1007/BF00552194>
56. Asoka-Kumar P, O'Brien K, Lynn KG, Simpson PJ, Rodbell KP. Detection of current-induced vacancies in thin aluminum–copper lines using positrons. *Appl Phys Lett.* 1996;68(3):406–408. <https://doi.org/10.1063/1.116700>
57. Li F, Zhang X, Zhang J. One-step fabrication of inorganic  $[Ca_{24}Al_{28}O_{64}]^{4+}(4e^-)$  from transition metal and oxide compound precursors by reactive sintering. *Ceram Int.* 2019. <https://doi.org/10.1016/j.ceramint.2019.08.052>
58. Cegan T, Petlak D, Skotnicova K, Jurica J, Smetana B, Zla S. Metallurgical Preparation of Nb–Al and W–Al Intermetallic Compounds and Characterization of Their Microstructure and Phase Transformations by DTA Technique. *Molecules.* 2020;25(8). <https://doi.org/10.3390/molecules25082001>
59. Levin I, Chan JY, Geyer RG, Maslar JE, Vanderah TA. Cation Ordering Types and Dielectric Properties in the Complex Perovskite  $Ca(Ca_{1/3}Nb_{2/3})O_3$ . *J Solid State Chem.* 2001;156(1):122–134. <https://doi.org/10.1006/jssc.2000.8971>
60. Rohl JW. Superconducting Magnets. *Mod. Phys. Alpha Z0.* John Wiley & Sons, Ltd; 1994
61. WebElements Periodic Table » Copper » radii of atoms and ions. n.d.
62. The development of oxidation-resistant niobium alloys. *J Common Met.* 1960;2(2–4):191–206. [https://doi.org/10.1016/0022-5088\(60\)90014-X](https://doi.org/10.1016/0022-5088(60)90014-X)
63. Hebsur MG, Stephens JR, Smialek J, Barrett CA, Fox D. Influence of alloying elements on the oxidation behavior of NbAl sub 3. 1988

64. Porter DA, Easterling KA, Sherif MY. Phase transformations in metals and alloys. 2nd ed. 2009
65. Hayashi K, Ueda N, Hirano M, Hosono H. Effect of stability and diffusivity of extra-framework oxygen species on the formation of oxygen radicals in  $12\text{CaO}\cdot 7\text{Al}_2\text{O}_3$ . *Solid State Ion.* 2004;173(1):89–94. <https://doi.org/10.1016/j.ssi.2004.07.057>
66. Kim SW, Hosono H. Synthesis and properties of  $12\text{CaO}\cdot 7\text{Al}_2\text{O}_3$  electride: review of single crystal and thin film growth. *Philos Mag.* 2012;92(19–21):2596–2628. <https://doi.org/10.1080/14786435.2012.685770>
67. Vanderah TA, Febo W, Chan JY, et al. Phase Equilibria and Dielectric Behavior in the  $\text{CaO}:\text{Al}_2\text{O}_3:\text{Nb}_2\text{O}_5$  System. *J Solid State Chem.* 2000;155(1):78–85. <https://doi.org/10.1006/jssc.2000.8894>
68. Gaul E. Coloring titanium and related metals by electrochemical oxidation. *J Chem Educ.* 1993;70(3):176. <https://doi.org/10.1021/ed070p176>
69. Komatsu I, Aoki H, Ebisawa M, Kuroda A, Kuroda K, Maeda S. Color change mechanism of niobium oxide thin film with incidental light angle and applied voltage. *Thin Solid Films.* 2016;603:180–186. <https://doi.org/10.1016/j.tsf.2016.02.011>
70. Bertoni MI, Mason TO, Medvedeva JE, Freeman AJ, Poeppelmeier KR, Delley B. Tunable conductivity and conduction mechanism in an ultraviolet light activated electronic conductor. *J Appl Phys.* 2005;97(10):103713. <https://doi.org/10.1063/1.1899246>
71. Rausch JJ, Simcoe CR. Low-Temperature Disintegration of Intermetallic Compounds. *Armour Res Found Chic Ill.* 1961;Final Report(ARF-2981-4):28.
72. AMERICAN ELEMENTS® | The Advanced Materials Manufacturer. n.d.